IFT - UNESP
INSTITUTO DE FÍSICA TEÓRICA

unesp
UNIVERSIDADE ESTADUAL PAULISTA
"JÚLIO DE MESQUITA FILHO"

Master Thesis IFT–T.005/18

Excitons in Monolayer Tellurium Studied with QPMBPT and a Hydrogen-Like Model

Kevin Angello Lizárraga Olivares

June, 2019

IFT - UNESP
INSTITUTO DE FÍSICA TEÓRICA

unesp
UNIVERSIDADE ESTADUAL PAULISTA
"JÚLIO DE MESQUITA FILHO"

Master Thesis

IFT–T.005/18

Excitons in Monolayer Tellurium Studied with QPMBPT and a Hydrogen-Like Model

Kevin Angello Lizárraga Olivares

Thesis presented to the Postgraduate program held on Instituto de Física Teórica at Universidade Estadual Paulista with the purpose to fullfill the requirements to obtain the master degree on physics.

Alexandre Reily Rocha - Advisor

June, 2019

Lizárraga Olivares, Kevin Angello
L789e Excitons in monolayer tellurium studied with QPMBPT and a hydrogen-like model / Kevin Angello Lizárraga Olivares. – São Paulo, 2019
161 f. : il.

Dissertação (mestrado) - Universidade Estadual Paulista (Unesp), Instituto de Física Teórica (IFT), São Paulo
Orientador: Alexandre Reily Rocha

1. Matéria condensada. 2. Matéria - Propriedades. 3. Células solares. I. Título

Sistema de geração automática de fichas catalográficas da Unesp. Biblioteca do Instituto de Física Teórica (IFT), São Paulo. Dados fornecidos pelo autor(a).

The present work is dedicated to all my family. Specially to my mom, Carito, who always give me strength, advice and courage to maintain the path for the fulfillment of my dreams. To my father and siblings, for their entertaining talks via skype. To my girlfriend, Anarin, who has been part of my family for three years, for her love, sympathy, time and perseverance to face our long distance relationship. And, for all my relatives who always believe on me.

Abstract

Excitons play a key role in photovoltaic (PV) applications. Nowadays, thin film PV technology has a 9% of worldwide production. In particular, tellurium has been alloyed with cadmium (Cd-Te) and used in the manufacture of thin film solar cells. However, tellurium technology could be improved if lower dimensional structures are used, for instance, the single layer form known as tellurene. Tellurene can be successfully synthesized on a substrate (e.g graphene), has high carrier mobilities, the lowest thermal conductivity among single-atom layers and a tunable optical band gap which make it a prominent candidate for technology development. In this work, we carry out ab-initio quasi-particle many body perturbation theory (QPMBPT) calculations to analyze the excitonic effects in light absorption for tellurene. Since tellurium is a heavy element, our analysis has been extended to the presence of spin orbit coupling, which makes a significant change in the band-structure as well as in the imaginary part of the dielectric constant. The anisotropy of tellurene is evident in the absorption spectra, which is similar to black phosphorus, with the strongest excitation along the zigzag direction and exciton binding energies similar to other 2D semiconductors. Furthermore, we compare our results with an effective hydrogen-like model, in which the electron and hole interacts via an anisotropic Keldysh interaction, i.e. an screened Coulomb potential, in order to estimate the exciton binding energy for SOC and non-SOC cases. The results show an excellent agreement between QPMBPT methodology and the hydrogen like model.

Keywords: Photovoltaic, solar cells, monolayer, tellurene, hole, optical band gap, exciton, QPMBPT, anisotropy, spin orbit coupling, hydrogen, keldysh interaction, binding energy.

Abstract in Portuguese

Os excitons desempenham um papel fundamental em ções fotovoltaicas (FV). Atualmente, a tecnologia FV de filme fino possui 9% da produção mundial. Em particular, o telúrio foi ligado ao cádmio (Cd-Te) e utilizado no fabrico de células solares de película fina. No entanto, a tecnologia de telúrio pode ser melhorada se estruturas de menor dimensão forem usadas, por exemplo, a forma de monocamada conhecida como telureno. O telureno pode ser sintetizado com sucesso em um substrato (por exemplo, grafeno), tem alta mobilidade dos portadores, a condutividade térmica mais baixa entre monocamadas de átomos e um gap de banda óptica sintonizável que o torna em um candidato proeminente para o desenvolvimento de tecnologia. Neste trabalho, realizamos cálculos ab-initio da teoria da perturbação do muitos corpos (QPMBPT) para analisar os efeitos excitônicos na absorção de luz pelo telureno. Como telúrio é um elemento pesado, nossa análise foi estendida para a presença de acoplamento spin-órbita, que faz uma mudança significativa na estrutura da banda, bem como na parte imaginária da constante dielétrica. A anisotropia da telurena é evidente no espectro de absorção, que é semelhante ao fósforo preto, com a mais forte excitação ao longo da direção em ziguezague e energias de ligação de excitons semelhantes a outros semicondutores 2D. Além disso, comparamos nossos resultados com um modelo efetivo de hidrogênio, no qual o elétron e o buraco interagem através de uma interação anisotrópica de Keldysh, ou seja, um potencial de Coulomb rastreado, para estimar a energia de ligação do exciton para os casos com SOC e não-SOC. Os resultados mostram uma excelente concordância entre a metodologia QPMBPT e o modelo do tipo hidrogênio.

Palavras-chave: Fotovoltaica, células solares, monocamada, telureno, buraco, gap de banda óptica, exciton, QPMBPT, anisotropia, acoplamento spin-órbita, hidrogênio, interação keldysh, energia de ligação.

List of Figures

List of Tables

Contents

CHAPTER 1

Introduction

1.1 Solar Energy and Photovoltaic Technology

Nowadays the world suffers from the contamination caused by fossil fuels in order to produce electricity. For this reason, new types of energy have been employed such as solar, wind or even nuclear energy. Where the solar energy is the most abundant, e.g, the amount of solar radiation striking the Earth over a three-day period is equivalent to the energy stored in all fossil energy sources. It is natural, does not pollute the planet, and is permanent, since compared to humanity life time, the sun can be considered a stable source for the next millenia [1].

The solar industry, according to the European Commission report PV 2017, has received 57% of the total investment (113.7 billion) on renewable sources for 7 years in a row. In particular, the main countries that lead current investment are China (USD 78.3 billion), the USA (USD 46.4 billion), the United Kingdom (USD 24 billion) and Japan (USD 14.4 billion) [2]. Furthermore, solar cell production vary between 79 GW and 84 GW per year in terms of output power. The annual production for several countries is represented in (figure 1.1), which reaffirms the rapid growth in the usage of solar cells [2].

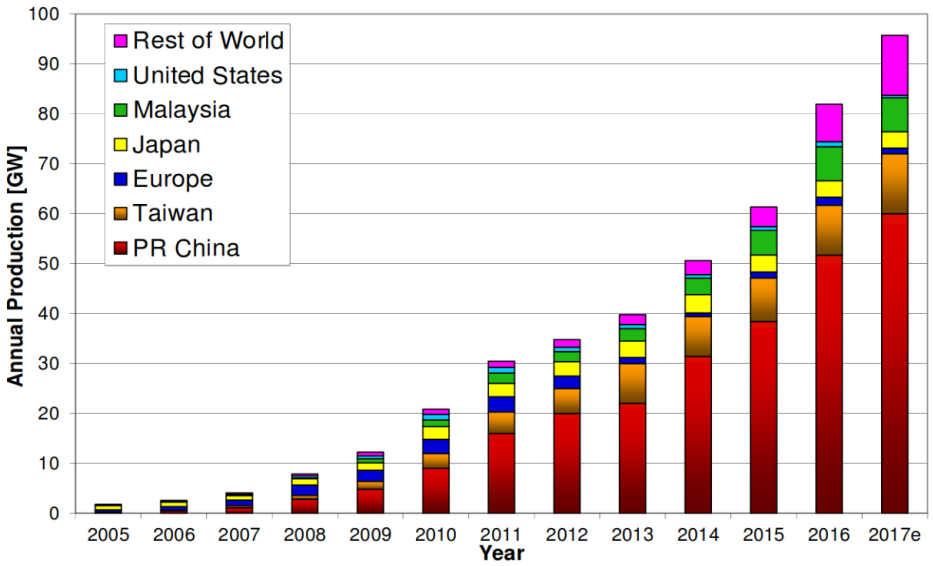

Figure 1.1: Annual world production in GW of Solar cells extracted from [2]

The production volume of Photovoltaic (PV) devices has increased, in the last 15 years, with a compound annual growth rate (CAGR) of over 40%, which sets the industry as one of the fastest growing worldwide [2]. The current PV manufactered are divided in three generations of solar cells. The first generation, also called conventional or wafer-based cells, are made of crystalline silicon (the most predominant PV technology) that includes materials such as polysilicon and monocrystalline silicon [1]. On the other hand, second generation cells are conformed by thin film solar cells, which includes amorphous silicon (aSi), Cadmium Telluride (CdTe) and Copper Indium Galium di-Selenide (CIGS). These are commercially significant in utility scale photovoltaic power stations, building integrated photo-

voltaics or in small stand-alone power system [1]. The third generation ranges over several thin film technologies (emerging PV), which have not been commercially applied (limited availability) and are still in the research phase [1]. Many of them use organic materials (dye-sensitized cells), organometallic compounds (biohybrid solar cell), polymer solar cell, as well as monolayer, quantum dots, micromorph and perovskite solar cells. By comparing the first and second generation solar cells, we find that the former are more commercially feasible due to their higher efficiency, meanwhile the second offers low production costs, but require more area to reach the same amount of energy yielded by silicon solar cells [1]. Even though, thin film solar cells are new to the market, they have reached a 9% share at worldwide total production. The different efficiency of PV cells are presented in figure 1.2, and a comparison on annual production in GW (Giga Watts) by the different PV techonologies is shown in figure 1.3 [3].

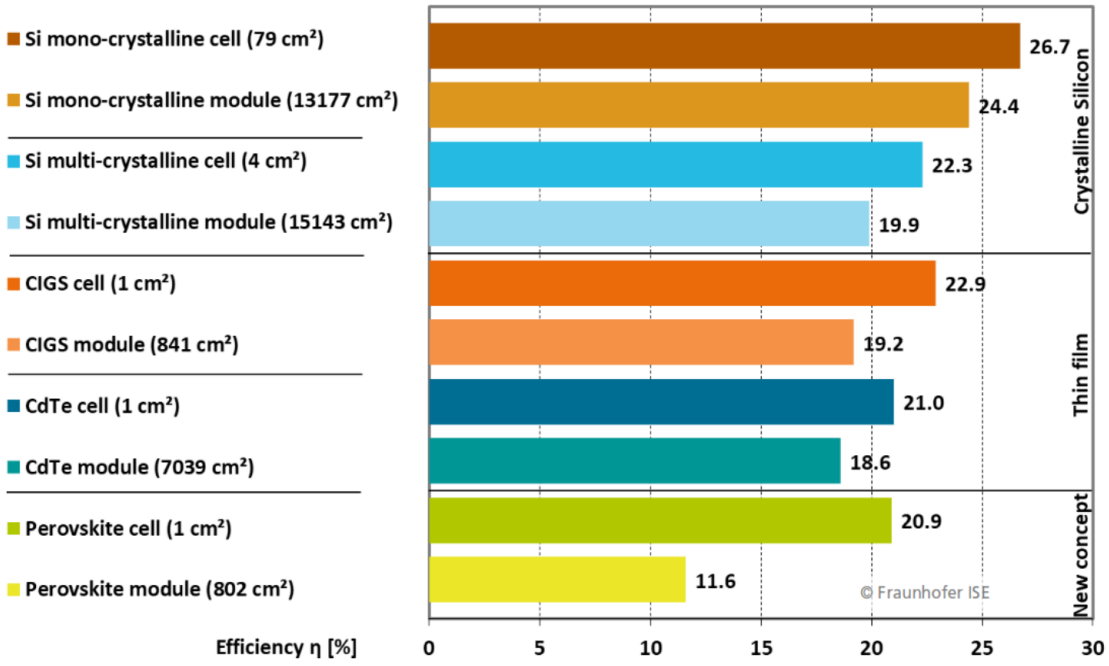

Figure 1.2: Efficiency comparison between solar cells technologies based on crystalline silicon, thin film and Perovskite [3].

The generation classification of solar cells only takes into account the time the technology has been in the industry. However, as we have seen from first and second generation, there are efficiency issues related to the conversion of light into electricity as well as high production costs compared to carbon-based electricity. This is where the third generation comes in to play by using new approaches in the transformation mechanism in order to achieve the goal of producing low-cost, high efficient solar cells. Consequently, another classification of solar cells can be done by taking into account the way in which electricity is produced: the conventional solar cells, that first appeared less than 30 years ago and is composed by the first and second generation solar cells, and excitonic solar cells, that cover

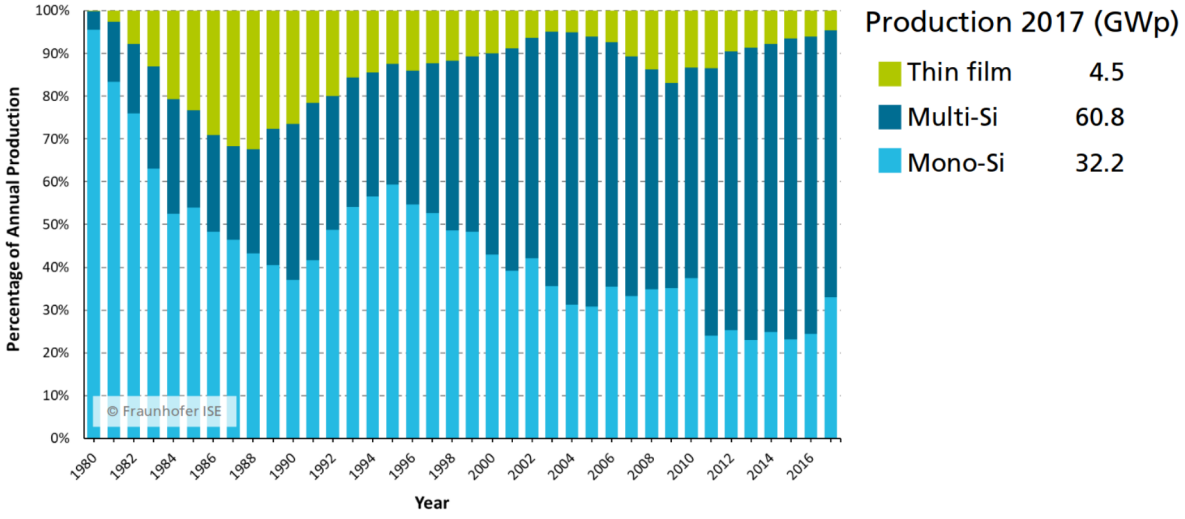

Figure 1.3: GW production per year from PV technologies from first and second generations, thin film (green), multi-Si (blue) and mono-Si (sky blue) [3].

third generation devices such as dye-sensitized solar cells (DSSCs), polymer, monolayer and quantum dot solar cells [1].

Conventional solar cells are based on the formation of an electron-hole free pair when light is absorbed, so, the electrons propagates freely on the conduction band meanwhile the holes do so in the valence band. Thus, the mechanism is related with the electron overcoming the electrical band gap. On the other hand, excitonic solar cells lay in the formation of an exciton, i.e, an electron-hole pair bounded by the Coulomb interaction similar to a hydrogenic atom, since the electron and hole have opposite charges. This exciton must be stable (i.e, it must have a large binding energy) in order to allow its diffusion until being disassociated at a hetero-interface (inter-facial dissociation) into a free electron in one material and a free hole on the other side [4]. For this reason, the search for materials which can form stable exciton is needed. Organic materials, monolayer (such as TMD's, Black phosphorus, and, our material of study, monolayer Tellurium) and quantum dots are excellent examples for high binding energy excitons [1, 4]. This suggest that we need to go further into low scale dimensional materials, thus, introducing us to the world of nano-technology and nano-optics.

1.1.1 Excitons

Excitons are quasiparticles formed inside solids constituted by an electron and a hole which are linked through Coulomb interaction. It happens when a photon collides with an electron in the valence band, causing it to jump into the conduction band and thus leaving a hole. This hole has positive charge and interacts with the electron, attracting it via the Coulomb interaction. If there exists a bound state, this quasi particle is called an exciton and has a binding energy lower than the free electron and hole ones [5, 6].

Depending on the dielectric constant of the material, excitons can be classified into Frenkel

or Wannier-Mott excitons. The first one is formed in materials where the dielectric constant is relatively small, in which the Coulomb interaction of the electron-hole pair is strong, consequently, the radius of the excitons are small (of the order of an unit cell) and have higher binding energy. On the other hand, Wannier-Mott excitons appear in materials with large dielectric constant, there the wavefunctions of the excitons spam several lattice spaces, resulting in low binding energies [7, 8].

According to the type of gap present in the material, the excitons are classified as direct or indirect ones. The direct ones such as GaAs, InP, CdTe and ZnTe conserve momentum whereas indirect ones can be formed either with emission or absorption of phonons for example [9]. Since the role of the excitons is more important at low temperatures, the emission process is more likely than the absorption one. Due to the large difference in crystal momentum between the lowest point of the conduction band and the highest of the valence band, the exciton may acquire a large center of mass momentum which corresponds to the absorved or emitted phonon. For the indirect exciton, a large range of crystal momentum values are possible and hence the energy levels spread out into bands, some materials that present this behaviour are Silicon and Germanium [6, 10].

One characteristic of the excitons explained above is that once formed, they tend to move freely in the crystal structure. Excitons thus play a key role in the industry, specially in light-induced processes such as light detectors, LEDs and lasers, photovoltaic generators and displays [4].

1.1.2 Tellurium Abundance

The cost production, availability and environmental friendly sources of the material employed are crucial factors for new solar cell technologies, a summary on the abundance of the constituents for Tellurium devices in comparison with other materials used in photovoltaic present devices is presented in this section [11]. This analysis is based on second generation thin film technology constituents such as cadmium, tellurium, gallium, indium, selenium and germanium [11] where the Cd-Te solar cell can give us a clue on what to expect for future technologies based on tellurium. These metals are produced as byproducts from the production of other materials such as aluminium, coal, copper and zinc [11]. Thus, there is an intrinsic dependence on the demand of the primary products, and, by analyzing the price-demand one can determine production dependencies. Table 1.1 is a summary of the world production for byproduct and primary commodities. From there one might conclude that it is unlikely to see an increase in production, e.g, it is unlikely that more coal will be mined and burned in order to recover germanium from ash, nor it is likely that more copper ore will be extracted to recover tellurium and more bauxite mined to recover more gallium during the production of aluminia [11]. At the same time, the amount of material needed for reaching a specific amount of GW per year for CIGS and CdTe PV films [11], the percentage

Byproduct commodity	**Primary commodities**	**World refinery production (in metric tons)**	**Price of refined metal (in dollars per kilogram)**
Cadmium	Zinc	16000	6
Gallium	Aluminium, Zinc	111	570
Germanium	Zinc, Coal	140	1490
Indium	Zinc	570	685
Selenium	Copper	3000-3500	71
Tellurium	Copper	450-500	211

Table 1.1: World production for byproducts, primary commodities where they come from, as well as world refinery production (in metric tons) of each byproduct and the price of the refined metal (in dollars per kilogram), extracted from [11].

that refineries produce for each metal and their corresponding costs are shown in table 1.2. In conclusion, Tellurium has a price below the average compared with other metals used in

Type of photovoltaic technology	**Metals required**			
	Metal	**Quantity (metric tons)**	**Percentage of 2008 estimated world refinery production from primary sources**	**Value of contained metal (in millions of dollars)**
Thin film CIGS	Gallium	30	27	17
	Indium	90	16	62
	Selenium	180	6	13
	total	300	49	92
Thin film CdTe	Cadmium	340	2	2
	Tellurium	390	82	82
	total	730	84	84

Table 1.2: Amount of metals required by PV technology CIGS and CdTe for producing a 8760 GWh/yr (Gigawatthours per year), the percentage production from primary sources and the value of the refined metals(in millions of dollars), extracted from [11]

thin film technology, and, the Gigawatts production for Cd-Te is half the price in comparison with CIGS thin film base materials. Furthermore, many alternatives for solving the demand of tellurium are presented such as the adoption of new government policies created to provide incentives for production, by increasing the values of the metals or that recycling rates of the byproduct commodities increase [11]. This initial analysis suggests that tellurium would be a nice candidate for PVs.

1.2 Nanotechnology

The history of nanotechnology comes from a distant past, starting 2000 years ago where sulfide nanocrystals were used by Greeks and Romans to dye hair, passing through the mid-

Structures	**Size (approx)**	**Materials**
Nanocrystals and clusters (quantum dots)	1 - 10 nm (diam.)	Metals, semiconductors, magnetic materials
Other nanoparticles	1 - 100 nm	ceramic oxides
Nanowires	1 - 100 nm (diam.)	Metals, semiconductors, oxides, sulfides, nitrides
Nanotubes	1 - 100 nm (diam.)	Carbon, layered metal chalcogenides
Nanoporus solids	0.5 - 10 nm (diam.)	Zeolites, phosphates
2D arrays (of nanoparticles)	Several nm^2 - μm^2	Metals, semiconductors, magnetic materials
Surfaces and thin films	1 - 100 nm (thickness)	A variety of materials
2D Monolayers	0.5 - 1 nm (thickness)	Metals, semiconductors insulators
3D structures (Superlattices)	Several nm in the three dimensions	Metals, semiconductors, magnetic materials

Table 1.3: Examples of nanostructures extracted from [12]

dle ages (1000 years ago) where gold nanoparticles were used to produce different colors in stained glass windows [12], and then becoming a real field of science with the advancement of experimental techniques that allowed for the controlled synthesis, assembly, visualization and spectroscopic assessment of matter at the atomic molecular scale. Since then, research and development applications has grown significantly.

It is impossible to talk about nanotechnology without first asking what makes nano special?. The answer lies in the sciences of chemistry, biology and quantum mechanics. On the one hand, typical sizes of molecules from a simple H_2 molecule to a complex protein lie in the nm scale. On the other hand, that is the typical scale where quantum mechanics starts to play a significant role. Thus, some of the most interesting quantum mechanical properties like superposition, absorption or spin interaction that are used in most of applications only happens at this scale. So then it becomes clear that a nanometer is a "magical" length scale point where technology meets atoms and molecules. It is worth to point that a nanoscopic object is thus a material where, at least, one of its dimensions falls in the nanometer scale (not necessarily all of them) [12, 13]. A few examples are organized in table 1.3. As it was pointed out, materials reduced to nano scale can show different properties compared to what they exhibit on macro-scale due to quantum mechanical effects, enabling unique applications. For instance, cooper which is an opaque substance, become transparent, platinum which is an inert material become a catalyst, aluminium which is a stable material turns combustible, silicon insulators became conductors and Gold which is solid, inert and yellow at room temperature becomes liquid and red [12]. Some size dependent properties listed above are shown in table 1.4.

Properties	Examples
Catalytic	Better catalytic efficiency through higher surface to volume ratio
Electrical	Increased electrical conductivity in ceramics and ceramic nanocomposites, increased electric resistance in metals.
Magnetic	superparamagnetism
Mechanical	Improved hardness and toughness of metals and alloys and ductility
Optical	Spectral shift of optical absorption and fluorescence properties, increased quantum efficiency of semiconductor nanocrystals.
Biological	Increased permeability through biological barriers (membranes)

Table 1.4: Size dependent properties extracted from [12]

1.3 2D Materials

The famous isolation of graphene, a single layer of graphite, in 2004 by Andre Geim and Konstantin Novoselov, opens the field of lower dimensionality materials [14]. The improved properties that graphite presents in the 2D compared to its 3D counterpart, led to a new field of research in those two-dimensional materials. In fact there is an ever expanding family of layered allotropes such as graphyne [14], borophene [15], germanene [16], silicene [17], phosphorene [18], stanene [19], bismuthene [20], molybdenite [21] to name a fewer. Even though a large number of 2D materials have been synthethized, and studied since then, we have not reach the theoretical prediction made in 2004 of 700 2D materials [22]. For this reason, the area of layered materials is a growing field and could potentially change electronics as we know. In the following sections I will describe some of the families of these layered materials and explain some intriguing properties unique about them.

1.3.1 Graphene

The prediction and study of graphene theoretically started in 1947 by P. R. Wallace as a text book example calculation for solid state physics. He predicted the electronic structure and noted the linear dispersion relation [14]. In 1956, the wave equation for excitations was written down by J. W. McClure and the similarity to the Dirac equation was first discussed by G. W. Semenoff, Di Vicenzo and Mele in 1984 [14].

Graphene consists of a single layer of carbon packed in a hexagonal (honeycomb) lattice, as it is made from carbon the importance of this 2D material grow immensely. Carbon is one of the most fascinating elements in the periodic table, it is the base for DNA and all forms of life on earth [14]. New forms of molecular carbon called fullerenes were discovered by space exploration and led to the award of the nobel prize in chemistry in 1996 [23]. Similarly, carbon nanotubes, quasi one dimensional form of carbon have been known theoretically for several decades since 1993 [14]. A point to be remarked is that graphene like structures were known theoretically since 1960's but there were experimental difficulties in isolating single layers in such a way that measurements could be done on them, it was even thought that

it would be practically impossible. So, it was somewhat surprise when Andre Geim, Konstantin Novoselov and their collaborators from the University of Manchester (UK), and the Insitute for Microelectronics Technology in Chernogolovka (Russia) presented their results on graphene in 2004. They manage to isolate graphene via an effective mechanical exfoliation method [14].

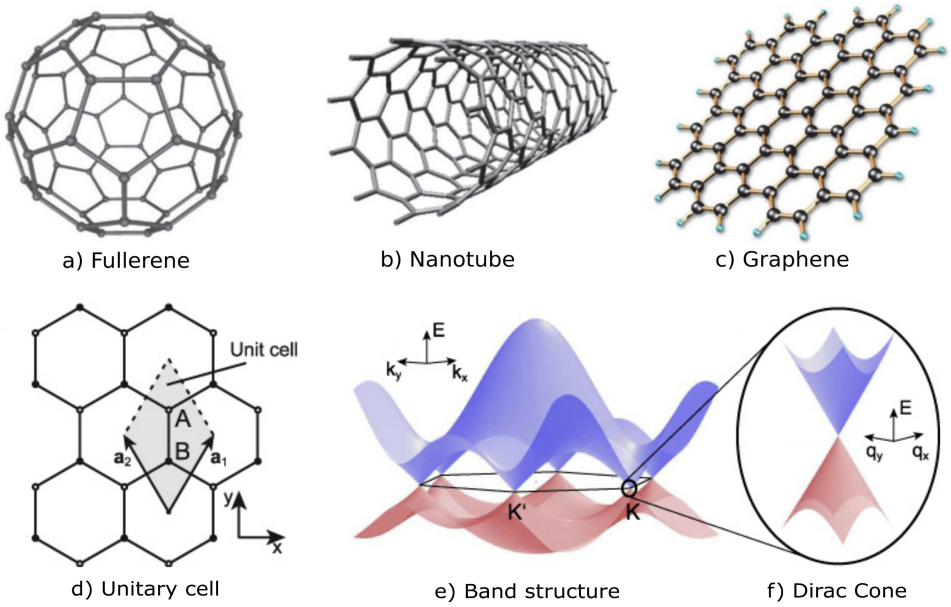

Figure 1.4: Different structures formed with grapehene: Fullerene (a), Nanotube (b) and Graphene sheet (c) extracted from [24]. Also, the unitary cell for the Honeycomb lattice (d), the 3D band structure of graphene, valence band and conduction band are pink and purple color respectively (e), and the (f) Dirac cone formed at the Fermi surface extracted from [25]

Characteristics of Graphene include transparency, it absorbs only 2.3% of visible light, hardness, it is more than 100 times stronger than the strongest steel, the electrical conductivity, which is slightly higher than copper, the thermal conductivity, which is dominated by phonons and has been measured to be 5000 $Wm^{-1}K^{-1}$, approximately 10 times more than copper at room temperature (401 $Wm^{-1}K^{-1}$) [14]. Furthermore, graphene band structure does not present a gap, the valence and conduction band met at a single point (figure 1.4-e) occasioning the so-called Dirac cones (figure 1.4-f) with zero effective masses for holes and electrons.

1.3.2 Transition Metal Dichalcogenides

Transition metal dichalcogenides (TMDs) are semiconductors of type ME_2 with M being a transition metal (like Mo,W) and X a chalcogen (S,Se,Te and Po). The structure consists of a 3 atomic layers, the central M layer lies in the middle of two layers of X atoms. Thus forming a honeycomb structure as showed in the figure 1.5 [**?**, 26]. Some features of these materials are: the direct band gap that could be used for electronic transistors and in optics as emitters detectors [27, 28, 29], the lack of inversion center of the crystal structure make a new

type of degree of freedom which emerges for charge carriers (opening a new branch called valleytronics) [30, 31, 32], and lastly, the strong spin-orbit coupling leads to an splitting of hundreds meV in the valence band and a few meV in the conduction band, which allows control of the electron spin (spintronics) [33]. Devices such as solar cells, LEDs, photodetectors, fuel cells and photocatalytic can be improved (smaller, cheaper and more efficient) with hetero-structures based on the combination of layers of TMDs, graphene and hexagonal boron nitride.

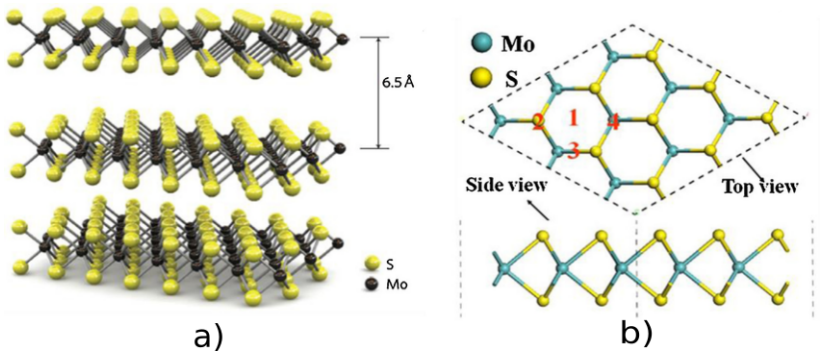

Figure 1.5: (a) Three dimensional MoS_2 structure Single layers separated by 6.5Å which can be extracted using scotch tape based micro-mechanical cleavage [26]. (b) Top and side views of MoS_2 monolayer where adsorption sites are showed with red numbers 1-4 extracted from [34].

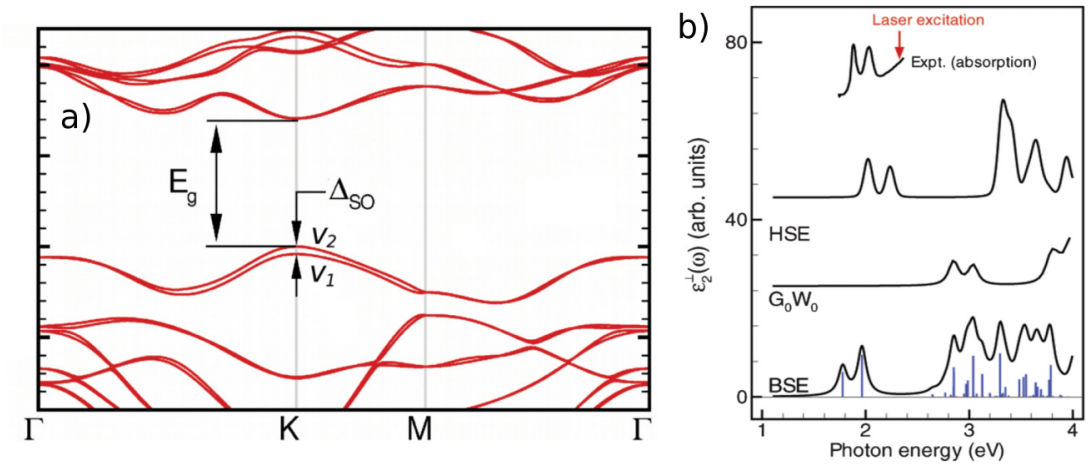

Figure 1.6: (a) Band structure of an MoS_2 monolayer, the splitting in the valence band is due to spin orbit coupling. Transitions between v_2 and v_1 and the CBM lead to the first two peaks in the absorption spectra (b) which corresponds to excitons [35]. The imaginary part of the dielectric constant as a function of photon energy is showed in (b) for three levels of theory (HSE, GW-RPA and BSE) as well as the experimental results [35]

TMDs like MoS_2 are good candidates for excitonic solar cells, since it present high binding energy excitons of the order of $1ev$ [35]. However, it happens that experimental results show two bright excitons for MoS_2 which can only be explained by the inclusion of spin-orbit coupling (SOC). The notorious splitting in the valence band (see figure 1.6) has an impact

then on excitonic binding energies. Now, the transitions occur between the degenerated states which led to new exciton formation (see the two peaks at figure 1.6-b) with binding energies of $1ev$ and $0.8ev$ [35]. This fact remarks that for heavy metals, the presence of SOC is necessary for having a good description of optics.

1.3.3 Transition Metal Monochalcogenides

It is also possible to obtain monolayers of the so called monochalcogenides (TMCs) . The members of this group obey the formula ME, where M is a transition metal and E a chalcogen such as S, Se, Te and Po. According to the group which transition metal belongs, there exists groups such as II ($M = Cd, Zn$) [36], III ($M = Ga, In$) [37] and IV ($M = Si, Ge, Sn$) [38, 39, 40]. The usual structures they acquire in the single layer is orthorhombic (SnSe, GeSe, GeS, SnS) [38, 39, 40] and in some cases hexagonal-honeycomb lattice (GaSe, InS, CdTe, ZnSe) [36, 38] as shown on figure 1.7. Each group of monochalcogenides has its own prop-

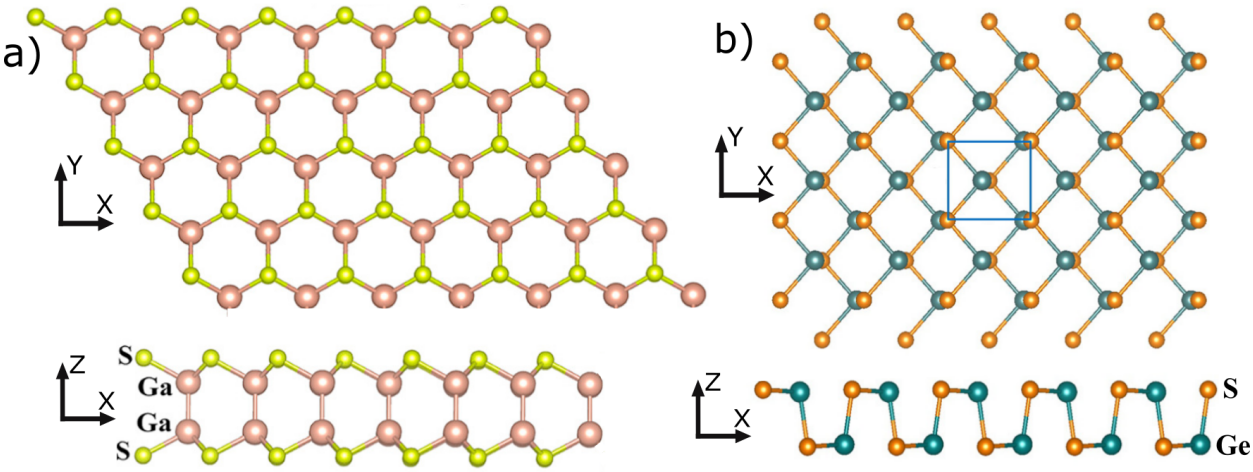

Figure 1.7: The hexagonal and orthorombic structures for monolayer monochalcogenides of GaS (a) and GeS (b) from top and side views extracted from [41, 38].

erties, i.e. Group II are know for the range of their band gaps varying from IR to UV with applications in photovoltaics and catalysis [36]. Group III TMCs have high carrier mobility, a layer dependent band gap as well as good electronic transport; making them promising candidates for electronic and optoelectronic devices such as field effect monolayer transistors (based on InSe) and photodetectors (made of GaS, GaSe, GaTe and InSe nanosheets), they also present promising piezoelectric and thermoelectric properties [37, 42]. Group IV TMCs present anisotropic optical, transport properties, flexibility, the ability to withstand enormous strain and giant piezoelectric effects; properties which allows potential applications such as nano-sized sensors and energy harvesting portable electronic devices [38, 39, 40].

An usual absorption spectra for group IV TMCs is detailed in figure 1.8 extracted from Gome et. al [40]. There we can see the anisotropy of the GeS monolayer for the the zigzag (zz, y direction) and armchair (ac, x direction) directions. The usual binding energy of excitons

in TMC's vary between 0.5 eV and 1 eV which make them good candidates for excitonic solar cells.

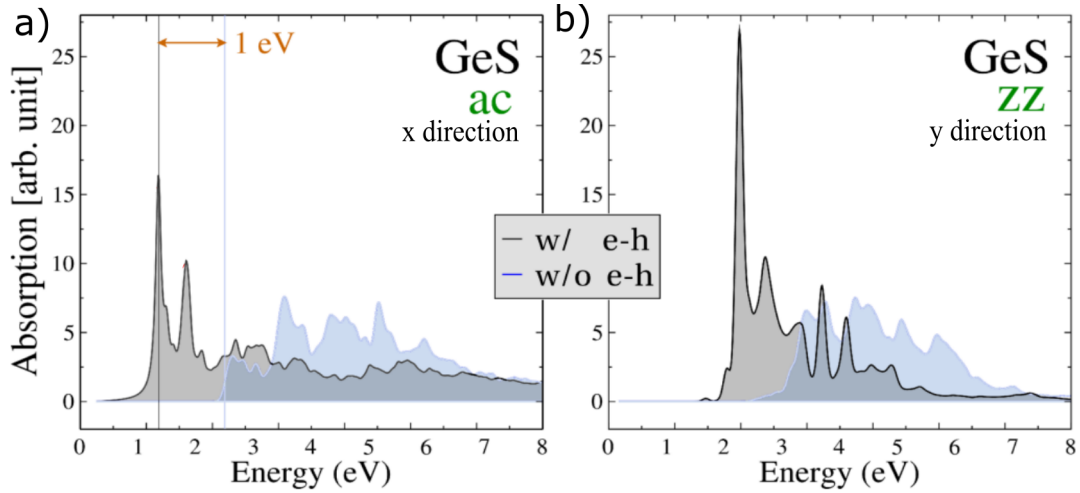

Figure 1.8: Absorption BSE spectra (gray spectrum) for germanium sulfide (GeS) monolayer in different directions: a) zigzag (y dir.) and b) armchair (x dir.) extracted from [40].

1.3.4 Phosphorene

Phosphorus has emerged as a new 2D material due to the properties that enhance one of its phases, the black phosphorus, which present a direct band gap varying from the infrared through the visible range, peculiar electrical, vibrational, optical and thermal properties. Thus, making it one of the important candidates for the development of photodetectors and solar energy storage devices [18, 43]. Since black phosphorus is layered, it can be exfoliated to obtain the monolayer called as phosphorene [44, 45]. In addition one can distort phosphorene to get the hexagonal structure of blue phosphorene (see figure 1.9) [43]. Phosphorene has the same structure as the 2D transition metal monochalcogenides: it has a puckered structure in the armchair direction, while it appears bilayer in the zigzag direction [18]. This unique structural arrangement gives origin to its famous anisotropy in physical properties such as band structure [46], electrical transport [47], thermoeletrics [48]; and mechanical such as critical strain [49], Poisson's ratio [50] and Young's modulus [51]. This has led the design of devices which can explode this directional selectivity (e.g. Phosphorene based FET [45, 46]).

The band structure and optics of black phosphorene are clear examples of the anisotropy. Firstly, in table 1.5 we can see that the difference from effective masses of the electrons (m) and holes (M) in the x and y directions represents the anisotropy of the band structure. Secondly, the figure 1.10 shows that the BSE spectrum in the zigzag (y) direction contain a bright exciton with a binding energy of 0.75 eV; however, no excitons are formed if the armchair (x) direction is chosen [43]. Thus, phosphorene is a good candidate for excitonic solar cells since it can form stable and direction dependent excitons.

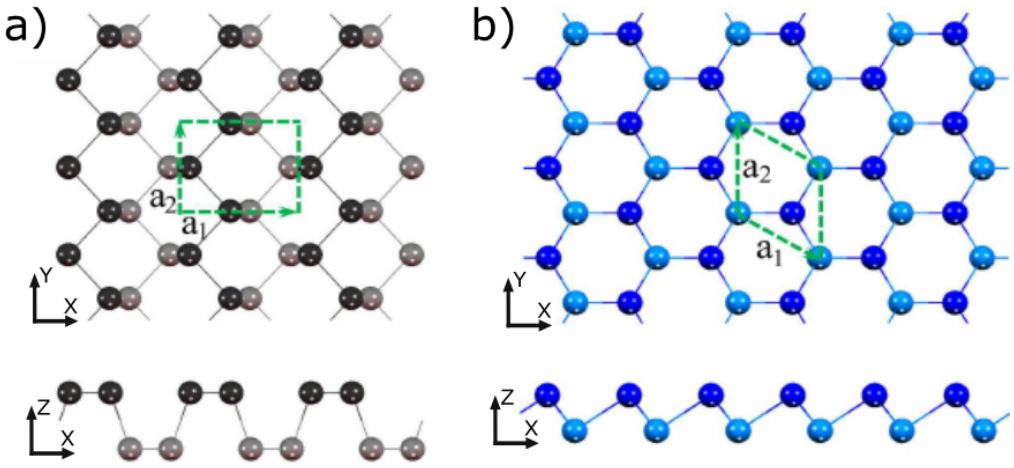

Figure 1.9: Monolayer phosphorus allotropes from top and side views: (a) blue and (b) black phosphorene extracted from [52].

m_x	m_y	M_x	M_y
0.14	1.23	0.13	7.78

Table 1.5: Effective masses of the valence (M) and conduction band (m) of black phosphorene in different directions extracted from [43]

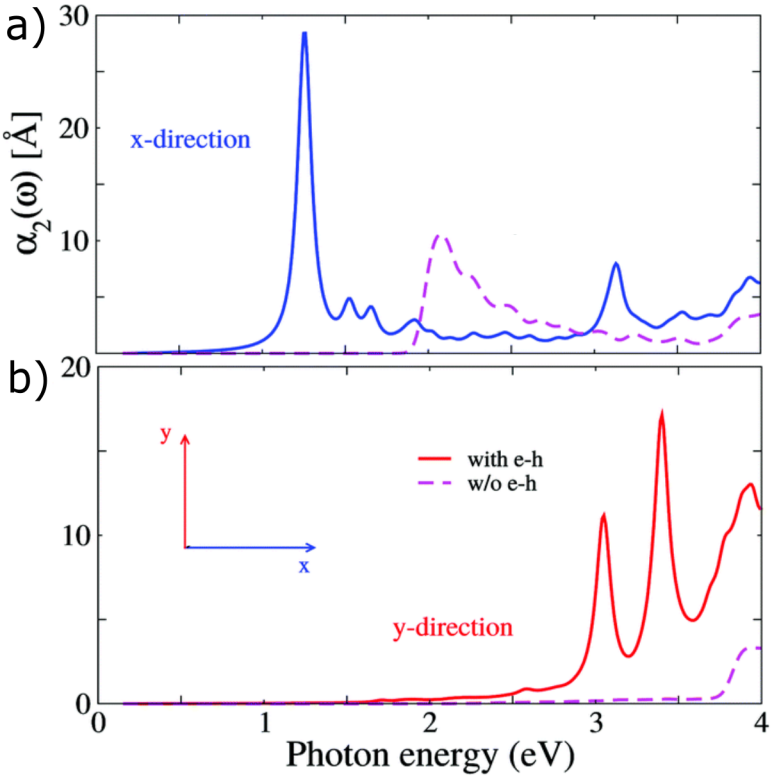

Figure 1.10: Absorption BSE spectra (blue and red) for black phosphorene in different in the zigzag (y) direction (a) and armchair (x) direction extracted from [43].

1.4 Tellurium

As similar to S, Se and Po, Te is a member of the chalcogenides. Its different 2d phases that will be discussed here would enter in the range of layered monochalcogenides (group VI). Tellurium was discovered within gold ores in 1780's in Transylvania, it is a semiconductor and its a rare material compared in abundance to gold. The primary use of Tellurium is for manufacturing films essential to photovoltaic solar cells. The common way for enhancing electrical conductivity is by alloying it with Cadmium. Furthermore, as an additive to steel and copper, tellurium improves machine efficiency, specially in thermoelecric cooling applications where it improves ductibility and tensile strength; and help prevent sulfuric acid corrosion. Both, the photovoltaic and thermoelectric applications cover the two-thirds of global tellurium consumption. Most tellurium used today is indirectly mined, as it is recovered as a byproduct of milled copper, gold and iron. The only mines focused on tellurium are located in China, the Dashuigou and Majigou, and Sweden at the Kankberg deposit, those deposit accounts for 15% annual production of tellurium.

1.4.1 Tellurene Phases

The first theoretical prediction of tellurene comes in a paper published on september 2017 by Zhili Zhu and Xialoin Cai [53, 54]. In their research they show, by terms of simulation and partially experimental, that layered tellurene can exists in three different phases: αTe (formed via thickness-dependent process), βTe (extracted from exfoliation process) and γTe (formed by distorting α-Te). Following studies comes from november 2017 until now, for example: the behavior of few layer Tellurene [55], the thermoelectric properties of the βTe phase [56], the effects that adatom and gas molecule adsorption has [57], the behavior of the excited states when the dimension is reduced [58], the synthesization in solution [59], by exfoliation [60], and on graphene [61].

All the phases has similar structural features, in particular tellurene has common bonding characters with other group-VI elements, where the nonmetallic character is weakened in the order of O > S > Se > Te, leading to a complete metallic character of Po [53]. For this reason, Te has the dual characteristics of both metal and nonmetal. Consequently, the two dimensional monolayers of Te adopt the trilayer atomic structures, i.e., a MoS_2-like structure (e.g, α-Te has an hexagonal symmetry like $1T - MoS_2$, while γ-Te is $2H - MoS_2$ like) [53]. Each tellurene phase posses three layers of atoms due its multivalency nature of Te, the central layer behaves more metal like meanwhile the outer layers more as a semiconductor [53]. This semiconductor characteristic is highlight in α-Te and β-Te phases, while the γ-Te show a metal behavior. Lastly, the optical absorption on tellurene has been studied in [58, 61], which will be addressed in detail on chapter 4.

1.5 Computational Physics

Up until the mid 20^{th} century, physics has relied on two main branches, theoretical and experimental. Ones models calculations using analytical methods that can be related to experimental data. However, with development of computers since world war II (the first large scale deployment was during the Manhattan project), it is possible nowadays to conceive of another branch, the computational one [62]. In particular, as we aim to simulate materials specific properties with high precision by solving the Schrodinger equation (or using other equivalent methods) for large number of particles, this can only be achieved with state of the art high performance computing tools.

In particular, density functional theory (DFT) [63] has become the work horse of atomistic simulations with the ideal balance between accuracy and efficiency. It provides information (both structural as well as the energetics) of molecules and solids in the ground state. The approximations inherent to the method as well as the fundamental concepts prevent it from being directly used for obtaining optical properties. Nonetheless one can use DFT as a starting point for a more accurate many body calculation where the single-particle excitations are obtained [64] and furthermore the electron-hole correlations, that form the exciton, can be further included via the so called Bethe-Salpeter equation (BSE) [65].

Open source codes for DFT calculations are, e.g, Siesta [66] and Quantum-Espresso [67]. And, for optics there are packages such as Berkeley-GW [68] and Yambo [69]. Since DFT is written in terms of the electron density of states, its calculations are not too demanding in contrast to optics (RPA and BSE) where the sums over bands and k-points in the Brillouin zone (BZ) makes the calculation heavy (talking in terms of number of processors and time consumed). However, one can reproduce part of the results obtained in BSE, i.e, the excitonic binding energies and wavefunctions, using an effective model (for this case a Hydrogen effective model). This help us to obtain specific information of the system quicker. For this reason, the development of effective models helps us to simplify and to have a better understanding of complex systems.

1.6 Thesis Scheme

As it was pointed in section 1.3, monolayers are good candidates for excitonic solar cells since they can form stable (high binding) excitons. And, from section 1.1 we can infer that Tellurium is a good material in terms of efficiency and cost in solar cell industry. For this reason, we address our study in low dimensional Tellurium, tellurene. Particularly, in the absorption of the three phases in order to find which is more suitable to harbor excitons. For this reason, we organize the following chapters in this way:

Chapter 2 details the necessary theoretical concepts for understanding the exciton formation in a monolayer, this enrolls density functional theory for structural properties (Quan-

tum Espresso), linear response theory for optical absorption in the IPA and RPA levels of theory, quasi particle many body perturbation theory (QPMBPT) for energy corrections in the band structure (the GW approximation), and the Bethe Salpeter equation for exciton wave functions and binding energies. And, in the last section we make an emphasis on how this theory was implemented in Yambo's code and why they are so consuming.

Chapter 3 talks about an effective model for excitons which will help to predict the binding energy and wave functions in a quicker and more efficient way. In this model, the exciton is thought as a two-dimensional particle conformed by an electron and hole which interacts via the screened Coulomb potential. For this reason, we talk about the 2D screned potential, 2D polarizability and the solution of a 2D Schrodinger equation for the isotropic and anisotropic cases. Lastly, a computational approach is given thanks to the Numerov method.

Chapter 4 focus on the analysis of the results on the bulk-Te and the three tellurene phases: Those coming from Quantum Espresso calculations such as the relaxed structures, band-structures, density of states, phonon stabilities; the ones developed on Yambo such as quasiparticle band-structures (in the GW approximation), and optics in the different levels of theory, i.e, independent particle approximation (IPA), random phase approximation (RPA) and Bethe Salpeter equation (BSE); and, the calculations coming from the effective hydrogen model. Lastly, we compare the wave functions and binding energy of excitons results coming from the quasiparticle many body (QPMBPT) picture with the effective model.

CHAPTER 2

Theoretical Concepts

Since we are interested in the calculation of the properties of realistic systems, we need to provide a theoretical framework for the accurate prediction of structural and electronic properties of both, the ground state as well as excited states. In this sense, density functional theory (DFT) [70, 71] works well for extracting the bandstructure of interacting systems, time dependent density functional theory (TDDFT) [72] gives birth to the response function that the system has due to small perturbations, thus providing an approach to calculate the dielectric constant in the independent particle approximation (IPA) and random phase approximation (RPA) levels of theory. The GW approximation in the framework of many body perturbation theory (MBPT) gives a shift to the value of the band structure in the DFT case by using the Hedin's equations [73], and so, going closer to experiment results. Lastly, the Bethe Salpeter equation (BSE) [74] uses this GW results to get the dielectric constant with the inclusion of two particle green function for electron and hole interaction. In effect, this corresponds to the calculation of the optical absorption of a particular system with the possibility of exciton formation. In what follows we will discuss the theoretical framework used in this dissertation.

2.1 Density Functional Theory

2.1.1 Schrodinger equation for many body systems

Let's begin with the description of a system with N electron moving in an external potential v_{ext} (electron-ion interaction):

$$\left(-\frac{1}{2}\sum_{i=1}^{N}\nabla^2_{\mathbf{r}_i}+\frac{1}{2}\sum_{i\neq j}\frac{1}{|\mathbf{r}_i-\mathbf{r}_j|}+\sum_i v_{\text{ext}}(\mathbf{r}_i,\mathbf{R})+E_{ion}(\mathbf{R})\right)\Psi(\mathbf{r})=E\Psi(\mathbf{r}), \tag{2.1}$$

where the energy depends on the ionic coordinates as well as the electron positions (for spin orbit case a dependence of the energy on spin needs to be included). In the derivation of equation (2.1), the Born-Oppenheimer approximation was used (where the kinetic term corresponding to the ions vanishes due to its large mass compared with the electrons [63]). The term E_{ion} can be neglected as well for a fixed ionic configurations (*i.e.*, the energy calculated will just differ by a constant) [63, 75]. So, the electronic Hamiltonian reads:

$$\begin{aligned}\hat{H}&=-\frac{1}{2}\sum_{i=1}^{N}\nabla^2_{\mathbf{r}_i}+\frac{1}{2}\sum_{i\neq j}\frac{1}{|\mathbf{r}_i-\mathbf{r}_j|}\sum_i v_{\text{ext}}(\mathbf{r}_i),\\ \hat{H}&=\hat{T}+\hat{V}_{ee}+\hat{V}_{\text{ext}}.\end{aligned} \tag{2.2}$$

Instead of solving the eigenvalue problem for $\hat{H}$, it is easier to find the ground state wave function Ψ_0 and energy E_0 using the variational principle. This states that the energy computed from a guessed Ψ will be an upper bond to the true ground state energy E_0. For this

reason, a minimization of the energy $E[\Psi]$ with respect to the many-electron wave function [75], $\Psi(\mathbf{r}) = \Psi(\mathbf{r}_1, \mathbf{r}_2, ..., \mathbf{r}_N)$, needs to be done, *i.e.*,

$$E[\psi] = \frac{\langle \Psi | \hat{H} | \Psi \rangle}{\langle \Psi | \Psi \rangle}, \quad \langle \Psi | \Psi \rangle = 1, \tag{2.3}$$

$$\frac{\delta E}{\delta \Psi} = 0. \tag{2.4}$$

This equation will theoretically yield the ground state, but, in practice this task is only achieved for few electrons [75]. When the system has thousands of particles, the complexity of the wave function makes this problem intractable due to the large number of degrees of freedom. For this reason, it is convenient to search quantities more compact to make calculations easier [75]. The most successful candidate is the electron density [63, 75, 76] defined as:

$$n(\mathbf{r}) = N \int d^3 r_2 d^3 r_3 ... d^3 r_N \Psi^*(\mathbf{r}, \mathbf{r}_2, ..., \mathbf{r}_N) \Psi(\mathbf{r}, \mathbf{r}_2, ..., \mathbf{r}_N), \tag{2.5}$$

which can also be written as:

$$n(\mathbf{r}) = \langle \Psi | \hat{n}(\mathbf{r}) | \Psi \rangle, \text{ with the density operator: } \hat{n}(\mathbf{r}) = \sum_i^N \delta(\mathbf{r} - \mathbf{r}_i). \tag{2.6}$$

The concept related to the density is that it describes the probability to find an electron at a position $\mathbf{r}$ by integrating all other out electrons, thus, containing less information than the full $N-1$ many-body wavefunction $\Psi(\mathbf{r})$ (it requires only three spatial coordinates in comparison with the 3N degrees of freedom of the wave function) [63, 75]. Before going deeply into why choosing the density operator, *i.e.*, the Honhenberg-Kohn theorem, lets find the density formulation of each of the terms entering in the ground state energy [75]:

$$E = \langle \Psi | \hat{T} | \Psi \rangle + \langle \Psi | \hat{V}_{ee} | \Psi \rangle + \langle \Psi | \hat{V}_{\text{ext}} | \Psi \rangle. \tag{2.7}$$

The energy contribution due to the external potential is given by

$$\begin{aligned} \langle \Psi | \hat{V}_{\text{ext}} | \Psi \rangle &= \sum_{i=1}^N \int d^3 r_1 d^3 r_2 ... d^3 r_N \Psi^*(\mathbf{r}_1, \mathbf{r}_2, ..., \mathbf{r}_N) v_{\text{ext}}(\mathbf{r}_i) \Psi(\mathbf{r}_1, \mathbf{r}_2, ..., \mathbf{r}_N), \\ &= N \int d^3 r d^3 r_2 ... d^3 r_N \Psi^*(\mathbf{r}, \mathbf{r}_2, ..., \mathbf{r}_N) v_{\text{ext}}(\mathbf{r}) \Psi(\mathbf{r}, \mathbf{r}_2, ..., \mathbf{r}_N), \\ &= \int d^3 r \, v_{\text{ext}}(\mathbf{r}) n(\mathbf{r}), \end{aligned} \tag{2.8}$$

and is only dependent on $n(\mathbf{r})$. Similarly, the kinetic energy is:

$$\begin{aligned}\langle\Psi|\,\hat{T}\,|\Psi\rangle &= -\frac{1}{2}\sum_{i=1}^{N}\int d^3r_1 d^3r_2 ... d^3r_N \Psi^*(\mathbf{r}_1,\mathbf{r}_2,...,\mathbf{r}_N)\nabla^2_{\mathbf{r}_i}\Psi(\mathbf{r}_1,\mathbf{r}_2,...,\mathbf{r}_N),\\ &= -\frac{N}{2}\int d^3r' d^3r d^3r_3 ... d^3r_N \delta(\mathbf{r}-\mathbf{r'})\Psi*(\mathbf{r'},\mathbf{r}_2,...,\mathbf{r}_N)\nabla^2_{\mathbf{r}}\Psi(\mathbf{r},\mathbf{r}_2,...,\mathbf{r}_N),\\ &= -\frac{1}{2}\int d^3r' d^3r \delta(\mathbf{r}-\mathbf{r'})\nabla^2_{\mathbf{r}}\gamma(\mathbf{r},\mathbf{r'}) = -\frac{1}{2}\int d^3r [\nabla^2_{\mathbf{r}}\gamma(\mathbf{r},\mathbf{r'})]_{\mathbf{r'}=\mathbf{r}},\end{aligned} \tag{2.9}$$

where $\gamma(\mathbf{r},\mathbf{r'})$ is the one particle density function:

$$\gamma(\mathbf{r},\mathbf{r}') = N\int d^3r_2 d^3r_3 ... d^3r_N \Psi^*(\mathbf{r'},\mathbf{r}_2,...,\mathbf{r}_N)\Psi(\mathbf{r},\mathbf{r}_2,...,\mathbf{r}_N). \tag{2.10}$$

Finally, the electron-electron interaction links the coordinates of every two electrons [75]:

$$\begin{aligned}\langle\Psi|\,\hat{V}_{ee}\,|\Psi\rangle =& \frac{1}{2}\sum_{i\neq j}\int d^3r_1 d^3r_2 ... d^3r_N \Psi^*(\mathbf{r}_1,\mathbf{r}_2,...,\mathbf{r}_N)\frac{1}{|\mathbf{r}_i-\mathbf{r}_j|}\Psi(\mathbf{r}_1,\mathbf{r}_2,...,\mathbf{r}_N),\\ =& \frac{N(N-1)}{2}\int d^3r_1 d^3r_2 \frac{1}{|\mathbf{r}_i-\mathbf{r}_j|}\int d^3r_3 ... d^3r_N \Psi^*(\mathbf{r}_1,\mathbf{r}_2,...,\mathbf{r}_N)\Psi(\mathbf{r}_1,\mathbf{r}_2,...,\mathbf{r}_N),\\ =& \frac{1}{2}\int d^3r_1 d^3r_2 \frac{n^2(\mathbf{r}_1,\mathbf{r}_2)}{|\mathbf{r}_1-\mathbf{r}_2|},\end{aligned} \tag{2.11}$$

where $n^2(\mathbf{r}_1,\mathbf{r}_2)$ is the pair density which is defined as the trace of the two density matrix $\Gamma(\mathbf{r}_1,\mathbf{r}_2,\mathbf{r}_1,\mathbf{r}_2)$:

$$\Gamma(\mathbf{r}_1,\mathbf{r}_2,\mathbf{r'}_1,\mathbf{r'}_2) = N(N-1)\int d^3r_3 ... d^3r_N \Psi^*(\mathbf{r}_1,\mathbf{r}_2,...,\mathbf{r}_N)\Psi(\mathbf{r'}_1,\mathbf{r'}_2,...,\mathbf{r}_N). \tag{2.12}$$

The classical electrostatic energy (Hartree term) is hidden in equation (2.12) and has the form:

$$E_H = \frac{1}{2}\int d^3r d^3r' \frac{n(\mathbf{r})n(\mathbf{r'})}{|\mathbf{r}-\mathbf{r'}|}. \tag{2.13}$$

If this Hartree term is subtracted from (2.12), the exchange correlation term $n_{xc}(\mathbf{r}_1,\mathbf{r}_2)$ emerges [75],

$$n_{xc}(\mathbf{r}_1,\mathbf{r}_2) = \frac{n^2(\mathbf{r}_1,\mathbf{r}_2)}{n(\mathbf{r}_1)} - n(\mathbf{r}_2). \tag{2.14}$$

The total energy of the system is therefore:

$$E = -\frac{1}{2}\int d^3r [\nabla^2_{\mathbf{r}}\gamma(\mathbf{r},\mathbf{r'})]_{\mathbf{r'}=\mathbf{r}} + \frac{1}{2}\int d^3r d^3r' \frac{n(\mathbf{r})n(\mathbf{r'})}{|\mathbf{r}-\mathbf{r'}|} + \frac{1}{2}\int d^3r d^3r' \frac{n(\mathbf{r})n_{xc}(\mathbf{r},\mathbf{r'})}{|\mathbf{r}-\mathbf{r'}|} + \int d^3r\, v_{\text{ext}}(\mathbf{r})n(\mathbf{r}). \tag{2.15}$$

This equation suggests that there exists a way to calculate the energy using the charge density, the method is called density functional theory (DFT) and has its bases in Hohenberg-

Kohn theorem [75, 76, 63].

2.1.2 Hohenberg-Kohn Theorem

DFT has its basis held on the shoulders of two theorems proved by Hohenberg and Kohn (HK) in 1964 [70], and later generalized by Levy [75]. The first theorem states that
"The electron nucleus interaction $\hat{V}_{ext}$ is a unique functional of $n(\mathbf{r})$; since in turn $\hat{V}_{ext}$ determines $\hat{H}$, it can be seen that the full many particle ground state is a functional of $n(\mathbf{r})$" [63, 76].
In practice this means they introduced the energy functional

$$E_{HK}[n] = F[n] + \int d^3 n(\mathbf{r})\, v_{\text{ext}}(\mathbf{r}), \;\; F[n] = \langle \Psi | \, \hat{T} + \hat{V}_{ee} \, | \Psi \rangle \,, \tag{2.16}$$

and proved that $F[n]$ is an unique functional of density $n(\mathbf{r})$ [75] (remember this term is independent of the system treated; it could be applied to the hydrogen atom as well as large molecules [76]), *i.e.*, for an N electron system, there are no two ground state wavefunctions $\Psi_1 \neq \Psi_2$ resulting in the same density $n(\mathbf{r})$ [75].

The second theorem states that
"$F[n]$, the functional that derives the ground state energy of the system, delivers the lowest energy if and only if the input density is the true ground state density" [63, 76].
This tell us that $E_{HK}[n]$ obeys the variational principle and gives energies always at or above the ground state energy E_0 [75],

$$E_{HK}[n] \geq E_0, \tag{2.17}$$

unless the true ground state density n_{GS} is given,

$$E_{HK}[n_{GS}] \geq E_0. \tag{2.18}$$

2.1.3 Kohn-Sham Approach

The Honhenberg-Kohn (HK) theorem gives a theoretical justification for the construction of the energy functional in terms of the density, however, it does not give us the correct form of the functional $F[n]$ [75, 76]. It is important to point that Thomas and Fermi proposed a functional in terms of the density before HK theorem. They considered three terms [63, 76]: the kinetic energy, which was formed by taking into account the homogeneus electron gas,

$$\hat{T}[n](\mathbf{r}) = \frac{3}{10}(3\pi^2)^{2/3} \int d^3 r\, n^{5/3}(\mathbf{r}), \tag{2.19}$$

the electron-electron interaction is just the hartree term:

$$\hat{V}_{ee}[n](\mathbf{r}) = \frac{1}{2} \int d^3 r\, d^3 r' \frac{n(\mathbf{r})\, n(\mathbf{r'})}{|\mathbf{r} - \mathbf{r'}|}, \tag{2.20}$$

and the Coulomb interaction between electron-ion:

$$\hat{V}_{\text{ext}}[n](\mathbf{r}) = \int d^3r\, v_{\text{ext}}(\mathbf{r})n(\mathbf{r}). \tag{2.21}$$

Even though the Thomas-Fermi model seems ok, it does not predict a number of properties, *e.g.*, the binding energies of atoms to form molecules and solids [63, 75].

In 1965, Kohn and Sham proposed a different approach for the functional $F[n]$ that maps the problem of a system of interacting particles into a system of independent electrons (non interacting) with the same density $n(\mathbf{r})$ in an effective local potential that mimics the influence of the other electrons[63, 71, 75, 76]. The HK energy then can be described as:

$$E[n] = T_s[n] + E_H[n] + E_{xc}[n] + E_{\text{ext}}[n], \tag{2.22}$$

where

$$E_{xc}[n] = \langle \Psi_{MB}|\, \hat{T}\, |\Psi_{MB}\rangle - T_s[n] + \langle \Psi_{MB}|\, \hat{V}_{ee}\, |\Psi_{MB}\rangle - E_H[n], \tag{2.23}$$

in which the true interacting wave function is denoted as Ψ_{MB}, meanwhile the wavefunction of the reference system of non-interacting particles is a Slater determinant built from one-electron wavefunctions ψ_n [75, 76]. The kinetic energy of the independent particles is represented in $T_s[n] = 1/2\sum_n |\psi_n\rangle \nabla^2 \langle\psi_n|$ and depends on the electron density [63, 75, 76] $n(\mathbf{r})$:

$$n(\mathbf{r}) = 2\sum_n |\psi_n(\mathbf{r})|^2. \tag{2.24}$$

With the definition of the Hartree potential

$$v_H[n](\mathbf{r}) = \int d^3r' \frac{n(\mathbf{r'})}{|\mathbf{r}-\mathbf{r'}|}, \tag{2.25}$$

and the artificial exchange potential $v_{xc}[n]$, the energy becomes:

$$\begin{aligned} E[n] =& T_s[n] + \int d^3r\, n(\mathbf{r})\left[\frac{1}{2}v_H[n](\mathbf{r}) + v_{xc}[n](\mathbf{r}) + v_{\text{ext}}[n](\mathbf{r})\right], \\ =& T_s[n] + \int d^3r\, n(\mathbf{r})\, v_{KS}[n](\mathbf{r}), \end{aligned} \tag{2.26}$$

where $v_{KS}[n](\mathbf{r})$ is the Kohn-Sham potential [63, 75, 76]. The ground state energy can be obtained by the minimization of (2.26) giving birth to the Kohn-Sham equations [63, 75, 76]:

$$\begin{aligned} \left(-\frac{1}{2}\nabla^2 + v_{KS}[n](\mathbf{r}) + \int d^3r\, n(\mathbf{r})\frac{\delta v_{KS}[n]}{\delta n(\mathbf{r'})}\right)\psi_n = \epsilon_n\psi_n, \\ \left(-\frac{1}{2}\nabla^2 + v_H[n](\mathbf{r}) + v_{xc}[n](\mathbf{r}) + v_{\text{ext}}(\mathbf{r})\right)\psi_n = \epsilon_n\psi_n, \\ \left(-\frac{1}{2}\nabla^2 + v_{\text{eff}}[n](\mathbf{r})\right)\psi_n = \epsilon_n\psi_n, \end{aligned} \tag{2.27}$$

where the exchange correlation $v_{xc}[n](\mathbf{r})$ is defined as:

$$v_{xc}[n](\mathbf{r}) = \frac{\delta E_{xc}[n]}{\delta n(\mathbf{r})}. \tag{2.28}$$

Due to the dependence of the KS Hamiltonian on the density and this on the wavefunctions themselves, the Kohn-Sham equations (2.27) are self consistent and must be solved iteratively. It is important to point out that if v_{xc} is known, then the KS scheme would lead to the exact result [63, 75, 76].

The Kohn-Sham density functional theory gives the ground state energy and ground state density by solving a set of one-electron like Schrodinger equations [63]. However, the exchange-correlation energy functional $E_{xc}[n]$ have to be approximated. The earliest approach is called local density approximation (LDA) and assumes that the exchange correlation can be locally approximated to the exchange correlation energy density per particle $\epsilon_{xc}^{\text{unif}}[n]$ of an uniform electron gas [63, 75, 76],

$$E_{xc}[n(\mathbf{r})] = \int d^3r\, n(\mathbf{r})\epsilon_{xc}^{\text{unif}}[n], \tag{2.29}$$

where the term $\epsilon_{xc}^{\text{unif}}[n]$ can be split in two parts,

$$\epsilon_{xc}^{\text{unif}}[n] = \epsilon_{x}^{\text{unif}}[n] + \epsilon_{c}^{\text{unif}}[n], \tag{2.30}$$

in which, the exact exchange energy was derived by Bloch and Dirac,

$$\epsilon_{x}^{\text{unif}}[n] = -\frac{3}{4}\left(\frac{3n}{\pi}\right)^{1/3}. \tag{2.31}$$

For the full exchange correlation of the homogeneus electron gas, a derivation using quantum Monte Carlo methods has been done by Ceperly and Alder et. al, [75].

Another approach to find the exchange-correlation energy is done wiht the generalized gradient approximation (GGA) in which the density and the variation of the density (gradient) is considered:

$$E_{xc}^{GGA}[n] = \int d^3r\, f(n, \nabla n). \tag{2.32}$$

These GGA functionals can be constructed as to fulfill specific conditions, or by fitting to energies calculated on a higher levels of theory or experimental values [63, 75]. The GGA that will be used along the calculations of chapter 4 corresponds to the first class of GGAs and was developed by Perdew, Burke and Ernzerhof (PBE) [63, 77].

2.2 Optical Properties within Linear Response Theory

2.2.1 Time Dependent Density Functional Theory (TDDFT)

The objetive of time dependent density functional theory is to map the time dependent Schrodinger equation:

$$i\frac{\partial\Psi(t)}{\partial t} = \hat{H}\Psi(t), \tag{2.33}$$

into an effective one electron problem (similar to what DFT does for the static schrodinger equation). In 1984, Runge and Gross proved that for a given initial state, a correspondence exists between the time dependent density $n(\mathbf{r},t)$ and the time dependent external potential $v_{\text{ext}}(\mathbf{r},t)$. The Runge-Gross theorem is the basis of TDDFT akin to the Hohenberg-Kohn theorem for DFT [78]. In the same way as it was done in DFT, a set of time dependent Kohn-Sham equations can be introduced, which maps the problem of interacting electrons moving in a time dependent external potential v_{ext} into a system of independent electrons moving in a time dependent effective potential v_{eff} [78]. The time dependent Kohn-Sham equation acquires the form:

$$i\frac{\partial\psi_n(\mathbf{r},t)}{\partial t} = \left[\frac{1}{2}\nabla^2 + v_{\text{eff}}[n](\mathbf{r},t)\right]\psi_n(\mathbf{r},t), \tag{2.34}$$

and, the time-dependent density:

$$n(\mathbf{r},t) = 2\sum_n |\psi_n(\mathbf{r},t)|^2, \tag{2.35}$$

where the effective potential is the sum of the time dependent external potential, Hartree potential and exchange correlation potential as in the DFT case [78]:

$$v_{\text{eff}}[n](\mathbf{r},t) = v_{\text{ext}}(\mathbf{r},t) + v_H[n](\mathbf{r},t) + v_{xc}[n](\mathbf{r},t), \tag{2.36}$$

with the time dependent Hartree potential

$$v_H[n](\mathbf{r},t) = \int d^3r' \frac{n(\mathbf{r'},t)}{|\mathbf{r}-\mathbf{r'}|}. \tag{2.37}$$

The time dependent exchange correlation potential v_{xc} depends on the history of the density $n(\mathbf{r},t)$, the Kohn-Sham wavefunctions and the initial state of the interacting system [78].

2.2.2 Linear response Theory

The response of the material to an external weak perturbation (compared to the internal electric fields caused by the ions) is encoded in the response function $\Pi(\mathbf{r},\mathbf{r'},t,t')$. This describes the change of the density δn at $(\mathbf{r},t)$ if the external potential undergoes a small

change at $(\mathbf{r'}, t')$ [78]

$$\delta n(\mathbf{r}, t) = \int dt' d^3 r' \Pi(\mathbf{r}, \mathbf{r'}, t, t') \delta v_{\text{ext}}(\mathbf{r'}, t'), \tag{2.38}$$

$$\Pi(\mathbf{r}, \mathbf{r'}, t, t') = \frac{\delta n(\mathbf{r}, t)}{\delta v_{\text{ext}}(\mathbf{r'}, t')}. \tag{2.39}$$

In the Kohn-Sham TDDFT formulation, the response function $\Pi^{KS}(\mathbf{r}, \mathbf{r'}, t, t')$ measures the response of the KS system to a small change of the effective Kohn-Sham potential [78]:

$$\delta n(\mathbf{r}, t) = \int dt' d^3 r' \Pi^{KS}(\mathbf{r}, \mathbf{r'}, t, t') \delta v_{\text{eff}}[n](\mathbf{r'}, t'), \tag{2.40}$$

$$\Pi^{KS}(\mathbf{r}, \mathbf{r'}, t, t') = \frac{\delta n(\mathbf{r}, t)}{\delta v_{\text{eff}}[n](\mathbf{r'}, t')}. \tag{2.41}$$

Due to the origin of equations (2.38) and (2.40) (both measuring the change of the density), they must be equal, linking this way the response function of the interacting system $\Pi(\mathbf{r}, \mathbf{r'}, t, t')$ with the KS response function $\Pi^{KS}(\mathbf{r}, \mathbf{r'}, t, t')$ [78]:

$$\int dt' d^3 r' \Pi(\mathbf{r}, \mathbf{r'}, t, t') \delta v_{\text{ext}}(\mathbf{r'}, t') = \int dt' d^3 r' \Pi^{KS}(\mathbf{r}, \mathbf{r'}, t, t') \; x$$
$$x \left[\delta v_{\text{ext}}(\mathbf{r'}, t') + \delta v_H[n](\mathbf{r'}, t') + \delta v_{xc}[n](\mathbf{r'}, t') \right]. \tag{2.42}$$

In order to write explicitly Π and Π^{KS} relation, it is necessary to expand the exchange correlation and include a kernel f_{xc} [78]:

$$v_{xc}[n_{GS} + \delta n](\mathbf{r}, t) = v_{xc}[n_{GS}](\mathbf{r}) + \int dt' d^3 r' f_{xc}[n_{GS}](\mathbf{r}, \mathbf{r'}, t, t') \delta n(\mathbf{r'}, t'), \tag{2.43}$$

$$f_{xc}[n_{GS}(\mathbf{r}, \mathbf{r'}, t, t')] = \frac{\delta v_{xc}[n](\mathbf{r}, t)}{\delta n(\mathbf{r'}, t')}|_{n=n_{GS}}. \tag{2.44}$$

Now it is possible to apply the chain rule for δv_H and δv_{xc},

$$\begin{aligned} \delta v_H[n](\mathbf{r'}, t') &= \int dt_1 dt_1 d^3 r_1 d^3 r_2 \frac{\delta v_H(\mathbf{r'}, t')}{\delta n(\mathbf{r}_1, t_1)} \frac{\delta n(\mathbf{r}_1, t_1)}{\delta v_{\text{ext}}(\mathbf{r}_2, t_2)}, \\ &= \int dt_1 dt_1 d^3 r_1 d^3 r_2 \frac{1}{|\mathbf{r}_1 - \mathbf{r'}|} \Pi(\mathbf{r}_1, \mathbf{r}_2, t_1, t_2) \delta v_{\text{ext}}(\mathbf{r}_2, t_2). \end{aligned} \tag{2.45}$$

$$\begin{aligned} \delta v_{xc}[n](\mathbf{r'}, t') &= \int dt_1 dt_1 d^3 r_1 d^3 r_2 \frac{\delta v_{xc}(\mathbf{r'}, t')}{\delta n(\mathbf{r}_1, t_1)} \frac{\delta n(\mathbf{r}_1, t_1)}{\delta v_{\text{ext}}(\mathbf{r}_2, t_2)} \delta v_{\text{ext}}(\mathbf{r}_2, t_2), \\ &= \int dt_1 dt_1 d^3 r_1 d^3 r_2 f_{xc}(\mathbf{r'}, \mathbf{r}_1, t', t_1) \Pi(\mathbf{r}_1, \mathbf{r}_2, t_1, t_2) \delta v_{\text{ext}}(\mathbf{r}_2, t_2). \end{aligned} \tag{2.46}$$

By changing the variables of integration and going to the frequency domain [78]:

$$\Pi(\mathbf{r}, \mathbf{r'}, \omega) = \Pi^{KS}(\mathbf{r}, \mathbf{r'}, \omega) + \int d^3 r_1 d^3 r_2 \Pi^{KS}(\mathbf{r}, \mathbf{r}_1, \omega) \left(\frac{1}{|\mathbf{r}_1 - \mathbf{r}_2|} + f_{xc}(\mathbf{r}, \mathbf{r'}, \omega) \right) \Pi(\mathbf{r}_2, \mathbf{r'}, \omega). \tag{2.47}$$

Relation (2.47) corresponds to the Hedin equation for the polarization (this will be treated deeply in the GW section) [79]. For the evaluation of the response function of an interacting electron system, the Kohn-Sham system should be calculated and aftyerwards the interacting response function is estimated by applying (2.47) with some approximated exchange-correlation kernel [78]. From here, we can extract the approximations for independent particle approximation (IPA) in which both contributions (Hartree and Kernel) are omitted [78], *i.e.*,

$$\Pi(\mathbf{r},\mathbf{r'},\omega) = \Pi^{KS}(\mathbf{r},\mathbf{r'},\omega). \tag{2.48}$$

The same can be said about the random phase approximation (RPA) or Hartree approximation in which only the exchange-correlation kernel is set to zero, *i.e.*,

$$\Pi(\mathbf{r},\mathbf{r'},\omega) = \Pi^{KS}(\mathbf{r},\mathbf{r'},\omega) + \int d^3r_1 d^3r_2 \Pi^{KS}(\mathbf{r},\mathbf{r}_1,\omega)\frac{1}{|\mathbf{r}_1-\mathbf{r}_2|}\Pi(\mathbf{r}_2,\mathbf{r'},\omega). \tag{2.49}$$

An explicit formula for the response function can be obtained by following the derivation of ref [80]. In summary, the authors perturb the system of a Hamiltonian $\hat{H}^0$ with an small perturbation $\delta\hat{H}(t)$ of the form:

$$\delta\hat{H}(t) = e^{\eta t}\sum_{i=1}^{N}\delta v(\mathbf{r}_i,t), \quad 0<\eta<<1, \tag{2.50}$$

where the factor $e^{\eta t}$ is introduced to guarantee an adiabatic, slow switching from the unperturbed Hamiltonian from $t\to-\infty$ ($e^{\eta t}=0$) to $t=0$ ($e^{\eta t}=1$) [78, 80]. The unperturbed system obeys the stationary Schrodinger equation:

$$\hat{H}^0\left|\Psi_i^0\right\rangle = E_i\left|\Psi_i^0\right\rangle, \tag{2.51}$$

where i denotes the ground ($i=0$) and excited states ($i>0$). This way $\left|\Psi_0^0\right\rangle$ and E_0^0 are the ground state wavefunction and energy. The time evolution of the ground state is given by:

$$\left|\Psi^0(t)\right\rangle = e^{-iE_0t}\left|\Psi_0^0\right\rangle. \tag{2.52}$$

On the other hand, the time dependent Schrodinger equation reads

$$i\frac{\partial|\Psi(t)\rangle}{\partial t} = \left(\hat{H}^0+\delta\hat{H}(t)\right)|\Psi(t)\rangle, \tag{2.53}$$

and according to first-order perturbation theory, $|\Psi(t)\rangle$ can be expressed as

$$|\Psi(t)\rangle = \left|\Psi^0(t)\right\rangle + \sum_{i\neq0}a_i(t)e^{-iE_it}\left|\Psi_i^0\right\rangle. \tag{2.54}$$

In other words, the perturbed wavefunctions are functions of the unperturbed time-dependent ground state solution ($\left|\Psi^0)(t)\right\rangle$) plus a mixture of components resulting from excited states of the unperturbed Hamiltonian [78]. The time dependent coefficients $a_i(t)$ can be expresed in frequency domain as

$$\begin{aligned}
a_i(t) &= -i\int_{-\infty}^{t} dt' e^{i\omega_{0i}t'}\left\langle\Psi_j^0\right|\delta\hat{H}(t')\left|\Psi_0^0\right\rangle,\\
a_i(t) &= -\int d^3r'\int\frac{\omega}{2\pi}\int_{-\infty}^{t} dt' e^{i(\omega_{0i}-\omega)t'}\delta v(\mathbf{r}',\omega)\left\langle\Psi_i^0\right|\hat{n}(\mathbf{r}')\left|\Psi_0^0\right\rangle,\\
a_i(t) &= -\int d^3r'\int\frac{\omega}{2\pi}\delta v(\mathbf{r}',\omega)\left\langle\Psi_i^0\right|\hat{n}(\mathbf{r}')\left|\Psi_0^0\right\rangle\frac{e^{i(\omega_{0i}-\omega)t'}}{\omega_{0i}-\omega},
\end{aligned} \tag{2.55}$$

where ω_{0i} denotes the difference between the energy of an excited state and the ground state $\omega_{0i} = E_i - E_0$ [78]. The change in the density resulting from the perturbation is

$$n_{\text{ind}}(\mathbf{r},t) = \delta n(\mathbf{r},t) = \langle\Psi(t)|\hat{n}(\mathbf{r})|\Psi(t)\rangle - \left\langle\Psi^0(t)\right|\hat{n}(\mathbf{r})\left|\Psi^0(t)\right\rangle. \tag{2.56}$$

Substituting (2.55) into (2.56), and by neglecting the terms proportional to the square of $|\Psi(t)\rangle - \left|\Psi^0(t)\right\rangle$, the induced density becomes:

$$\begin{aligned}
n_{\text{ind}}(\mathbf{r},t) &= \sum_{i\neq 0}\left[a_i(t)\left\langle\Psi_0^0\right|\hat{n}(\mathbf{r})\left|\Psi_i^0\right\rangle e^{-i\omega_{0i}t} + a_i^*(t)\left\langle\Psi_i^0\right|\hat{n}(\mathbf{r})\left|\Psi_0^0\right\rangle e^{-i\omega_{0i}t}\right],\\
n_{\text{ind}}(\mathbf{r},t) &= -\int d^3r'\int\frac{d\omega}{2\pi}\delta v(\mathbf{r'},\omega)e^{-i\omega t}\,\mathrm{x}\\
&\quad\sum_{i\neq 0}\left(\frac{\left\langle\Psi_i^0\right|\hat{n}(\mathbf{r'})\left|\Psi_0^0\right\rangle\left\langle\Psi_0^0\right|\hat{n}(\mathbf{r})\left|\Psi_i^0\right\rangle}{\omega_{0i}-\omega} + \frac{\left\langle\Psi_0^0\right|\hat{n}(\mathbf{r'})\left|\Psi_i^0\right\rangle\left\langle\Psi_0^i\right|\hat{n}(\mathbf{r})\left|\Psi_0^0\right\rangle}{\omega_{0i}+\omega}\right).
\end{aligned} \tag{2.57}$$

And, in the frequency space:

$$n_{\text{ind}}(\mathbf{r},\omega) = -\int d^3r'\delta v(\mathbf{r'},\omega)\sum_{i\neq 0}\left(\frac{\left\langle\Psi_i^0\right|\hat{n}(\mathbf{r'})\left|\Psi_0^0\right\rangle\left\langle\Psi_0^0\right|\hat{n}(\mathbf{r})\left|\Psi_i^0\right\rangle}{\omega_{0i}-\omega} + \frac{\left\langle\Psi_0^0\right|\hat{n}(\mathbf{r'})\left|\Psi_i^0\right\rangle\left\langle\Psi_0^i\right|\hat{n}(\mathbf{r})\left|\Psi_0^0\right\rangle}{\omega_{0i}+\omega}\right). \tag{2.58}$$

From the definition of the response function in (2.38):

$$\Pi(\mathbf{r},\mathbf{r}',\omega) = \frac{\delta n(\mathbf{r},\omega)}{\delta v(\mathbf{r}',\omega)} = -\sum_{i\neq 0}\left(\frac{\left\langle\Psi_i^0\right|\hat{n}(\mathbf{r}')\left|\Psi_0^0\right\rangle\left\langle\Psi_0^0\right|\hat{n}(\mathbf{r})\left|\Psi_i^0\right\rangle}{\omega_{0i}-\omega} + \frac{\left\langle\Psi_0^0\right|\hat{n}(\mathbf{r}')\left|\Psi_i^0\right\rangle\left\langle\Psi_0^i\right|\hat{n}(\mathbf{r})\left|\Psi_0^0\right\rangle}{\omega_{0i}+\omega}\right). \tag{2.59}$$

The Kohn-Sham scheme comes naturally from this formula. Since the KS wavefunctions correspond to non-interacting electrons, the full $\left|\Psi_0^0\right\rangle$ can be expressed as a Slater determinant as well as $\left|\Psi_i^0\right\rangle$. So, the response function for the Kohn-Sham system is [78, 80]:

$$\Pi^{KS}(\mathbf{r},\mathbf{r'},\omega) = -\sum_n\sum_m 2\left(\frac{\psi_m^*(\mathbf{r'})\psi_n^*(\mathbf{r'})\psi_n^*(\mathbf{r})\psi_m(\mathbf{r})}{\epsilon_m-\epsilon_n-\omega} + \frac{\psi_n^*(\mathbf{r'})\psi_m^*(\mathbf{r'})\psi_m^*(\mathbf{r})\psi_n^*(\mathbf{r})}{\epsilon_m-\epsilon_n+\omega}\right), \tag{2.60}$$

where n counts the occupied states, m for the unoccupied ones, and the difference $\omega_{mn} = \epsilon_m - \epsilon_n$ corresponds to the transition energy (electron jumps). Interestingly, equations (2.59) and (2.60) correspond to the Green's function. Relation (2.60) takes the following form when the system is a crystal [78]:

$$\Pi^{KS}_{\mathbf{G},\mathbf{G}'}(\mathbf{q},\omega) = -\frac{1}{V}\sum_{n,m,\mathbf{k}} 2 f_{n\mathbf{k}} \left\langle u_{m\mathbf{k}+\mathbf{q}} \right| e^{i\mathbf{G}.\mathbf{r}} \left| u_{n\mathbf{k}} \right\rangle \left\langle u_{n\mathbf{k}} \right| e^{i\mathbf{G}'.\mathbf{r}'} \left| u_{m\mathbf{k}+\mathbf{q}} \right\rangle \text{ x} \\ \left(\frac{1}{\epsilon_{m\mathbf{k}+\mathbf{q}} - \epsilon_{n\mathbf{k}} - \omega - i\eta} + \frac{1}{\epsilon_{m\mathbf{k}+\mathbf{q}} - \epsilon_{n\mathbf{k}} + \omega + i\eta} \right), \tag{2.61}$$

where $\mathbf{q}$ and $\mathbf{q}'$ are the fourier transform with respect to $\mathbf{r}$ and $\mathbf{r'}$, and $\mathbf{G}$ and $\mathbf{G'}$ correspond to the invariance that $\mathbf{R}$ (ion positions in r-space) represent in the reciprocal lattice space [78]. Consequently one can replace $\mathbf{q} \rightarrow \mathbf{q}+\mathbf{G}$ and $\mathbf{q'} \rightarrow \mathbf{q'}+\mathbf{G'}$ where $\mathbf{q}$ lies within the first Brillouin Zone (IBZ) [78]. The shift of $n \rightarrow n\mathbf{k}$ and $m \rightarrow m\mathbf{k}$ means the sum runs over bands and k points. Lastly, the KS wave function is expressed in terms of the Bloch wave functions according to:

$$\psi_{n\mathbf{k}}(\mathbf{r}) = e^{i\mathbf{k}.\mathbf{r}} u_{n\mathbf{k}}(\mathbf{r}). \tag{2.62}$$

2.2.3 Macroscopic and microscopic dielectric constant

The dielectric function encloses the optical spectra within its imaginary component. For this reason, a fundamental description of its behavior is necessary. There are two *types* of dielectric constant, the microscopic and macroscopic. The first relates the microscopic electric field (*i.e.*, inside a unitary cell) with the external field [78],

$$\mathbf{e}(\mathbf{r},\omega) = \int d^3 r' \varepsilon^{-1}(\mathbf{r},\mathbf{r'},\omega)\mathbf{E}_{\text{ext}}(\mathbf{r'},\omega), \tag{2.63}$$

meanwhile, the second is the link between the macroscopic electric field of the system and the external field [78], *i.e.*,

$$\mathbf{E}(\mathbf{r},\omega) = \int d^3 r' \varepsilon^{-1}_{\text{mac}}(\mathbf{r}-\mathbf{r'},\omega)\mathbf{E}_{\text{ext}}(\mathbf{r'},\omega). \tag{2.64}$$

The fourier transforms of (2.63) and (2.64) yield [78]:

$$\mathbf{E}(\mathbf{q},\omega) = \varepsilon^{-1}_{\text{mac}}(\mathbf{q},\omega)\mathbf{E}_{\text{ext}}(\mathbf{q},\omega), \tag{2.65}$$

$$\mathbf{e}(\mathbf{q}+\mathbf{G},\omega) = \sum_{\mathbf{G'}} \varepsilon^{-1}(\mathbf{q}+\mathbf{G},\mathbf{q}+\mathbf{G'},\omega)\mathbf{E}_{\text{ext}}(\mathbf{q}+\mathbf{G'},\omega), \tag{2.66}$$

where $\mathbf{q'} = \mathbf{q}+\mathbf{G}$, and $\mathbf{q}'' = \mathbf{q}+\mathbf{G'}$ represent the translation invariance in reciprocal space with $\mathbf{q}$ and $\mathbf{q'}$ belonging to the IBZ [78]. In order to establish a relation between both equations, a

correspondence from the macroscopic and microscopic electric field has to be done,

$$\mathbf{E}(\mathbf{r},\omega) = \frac{1}{V}\int_{V(\mathbf{R})} d^3 r \mathbf{e}(\mathbf{r},\omega), \tag{2.67}$$

where $V(\mathbf{R})$ is the integration over the unit cell around $\mathbf{R}$ [78]. The Fourier transform of (2.67) expresses the relation between both fields, *i.e.*,

$$\mathbf{E}(\mathbf{q}+\mathbf{G},\omega) = \mathbf{e}(\mathbf{q},\omega)\delta_{\mathbf{G},0}. \tag{2.68}$$

On the other hand, the macroscopic nature of the external field can be translated to reciprocal space as:

$$\mathbf{E}_{\text{ext}}(\mathbf{q}+\mathbf{G},\omega) = \mathbf{E}_{\text{ext}}(\mathbf{q},\omega)\delta_{\mathbf{G},0}. \tag{2.69}$$

Thus, the relation between the macroscopic electric field and the external one can be written in terms of the dielectric constant $\varepsilon^{-1}_{\mathbf{GG'}}(\mathbf{q},\omega) = \varepsilon^{-1}(\mathbf{q}+\mathbf{G},\mathbf{q}+\mathbf{G'},\omega)$,

$$\mathbf{E}(\mathbf{q},\omega) = \mathbf{e}(\mathbf{q},\omega) = \sum_{\mathbf{G'}} \varepsilon^{-1}_{0\mathbf{G'}}(\mathbf{q},\omega)\mathbf{E}_{\text{ext}}(\mathbf{q},\omega)\delta_{\mathbf{G'},0} = \varepsilon^{-1}_{00}(\mathbf{q},\omega)\mathbf{E}_{\text{ext}}(\mathbf{q},\omega). \tag{2.70}$$

By comparing (2.66) and (2.70), the relation between macroscopic and microscopic dielectric constant becomes clear:

$$\varepsilon^{-1}_{\text{mac}}(\mathbf{q},\omega) = \varepsilon^{-1}_{00}(\mathbf{q},\omega), \tag{2.71}$$

$$\varepsilon_{\text{mac}}(\mathbf{q},\omega) = (\varepsilon^{-1}_{00}(\mathbf{q},\omega))^{-1}. \tag{2.72}$$

Therefore, the macroscopic dielectric function is obtained by inverting the microscopic dielectric function with respect to $\mathbf{G},\mathbf{G'}$, taking the case ($\mathbf{G} = \mathbf{G}' = 0$) of the resulting matrix and inverting this 3x3 tensor [78]. Now, the only task remaining is to link the microscopic dielectric constant with the response function Π. This is achieved with the Poisson equation in the reciprocal space in where the electric field $\mathbf{E}(\mathbf{q})$ is written in terms of the density function $n(\mathbf{q})$. This way the electric field can be expressed in terms of the induced density [78]:

$$\varepsilon^{-1}_{\mathbf{G},\mathbf{G'}}(\mathbf{q},\omega) = \varepsilon^{-1}(\mathbf{q}+\mathbf{G},\mathbf{q}+\mathbf{G'},\omega) = \delta_{\mathbf{G},\mathbf{G'}} + \frac{4\pi}{|\mathbf{q}+\mathbf{G}||\mathbf{q}+\mathbf{G'}|}\frac{\partial n_{\text{ind}}(\mathbf{q}+\mathbf{G},\omega)}{\partial v_{\text{ext}}(\mathbf{q}+\mathbf{G'},\omega)}, \tag{2.73}$$

where the quantity

$$\frac{\partial n_{\text{ind}}(\mathbf{q}+\mathbf{G},\omega)}{\partial v_{\text{ext}}(\mathbf{q}+\mathbf{G'},\omega)} = \Pi_{\mathbf{G},\mathbf{G'}}(\mathbf{q},\omega), \tag{2.74}$$

is the response function found in section 2.2.2. The dielectric function is then written in terms of the response function

$$\varepsilon^{-1}_{\mathbf{G},\mathbf{G'}}(\mathbf{q},\omega) = \varepsilon^{-1}(\mathbf{q}+\mathbf{G},\mathbf{q}+\mathbf{G'},\omega) = \delta_{\mathbf{G},\mathbf{G'}} + \frac{4\pi}{|\mathbf{q}+\mathbf{G}||\mathbf{q}+\mathbf{G'}|}\Pi_{\mathbf{G},\mathbf{G'}}(\mathbf{q},\omega). \tag{2.75}$$

Consequently, computing the response function (which can be done by using Π^{KS}) of the system leads us to the microscopic dielectric function, which can be turned into the macroscopic dielectric function, using (2.72), to finally get the optical spectra.
One curious point, that will be explained later, is that the dielectric function can be expressed in terms of the derivative with respect to the total potential [78]:

$$\varepsilon_{\mathbf{G},\mathbf{G'}}(\mathbf{q},\omega) = \delta_{\mathbf{G},\mathbf{G'}} - \frac{4\pi}{|\mathbf{q}+\mathbf{G}||\mathbf{q}+\mathbf{G'}|}\frac{\partial n_{\text{ind}}(\mathbf{q}+\mathbf{G},\omega)}{\partial v_{\text{tot}}(\mathbf{q}+\mathbf{G'},\omega)}, \tag{2.76}$$

where

$$\frac{\partial n_{\text{ind}}(\mathbf{q}+\mathbf{G},\omega)}{\partial v_{tot}(\mathbf{q}+\mathbf{G'},\omega)} = \Pi^{*}_{\mathbf{G},\mathbf{G'}}(\mathbf{q},\omega), \tag{2.77}$$

is the irreducible polarizability (or screned polarization), whereas $\Pi_{\mathbf{G},\mathbf{G'}}(\mathbf{q},\omega)$ is called the reducible polarization in the framework of Hedin's equations [79]. Both polarizations are linked by one of the Hedin's equation [79] (similar as in the case with the Π^{KS}) as follows:

$$\Pi_{\mathbf{G},\mathbf{G'}}(\mathbf{q},\omega) = \Pi^{*}_{\mathbf{G},\mathbf{G'}}(\mathbf{q},\omega) + \sum_{\mathbf{G}_1\mathbf{G}_2}\Pi^{*}_{\mathbf{G},\mathbf{G}_1}(\mathbf{q},\omega)\frac{4\pi}{|\mathbf{q}+\mathbf{G}_1||\mathbf{q}+\mathbf{G}_2|}\Pi_{\mathbf{G}_2,\mathbf{G'}}(\mathbf{q},\omega). \tag{2.78}$$

2.3 Quasiparticle Many Body Perturbation Theory (QPMBPT)

With a framework for the calculation of the dielectric constant we will reframe it in terms of Green's functions.

2.3.1 0th order Green Function

Before going deeply in the formulation of Green's functions, lets begin with the basic definition for the non-interacting case. Every many body non-interacting system can be described by a Hamiltonian in terms of the kinetic energy and the external potential (*e.g.*, a periodic potential in a crystal) $\hat{H} = \hat{T} + \hat{U}_{\text{ext}}$. This Hamiltonian can be expressed in terms of the creation and annihilation operators, whose real space representation allows us to define the quantum field operator or second quantization operators [81, 82]

$$\begin{aligned}\hat{\Psi}(\mathbf{r}) &= \sum_k \hat{c}_k \psi_k(\mathbf{r}),\\ \hat{\Psi}^{\dagger}(\mathbf{r}) &= \sum_k \hat{c}^{\dagger}_k \psi_k(\mathbf{r}),\end{aligned} \tag{2.79}$$

where $\psi_k(\mathbf{r})$ represent single particle wavefunctions in real space, *e.g.*, for a crystal they will be the Bloch wave functions where the index k accounts for k points in the reciprocal lattice, and, another index could be added for the summation over bands. Consequently, the creation and annihilation operators $\hat{c}_k$, $\hat{c}^{\dagger}_k$ lie in the reciprocal space with the single particle wave functions (Bloch electrons) mapping them into real space [81]. In the following, the

Heisenberg picture is the natural way to define the Green's function in the non-interacting case. In this way the operators in (2.79) take a time dependence [82, 83]

$$\begin{aligned}\hat{c}_k(t) &= e^{i\hat{H}t}\hat{c}_k e^{-i\hat{H}t},\\ \hat{\Psi} &= e^{i\hat{H}t}\hat{\Psi}(\mathbf{r})e^{-i\hat{H}t}.\end{aligned} \tag{2.80}$$

Furthermore, we define a time-ordering $\hat{T}$ operator whose purpose is to order the product of time dependent operators in a way that early times are to the right and later times to the left [83], *i.e.*,

$$\hat{T}\hat{\Psi}(\mathbf{r}_1,t_1)\hat{\Psi}^\dagger(\mathbf{r}_2,t_2) = \begin{cases}\hat{\Psi}(\mathbf{r}_1,t_1)\hat{\Psi}^\dagger(\mathbf{r}_2,t_2), & t_1 > t_2\\ -\hat{\Psi}^\dagger(\mathbf{r}_2,t_2)\hat{\Psi}(\mathbf{r}_1,t_1), & t_2 > t_1\end{cases}, \tag{2.81}$$

where the minus sign comes for the definition of the anticommutator relation that fermions obey. The single particle 0^{th} order Green's function is defined in terms of the field operators acting on the ground state of the entire system $|\Psi_0\rangle$, so

$$G_0(\mathbf{r}_1,t_1,\mathbf{r}_2,t_2) = -i\,\langle\Psi_0|\,\hat{T}\hat{\Psi}(\mathbf{r}_1,t_1)\hat{\Psi}^\dagger(\mathbf{r}_2,t_2)\,|\Psi_0\rangle\,. \tag{2.82}$$

There exists, of course, a formulation for Green's function with annihilation and creation operators $\hat{c}_\nu$, $\hat{c}_\nu^\dagger$ in the reciprocal space [83]

$$G_0(\mathbf{k},\mathbf{k}',t,t') = -i\,\langle\Psi_0|\,\hat{T}\hat{c}_k(t)\hat{c}_k^\dagger(t')\,|\Psi_0\rangle\,. \tag{2.83}$$

The issue with reciprocal space is that it does not allow us to define clearly the density operator (real space), which is an useful quantity to make the analogy with DFT and TDDFT. From now on, the real space formulation will be our preferable choice. The meaning of 0^{th} order Green's function is to measure the transition of the system when a fermion jumps from one state to another without interacting with another particle in the middle of the process. For this reason, Green's functions, in general, receive the name of propagator [82].

When many particles are treated it is comfortable to work in Fock space instead of Hilbert space; the difference between them is related with field operators, as they rise and lower the number of particles, they built different states with different particle numbers (*e.g.*, $\left|\Psi^0\right\rangle = |0\rangle$ is the vacuum, $\left|\Psi^{(1)}\right\rangle$ is state with 1 particle, $\left|\Psi^{(2)}\right\rangle$ with two, and so on), those states correspond to different Hilbert spaces $\mathscr{H}_N$ [81, 83]. And, the collection of them gives birth to Fock space $\mathscr{F}$, thus, operators $\Psi(\mathbf{r}_1,t_1)$, $\Psi^\dagger(\mathbf{r}_2,t_2)$ map between different states in the Fock space [81]. The completeness relation in Fock space is:

$$\mathbf{1} = |0\rangle\langle 0| + \sum_n \left|\Psi_n^{(1)}\right\rangle\left\langle\Psi_n^{(1)}\right| + \sum_n \left|\Psi_n^{(2)}\right\rangle\left\langle\Psi_n^{(2)}\right| + \ldots, \tag{2.84}$$

in which the upper indices account for number of particles, and n for the different eigen-

states for given number of particles.
The spectral representation of the Green's function is important for extracting the absorption spectra of the system. This can be achieved by rewriting the Green's function as [82, 83]:

$$\begin{aligned} G_0(\mathbf{r},t) = -i\Big[&\theta(t)\sum_n \langle\Psi_0|\hat{\Psi}(\mathbf{r},t)|\Psi_n^{(N+1)}\rangle\langle\Psi_n^{(N+1)}|\hat{\Psi}^\dagger(\mathbf{r})|\Psi_0\rangle \\ &-\theta(-t)\sum_n \langle\Psi_0|\hat{\Psi}^\dagger(\mathbf{r})|\Psi_n^{(N-1)}\rangle\langle\Psi_n^{(N-1)}|\hat{\Psi}(\mathbf{r},t)|\Psi_0\rangle\Big], \end{aligned} \tag{2.85}$$

where $|\Psi_0\rangle$ is the ground state of the system. By introducing the explicit time dependence of the operators, we arrive at:

$$\begin{aligned} G_0(\mathbf{r},\omega) = &-i\sum_n \int_0^\infty dt e^{i[\omega+i\eta E_0^{(N)}-E_n^{(N+1)}]t}|\langle\Psi_n^{(N+1)}|\hat{\Psi}^\dagger(\mathbf{r})|\Psi_0\rangle|^2 \\ &+i\sum_n \int_{-\infty}^0 dt e^{i[\omega-i\eta E_n^{(N-1)}-E_0^{(N)}]t}|\langle\Psi_n^{(N-1)}|\hat{\Psi}(\mathbf{r})|\Psi_0\rangle|^2, \end{aligned} \tag{2.86}$$

where the factor $e^{-\eta t}$ ($\eta > 0$) is introduced in the Fourier transform because the Green's function is ill-defined due to the presence of an oscillatory behavior for $t \to \infty$ [83]. After integration of (2.86),

$$G_0(\mathbf{r},\omega) = \sum_n \left(\frac{\left\langle\Psi_n^{(N+1)}\middle|\hat{\Psi}^\dagger(\mathbf{r})\middle|\Psi_0\right\rangle|^2}{\omega + E_0^{(N)} - E_n^{(N+1)} + i\eta} + \frac{|\left\langle\Psi_n^{(N-1)}\middle|\hat{\Psi}(\mathbf{r})\middle|\Psi_0\right\rangle|^2}{\omega + E_n^{(N-1)} - E_0^{(N)} - i\eta} \right). \tag{2.87}$$

The rising operator $\Psi^\dagger(\mathbf{r})$ increases the energy by

$$E_n^{(N+1)} - E_0^{(N)} = \varepsilon_n^{(N+1)} + \mu_N, \tag{2.88}$$

where $\varepsilon_n^{(N+1)} = E_n^{(N+1)} - E_0^{(N+1)}$ is the excitation energy for the state with N+1 particles, and $\mu_N = E_0^{(N+1)} - E_0^{(N)}$ is the chemical potential [82, 83]. In the same way, the lowering operator $\Psi(\mathbf{r})$ in the second term reduces the energy by

$$E_0^{(N)} - E_n^{(N-1)} = \mu_{N-1} - \varepsilon_n^{(N-1)}, \tag{2.89}$$

if we assume that the difference between chemical potentials for μ_N and μ_{N+1} can be neglected. Furthermore, if the spectral densities are defined:

$$\begin{aligned} A(\mathbf{r},\omega) &= \sum_n \langle\Psi_n^{(N+1)}|\hat{\Psi}^\dagger(\mathbf{r})|\Psi_0\rangle|^2\delta(\omega-\varepsilon_n), \\ B(\mathbf{r},\omega) &= \sum_n |\langle\Psi_n^{(N-1)}|\hat{\Psi}(\mathbf{r})|\Psi_0\rangle|^2\delta(\omega-\varepsilon_n), \end{aligned} \tag{2.90}$$

the Green function can be written in terms of them:

$$G_0(\mathbf{r},\omega) = \int_0 d\omega' \left(\frac{A(\mathbf{r},\omega')}{\omega - \omega' - \mu + i\eta} + \frac{B(\mathbf{r},\omega')}{\omega + \omega' - \mu - i\eta} \right). \tag{2.91}$$

Equations (2.87) and (2.91) define the spectral representation of the Green's function and its poles account for the energies required to add/remove an electron from the system. The 0^{th} order Green's function is a solution of a differential equation in the frequency domain [64]:

$$G_0^{-1}(\mathbf{r},\mathbf{r}',\omega) = \delta(\mathbf{r}-\mathbf{r}')[\omega - h], \tag{2.92}$$

which in real space reads

$$\left[\frac{i\partial}{\partial t} - h \right] G_0(\mathbf{r},\mathbf{r}',t) = \delta(\mathbf{r},\mathbf{r}'), \tag{2.93}$$

where the Hamiltonian and h are related by

$$\hat{H} = \int d^3 r \hat{\Psi}^\dagger(\mathbf{r}) h \hat{\Psi}(\mathbf{r}). \tag{2.94}$$

Therefore, the spectral function (imaginary part of the Green's function) of the non-interacting system will be obtained by δ-like functions at the electron energies ε_n [64].

2.3.2 Green's functions

In order to use the full power of Green's function a generalization is needed from the non-interacting picture to a full interacting. An interacting system of many body fermions has a Hamiltonian of the form

$$\hat{H} = \hat{H}_0 + \hat{V}_H + \hat{V}_{\text{ext}}(t), \tag{2.95}$$

where $\hat{H}_0$ is the many body Hamiltonian without interactions, $\hat{V}_H$ accounts for e-e interactions and $\hat{V}_{\text{ext}}(t)$ is a perturbation defined in order to turn on electron jumps between states [79]. This last quantity is also presented in the 0^{th} order Green's treatment, but, since no interactions will happen between the internal "path" of the electron from one state to another, it has no reason to be formally defined. However, as we will see through the following sections, when interactions are turned on, the transition of an electron between states carries a myriad of interactions with its surroundings [82].

In order to achieve Green's function formulation including interactions, it is necessary to introduce the interaction picture (also called Dirac representation) [82, 84]. In this picture, the rising and lowering field operators in the Heisenberg representation $\hat{\Psi}(\mathbf{r},t)$ are linked with its counterparts in the Dirac one $\hat{\Psi}_d(\mathbf{r},t)$ via the scattering matrix $S(t,t')$,

$$\hat{\Psi}(\mathbf{r},t) = S(0,t)\hat{\Psi}_d(\mathbf{r},t)S(t,0), \tag{2.96}$$

where the scattering operator is defined in terms of the time evolution operators $U(t)$,

$$\begin{aligned} S(t,t') &= U(t)U(t') = \hat{T}e^{-i\int_t^{t'} dt[\hat{V}_{\text{ext}}+\hat{V}_H]}, \\ U(t) &= \hat{T}e^{-i\int_0^t dt'[\hat{V}_{\text{ext}}(t')+\hat{V}_H]} = e^{i\hat{H}_0 t}e^{-i\hat{H}t}, \end{aligned} \tag{2.97}$$

and is related to the evolution of the system between two different times due to the interactions $\hat{V}_H$ and $\hat{V}_{\text{ext}}(t)$. Using equation (2.96) and definitions (2.97) it is possible to find the expression for $\hat{\Psi}_0(\mathbf{r},t)$ in terms of the time independent (non-interacting) field operator $\hat{\Psi}(\mathbf{r})$ [82, 84]:

$$\hat{\Psi}_0(\mathbf{r},t) = e^{i\hat{H}_0 t}\hat{\Psi}(\mathbf{r})e^{-i\hat{H}_0 t}. \tag{2.98}$$

The next step is to built the definition of Green's function for the interaction picture. We can do this by using our Green's function definition for the 0^{th} order, and assume for a moment that it is valid for any Hamiltonian [82, 84]:

$$G(\mathbf{r},\mathbf{r'},t,t') = -i\langle\Psi_0|\hat{T}\hat{\Psi}(\mathbf{r},t)\hat{\Psi}^\dagger(\mathbf{r}',t')|\Psi_0\rangle, \tag{2.99}$$

where

$$\hat{\Psi}(\mathbf{r},t) = e^{iHt}\hat{\Psi}e^{-iHt}, \tag{2.100}$$

corresponds to the field operator in the Heisenberg picture.
However, there is a problem with state $|\Psi_0\rangle$; we do not know if, for $t=0$, it would be the true ground state of the non-interacting many body system [82]. To overcome this, the ground state of the non-interacting system is chosen to be at $t\to-\infty$, and is brought adiabatically with using the operator $S(-\infty,0)$. For this reason, equation (2.99) is well defined,

$$G(\mathbf{r},\mathbf{r'},t,t') = -i\langle\Psi_0|\hat{T}S(-\infty,0)\hat{\Psi}(\mathbf{r},t)\hat{\Psi}^\dagger(\mathbf{r}',t')S(0,-\infty)|\Psi_0\rangle. \tag{2.101}$$

After expanding this term with the time ordering operator, and using the definition of the field operator in the Dirac representation (2.96), the left handed bracket is replaced by

$$\langle\Psi_0|S(-\infty,0) = \frac{\langle\Psi_0|S(\infty,0)}{\langle\Psi_0|S(\infty,-\infty)|\Psi_0\rangle}. \tag{2.102}$$

So the Green's function reads,

$$G(\mathbf{r},\mathbf{r'},t,t') = -i\frac{\langle\Psi_0|\hat{T}\hat{\Psi}_0(\mathbf{r},t)\hat{\Psi}_0^\dagger(\mathbf{r}',t')S(\infty,-\infty)|\Psi_0\rangle}{\langle\Psi_0|S(\infty,-\infty)|\Psi_0\rangle}, \tag{2.103}$$

and the time ordering operator $\hat{T}$ sorts the matrix $S(\infty,-\infty)$ in three time intervals namely $S(\infty,t)$, $S(t,t')$ and $S(t',-\infty)$ [82]. The Green's function can be expressed in the spectral

representation (analogous to eq. (2.91)) [85, 86]:

$$G(\mathbf{r},\omega) = \int_0 d\omega' \left(\frac{A(\mathbf{r},\omega')}{\omega - \omega' - \Sigma^*(\mathbf{r},\omega) - \mu + i\eta} + \frac{B(\mathbf{r},\omega')}{\omega + \omega' - \Sigma^*(\mathbf{r},\omega) - \mu - i\eta} \right), \tag{2.104}$$

and obey,

$$\left[\frac{i\partial}{\partial t} - h_0 \right] G(\mathbf{r},\mathbf{r}',t,t') - \int d^3 r_1 d\, t_1 M(\mathbf{r},t,\mathbf{r}_1,t_1) G(\mathbf{r}_1,t_1,\mathbf{r}',t') = \delta(\mathbf{r},\mathbf{r}')\delta(t,t'), \tag{2.105}$$

for a Hamiltonian of the form [85]

$$\hat{H} = \int d^3 r \hat{\Psi}^\dagger(\mathbf{r},t) h_0 \hat{\Psi}(\mathbf{r},t) + \frac{1}{2} \int d^3 r d^3 r' \hat{\Psi}^\dagger(\mathbf{r},t) \hat{\Psi}^\dagger(\mathbf{r}',t) [v_H + \varphi] \hat{\Psi}(\mathbf{r}',t) \hat{\Psi}(\mathbf{r},t). \tag{2.106}$$

The new term $\Sigma^*(\mathbf{r},\omega)$ is the reduced self energy and $M(\mathbf{r},t,\mathbf{r}_1,t_1)$ is the interaction energy which will be explained later.
For the Hamiltonian, we have v_H and φ, which account for the Hartree potential and the perturbation respectively in terms of the density operator $\hat{n}$ and average density $n(\mathbf{r})$ [79]:

$$\begin{aligned} \hat{V}_{\text{ext}} &= \int d^3 r \varphi(\mathbf{r},t) \hat{n}(\mathbf{r}), \\ \hat{V}_H &= \int d^3 r' v_H(\mathbf{r}',\mathbf{r}) \hat{n}(\mathbf{r}'). \end{aligned} \tag{2.107}$$

Consequently, equations (2.107) give rise to a functional formulation in terms of the density operator, which will be exploited in deducting Hedin's equations.

2.3.3 Hedin's equations

Let's first define first a simple notation for the following, $1 = \mathbf{r}_1, t_1$, $d1 = d^3 r_1 d\, t_1$, and the ground state of non interacting system is $|\Psi_0\rangle = |N\rangle$, the propagator reads:

$$iG(1,2) = \frac{\langle N | \hat{T} S \hat{\Psi}(1) \hat{\Psi}^\dagger(2) | N \rangle}{\langle N | S | N \rangle}, \tag{2.108}$$

where the known scattering matrix S depends on the external potential $\hat{V}_{\text{ext}}$ and the Hartree interaction $\hat{V}_H$. What is more, these two depend on the potentials v_H and φ defined in (2.107). Even though the field φ seems physical it shall be turned off from every equation after the deduction has been completed. As in the case with DFT, a similar dependence of functionals will be followed. For the density operator, the formulation used for this picture is in terms of the rising and lowering field operators, consequently, the density treated in DFT becomes an operator defined in terms of those creation/annihilation operators [79]:

$$\hat{n}(1) = \hat{\Psi}^\dagger(1) \hat{\Psi}(1). \tag{2.109}$$

The average density $n(1)$ and the Hartree potential $v_H(1)$ are defined in terms of the Green's function [79]:

$$n(1) = -i\frac{\langle N|\,\hat{T}S\hat{n}(1)\,|N\rangle}{\langle N|\,S\,|N\rangle} = iG(1,1^{\dagger}), \tag{2.110}$$

$$v_H(1) = \int d2\frac{1}{|\mathbf{r}_1-\mathbf{r}_2|}n(2) = i\int d2G(2,2^{\dagger})\frac{1}{|\mathbf{r}_1-\mathbf{r}_2|}\delta(t_1-t_2). \tag{2.111}$$

Once we have settled the notation, we are ready to deduct Hedin's equations. The derivation chosen here follows the work by Molinari et. al, [79]. A diagrammatic picture will be followed parallel to equations in order to clarify things.

The first equation corresponds to the Dyson equation. The Green function $G(1,2)$ is the transition for a particle to go from state 1 to 2 and is usually represented by two lines diagrammatically. Another way to appreciate the propagation of the electron is by imagining a pure transition (without interactions), which corresponds to $G_0(1,2)$, plus all the quasiparticle interaction corrections that happens in the middle, *i.e.*,

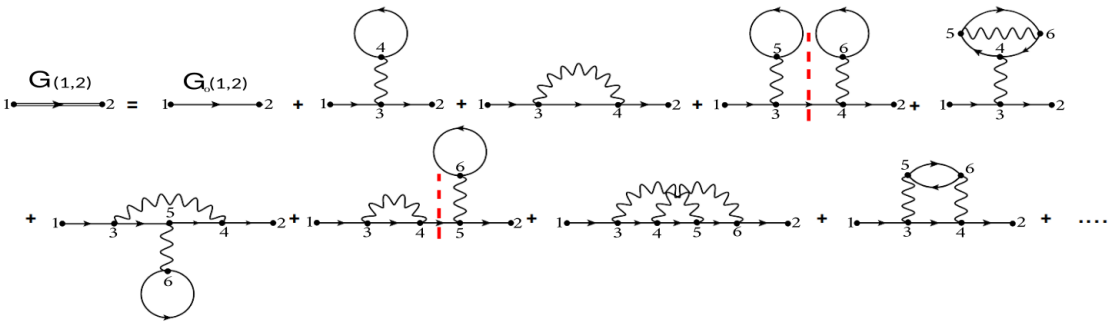

Where Hartree and Fock terms corresponds to the first two diagrams, and red lines account for separable diagrams. These interactions of the particle with its surroundings can be factorized into the term known as reducible self-energy Σ [86], leaving the Green's function as,

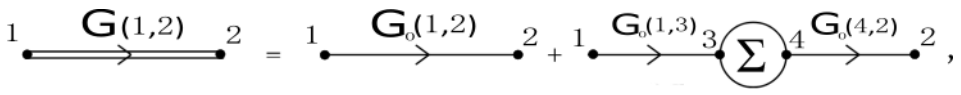

$$G(1,2) = G_0(1,2) + \int d3d4G_0(1,3)\Sigma(3,4)G_0(4,2), \tag{2.112}$$

where coordinates 3 and 4 show the intermediate points where quasiparticle interactions occur. Formally, the self-energy $\Sigma(3,4)$ is defined as the sum of all Feynman diagrams with no external lines such that they can be inserted in a propagator [86].

Additionally, it is possible to define a quantity called irreducible self energy Σ^* which accounts for all Feynman diagrams which have no external lines, *i.e.*, the ones that can be inserted in a propagator and cannot be separated in two pieces by cutting a single propagator [86]. Thus, it is possible to decompose the reducible self energy in terms of irreducible ones [86]:

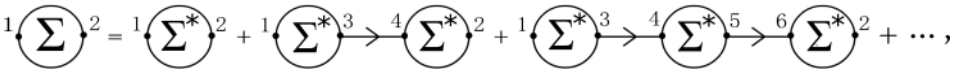

$$\Sigma(1,2) = \Sigma^*(1,2) + \int d3d4\Sigma^*(13)G_0(3,4)\Sigma^*(4,2) + \int d3d4d5d6\Sigma^*(13)G_0(3,4)\Sigma^*(4,5)G_0(5,6)\Sigma^*(6,2). \tag{2.113}$$

If (2.113) is replaced in (2.112) we arrive in the Dyson equation (diagrammatically it would correspond to expanding the reducible self energy in the Green's propagator and then just factorizing them by using the Green's definition itself):

$$G(1,2) = G_0(1,2) + \int d3d4G_0(1,3)\Sigma^*(3,4)G(4,2), \tag{2.114}$$

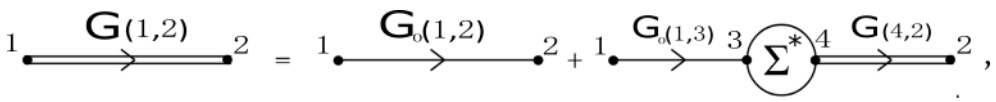

$$G^{-1}(1,2) = G_0^{-1}(1,2) - \Sigma^*(1,2). \tag{2.115}$$

The second equation for the screened (irreducible) Coulomb potential can be derived from the definition of the effective potential [79], *i.e.*, the sum of the time dependent perturbation and the Hartree term

$$V(1) = \varphi(1) + v_H(1) = \varphi(1) + i\int d2v(1,2)G(2,2^\dagger), \tag{2.116}$$

where $v(1,2) = 1/|\mathbf{r}_1 - \mathbf{r}_2|$. The functional derivate of $V(1)$ with respect to $\varphi(2)$ is

$$\frac{\delta V(1)}{\delta\varphi(2)} = \delta(1,2) + i\int d3v(1,3)\frac{\delta G(3,3^\dagger)}{\delta\varphi(2)}, \tag{2.117}$$

where the last term in the right hand side can be written in terms of the reducible polarization for the following property for any operator $\hat{A}$:

$$\frac{\delta}{\delta\varphi(1)}\frac{\langle N|\,\hat{T}S\hat{A}\,|N\rangle}{\langle N|\,S\,|N\rangle} = i\frac{\langle N|\,\hat{T}S\hat{A}\delta\hat{n}(1)\,|N\rangle}{\langle N|\,S\,|N\rangle}. \tag{2.118}$$

The term $\delta\hat{n}(1)$ measures the response of the system under the small perturbation, and is represented as the difference between the density operator and the average density of the system [79], *i.e.*

$$\delta\hat{n}(1) = \hat{n}(1) - n(1), \tag{2.119}$$

Considering $\hat{A} = \delta n(2)$, the definition for the reducible polarization appears:

$$\Pi(1,2) = i\frac{\langle N|\,\hat{T}S\delta\hat{n}(1)\delta\hat{n}(2)\,|N\rangle}{\langle N|\,S\,|N\rangle}. \tag{2.120}$$

In fact, we arrive at the same quantity when working with linear response theory, in which the polarization is the variation of the density with respect to the perturbation (eq. (2.39)). This is more clear, when (2.120) is expressed as:

$$\Pi(1,2) = i\frac{\delta G(1,1^{\dagger})}{\delta\varphi(2)}. \tag{2.121}$$

So, the reducible polarization measures the change of the average density when the perturbation undergoes a small change. The definition of $\Pi(1,2)$ can be replaced in (2.117):

$$\frac{\delta V(1)}{\delta\varphi(2)} = \delta(1,2) + \int d3v(1,3)\Pi(3,2). \tag{2.122}$$

On the other hand, the screened Coulomb potential is defined in terms of the Coulomb interaction:

$$W(1,2) = \int d3\frac{\delta V(1)}{\delta\varphi(3)}v(3,2), \tag{2.123}$$

and, can be expressed in terms of the reducible polarization by using (2.122):

$$W(1,2) = v(1,2) + \int d3d4v(1,3)\Pi(3,4)v(4,2). \tag{2.124}$$

Thus we find that the screened Coulomb interaction is represented by the unscreened Coulomb interaction plus Coulomb interactions connected via the unscreened (reducible) polarization. From equation (2.122) it is useful to derive its generalization [79]:

$$\frac{\delta}{\delta\varphi(1)} = \frac{\delta}{\delta V(1)} + \int d2d3v(2,3)\Pi(3,1)\frac{\delta}{\delta V(2)}, \tag{2.125}$$

and from that, the following identity:

$$\int d1v(4,1)\frac{\delta}{\delta\varphi(1)} = \int d1W(4,1)\frac{\delta}{\delta V(1)}. \tag{2.126}$$

If the chain rule is applied to the screened polarization,

$$\Pi(1,2) = i\frac{\delta G(1,1^{\dagger})}{\delta V(2)}\frac{\delta V(2)}{\delta\varphi(2)}, \tag{2.127}$$

and, by replacing (2.122), we obtain:

$$\Pi(1,2) = i\frac{\delta G(1,1^{\dagger})}{\delta V(2)} + i\int d3d4\frac{\delta G(1,1^{\dagger})}{\delta V(3)}v(3,4)\Pi(4,2), \tag{2.128}$$

where the term

$$\Pi^*(1,2) = i\frac{\delta G(1,1^\dagger)}{\delta V(2)}, \tag{2.129}$$

is the screened or irreducible polarization. Its meaning corresponds to the variation of the density when the effective potential $V(2)$ undergoes a small change. Equation (2.128) is the analogous of (2.78) and can be interpreted as follows, the system is perturbed with a small perturbation causing fermions to change states, the response of the system for this small change without considering the interactions (Hartree term) is reflected in the unscreened polarization. Meanwhile, when the Coulomb interaction is turned on, the response function of the system is screened due to the myriad of interactions of the electron with its surroundings. The term "reducible" and "irreducible" can be clarified by looking at the Feynmann diagram for (2.128) and expanding it, *i.e.*,

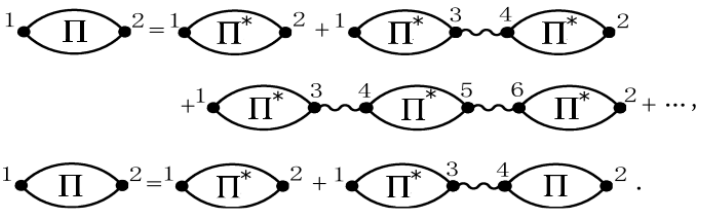

The reducible term $\Pi(1,2)$ can be expressed in terms of the irreducible one $\Pi^*(1,2)$. From the identity (2.126), it is possible to derive:

$$\int d4v(5,4)\Pi(4,2) = \int d4W(5,4)\Pi^*(4,2), \tag{2.130}$$

and the Coulomb screened potential (2.124) is written as:

$$W(1,2) = v(1,2) + \int d3d4v(1,3)\Pi^*(3,4)W(4,2). \tag{2.131}$$

This leads to our second Hedin's equation. This expresses that the screened Coulomb interaction expansion can be reduced in terms of the irreducible polarization Π^* as well as the irreducible Coulomb interaction $v(1,2)$,

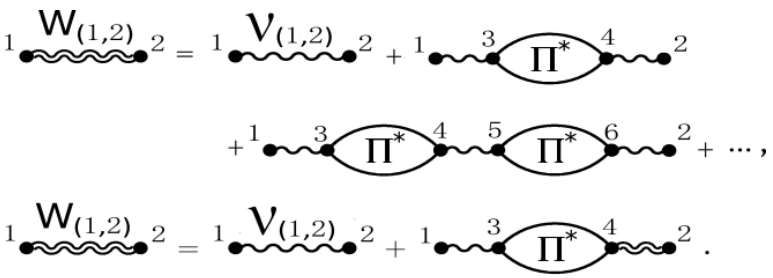

From the definition of $W(1,2)$, we can interpret this term as follows, the Coulomb interaction suffer a modification due to the change make by the perturbation reflected in the polarization, thus, making a variation in the intensity (screened) of the Coulomb interaction.

The third equation arrives from the definition of the vertex function [79]. The propagator has the identity:

$$\int d3G^{-1}(5,3)G(3,1) = \delta(5,1), \tag{2.132}$$

whose derivate with respect to the effective potential is

$$\int d3\frac{\delta G^{-1}(5,3)}{\delta V(4)}G(3,2) + \int d3G^{-1}(5,3)\frac{\delta G(3,2)}{\delta V(4)} = 0. \tag{2.133}$$

If both sides are multiplied by $\int d5G(1,5)$:

$$\int d3d5G(1,5)\frac{\delta G^{-1}(5,3)}{\delta V(4)}G(3,2) + \frac{\delta G(1,2)}{\delta V(4)} = 0. \tag{2.134}$$

and, by choosing $2 = 1^{\dagger}$, the definition of $\Pi^*(1,4)$ is obtained from the second term on the left side, *i.e.*,

$$\Pi^*(1,4) = i\int d3d5G(1,5)\frac{\delta G^{-1}(5,3)}{\delta V(4)}G(3,1^{\dagger}). \tag{2.135}$$

If the definition of the vertex function is taken into account,

$$\Gamma(1;2,3) = -\frac{\delta G^{-1}(2,3)}{\delta V(1)}, \tag{2.136}$$

we arrive on the third Hedin's equation for the screened polarization:

$$\Pi^*(1,2) = -i\int d3d4\Gamma(2;3,4)G(1,3)G(4,1), \tag{2.137}$$

whose diagrammatic form can be interpreted as

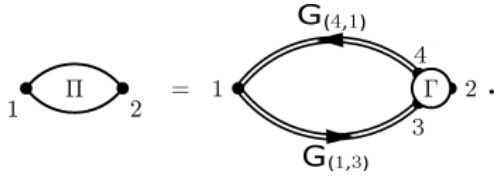

The fourth equation is the vertex function but expressed in terms of the irreducible self-energy, this is achieved by using Dyson equation [79]:

$$\begin{aligned}\Gamma(1;2,3) =& \frac{\delta G^{-1}(2,3)}{\delta V(1)},\\ =& \frac{\delta G_0^{-1}(2,3)}{\delta V(1)} - \frac{\delta \Sigma^*(1,2)}{\delta V(1)},\\ =& \delta(1,2)\delta(1,3) + \frac{\delta \Sigma^*(2,3)}{\delta V(1)},\end{aligned} \tag{2.138}$$

where the term $\delta(1,2)\delta(1,3)$ comes from the equation satisfied by G_0^{-1} (equation (2.92)). The

following identity is useful to express the vertex in terms of just the Green's function [79]

$$\begin{aligned}\frac{\delta}{\delta V(5)} &= \int d1d2 \frac{\delta G(1,2)}{\delta V(5)} \frac{\delta}{\delta G(1,2)}, \\ &= -\int d1d2d3d4 G(1,4) \frac{\delta G^{-1}(4,3)}{\delta V(5)} G(3,2) \frac{\delta}{\delta G(1,2)}, \\ &= \int d1d2d3d4 G(1,4)\Gamma(5;4,3)G(3,2)\frac{\delta}{\delta G(1,2)}. \end{aligned} \tag{2.139}$$

This means, that the vertex equation (2.138) can be expressed as:

$$\Gamma(1;2,3) = \delta(1,2)\delta(1,3) + \int d4d5d6d7 G(4,7)\Gamma(1;6,7)G(6,5)\frac{\delta\Sigma^*(2,3)}{\delta G(4,5)}. \tag{2.140}$$

The diagram of the vertex is a sum of a point and a so-called kernel, defined in terms of the self-energy derivative, coupled with the vertex itself (this means that the vertex function is non linear and for a full solution to be found it is necessary to iterate),

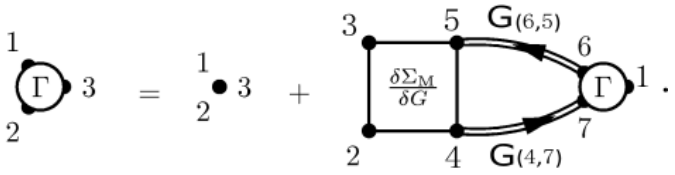

Finally, the fifth equation is constructed from equation (2.105) [79, 85]. In our notation this reads as:

$$\left[i\frac{\partial}{\partial t} - h_0\right] G(1,2) - \int d3 M(1,3)G(3,2) = \delta(1,2), \tag{2.141}$$

where the matrix $\int d3 M(1,3)G(3,2)$ is a special case for the two particle Green's function, *i.e.*,

$$\begin{aligned}\int d3 M(1,3)G(3,2) &= i\int d3 G_2(1,2,3,3^\dagger)v(1,3), \\ &= \int d3 \frac{\langle N|\hat{T}S\hat{\Psi}(1)\hat{\Psi}^\dagger(2)\hat{n}(3)|N\rangle}{\langle N|S|N\rangle} v(1,3). \end{aligned} \tag{2.142}$$

The two particle Green's function satisfies the property:

$$\frac{\delta G(1,2)}{\delta\varphi(3)} = G(1,2)G(3,3^\dagger) - G_2(1,2,3,3^\dagger). \tag{2.143}$$

By replacing it on (2.142), we obtain

$$\begin{aligned}\int d3 M(1,3)G(3,2) &= i\int d3 G(1,2)G(3,3^\dagger)v(1,3) - i\int d3 \frac{\delta G(1,2)}{\delta\varphi(3)} v(1,3), \\ &= iG(1,2)v_H(1) - i\int d3 \frac{\delta G(1,2)}{\delta\varphi(3)} v(1,3). \end{aligned} \tag{2.144}$$

Thus, equation (2.141) will be given by

$$\left[i\frac{\partial}{\partial t} - h_0 - v_H\right] G(1,2) + i\int d3 \frac{\delta G(1,2)}{\delta \varphi(3)} v(1,3) = \delta(1,2). \tag{2.145}$$

Equation (2.145) represents the motion of the Green's propagator when interactions are turned on. The last quantity on the left hand side can be understood in terms of the irreducible self-energy $\Sigma^*(1,3)$[79, 85]:

$$\int \Sigma^*(1,3)G(3,2) = i\int d3 v(1,3)\frac{\delta G(1,2)}{\delta \varphi(3)} = i\int d3 W(1,3)\frac{\delta G(1,2)}{\delta V(3)}, \tag{2.146}$$

where for the last equality it was use the property in eq. (2.126). In order to isolate Σ^* we multiply both sides by the inverse of the green's function [79], so:

$$\begin{aligned}\Sigma^*(1,2) &= i\int d3d4 W(1,3)\frac{\delta G(1,4)}{\delta V(3)} G^{-1}(4,2), \\ &= -i\int d3d4 W(1,3)G(1,4)\frac{\delta G^{-1}(4,2)}{\delta V(3)},\end{aligned} \tag{2.147}$$

where for the last equality we have used the identity derived from $\int d3 G^{-1}(1,3)G(3,2) = \delta(1,2)$:

$$\int d3 \frac{\delta G^{-1}(1,3)}{\delta V(4)} G(3,2) + \int d3 G^{-1}(1,3)\frac{\delta G(3,2)}{\delta V(4)} = 0. \tag{2.148}$$

The last derivative in (2.147) is the vertex definition. Then, the fifth Hedin's equation for the irreducible self energy is obtained:

$$\Sigma^*(1,2) = i\int d3d4 W(1,3)\Gamma(3;4,2)G(1,4). \tag{2.149}$$

As usual, the Feynmann diagram corresponding to the irreducible self energy is:

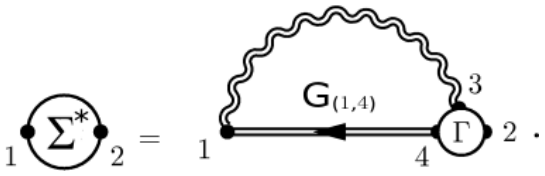

Hedin's equations are self consistent. As we can see in the figure 2.1 one variable depends on the previous calculation, forming a loop. In order to extract the correct solution there must be several iterations [64]. Computationally speaking, several iterations take a large amount of time, since the calculation itself of each of Hedin's equations corresponds to several sum over the bands and k points in reciprocal space. For this reason, approximations have to be done, the first is the so-called GW approximation which will be explored in the next section.

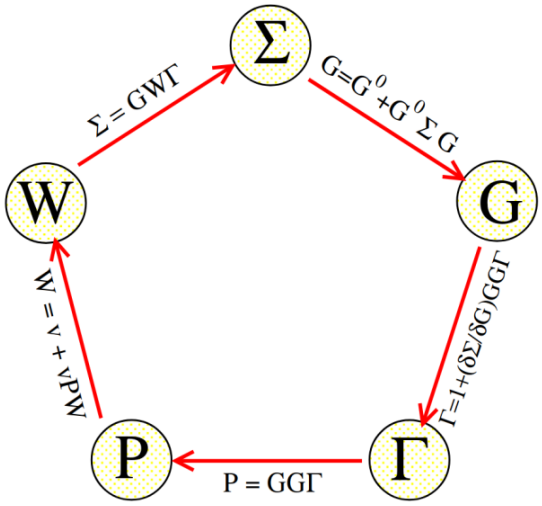

Figure 2.1: Self consistency of Hedin's equations

2.3.4 GW approximation

For the so-called GW approximation, the vertex corrections are set to be

$$\Gamma(1;2,3) \approx \delta(1,2)\delta(1,3). \tag{2.150}$$

Consequently, the screened polarization is described by:

$$\Pi^*(1,2) = -iG(1,2)G(2,1), \tag{2.151}$$

and, the irreducible self energy becomes

$$\Sigma^*(1,2) = iG(1,2)W(1,2), \tag{2.152}$$

thus explaining the name "GW" approximation. Equation (2.141) can be written in a better form if we replace the field operators entering the Green's function by the wave functions, *i.e.*, the quasiparticle equation [64, 85],

$$(T + u_{\text{ext}} + v_H)\,\Psi^{QP}_{nk}(r) + \int d^3r'\Sigma(r,r',E^{QP}_{nk})\Psi^{QP}_{nk}(r') = E^{QP}_{nk}(r), \tag{2.153}$$

where u_{ext} corresponds to the periodic potential of the ions, and the wave functions $\Psi^{QP}_{nk}(r)$ correspond to the ground state wave function for the non interacting system (which, in principle could be considered as the KS wave functions since the KS scheme assumes independent electrons in an effective potential that play, the role of the interactions). It is important to notice that the $\Psi^{QP}_{nk}(r)$ are going to vary since the self energy $\Sigma(r,r',E^{QP}_{nk})$ is self consistent. For the simplest case, just one iteration will be enough [64]. However, self consistency with respect to wavefunctions can be introduced by the scQPGW method [87, 88].
Additionally, there is a restriction for the quasiparticle energies $E^{QP}_{nk}(r)$ to be real. If the DFT

wavefunctions are considered, the quasiparticle energies take the value [64, 85]:

$$E_{nk}^{QP} = Re\left[\left\langle\psi_{nk}^{KS}\right| T + u_{\text{ext}} + v_H + \Sigma^*(E_{nk}^{QP})\left|\psi_{nk}^{KS}\right\rangle\right]. \tag{2.154}$$

Now we need the QP approximation, where the energy is Taylor expanded in terms of the self energy. This is achieved, first by deducing the energy of an $N+1$ particle system:

$$E^{N+1} = E_{nk}^{N} + Re\left[\left\langle\psi_{nk}^{KS}\right|\Sigma^*(E_{nk}^{N+1})\left|\psi_{nk}^{KS}\right\rangle\right], \tag{2.155}$$

A Taylor expansion of the self energy around E_{nk}^{N} yields

$$\begin{aligned} E^{N+1} =& E_{nk}^{N} + Re\left[\left\langle\psi_{nk}^{KS}\right|\Sigma^*(E_{nk}^{N})\left|\psi_{nk}^{KS}\right\rangle\right] \\ &+ (E_{nk}^{N+1} - E_{nk}^{N}) Re\left[\left\langle\psi_{nk}^{KS}\right|\frac{\partial\Sigma^*(\omega)}{\partial\omega}|_{\omega=E_{nk}^{N}}\left|\psi_{nk}^{KS}\right\rangle\right], \end{aligned} \tag{2.156}$$

then we replace the quantity $E_{nk}^{N+1} - E_{nk}^{N}$ with equation (3.38) to obtain

$$\begin{aligned} E^{N+1} =& E_{nk}^{N} + Re\left[\left\langle\psi_{nk}^{KS}\right|\Sigma^*(E_{nk}^{N})\left|\psi_{nk}^{KS}\right\rangle\right] \\ &+ Re\left[\left\langle\psi_{nk}^{KS}\right|\Sigma^*(E_{nk}^{N+1})\left|\psi_{nk}^{KS}\right\rangle\right] Re\left[\left\langle\psi_{nk}^{KS}\right|\frac{\partial\Sigma^*(\omega)}{\partial\omega}|_{\omega=E_{nk}^{N}}\left|\psi_{nk}^{KS}\right\rangle\right]. \end{aligned} \tag{2.157}$$

Lastly, we introduce the normalization factor Z_{nk}^{N} that accounts for the fact that the weights of the QP peaks are reduced at the cost of emerging satellites [64], *i.e.*,

$$Z_{nk}^{N} = \left(1 - Re\left[\left\langle\psi_{nk}^{KS}\right|\frac{\partial\Sigma^*(\omega)}{\partial\omega}|_{\omega=E_{nk}^{N}}\left|\psi_{nk}^{KS}\right\rangle\right]\right), \tag{2.158}$$

so, the quasiparticle QP energies can be approximated as

$$E_{nk}^{N+1} = E_{nk}^{N} + Z_{nk} Re\left[\left\langle\psi_{nk}^{KS}\right|\Sigma^*(E_{nk}^{N})\left|\psi_{nk}^{KS}\right\rangle\right], \tag{2.159}$$

which represents the QP corrections for the energies.
As it is appreciated we need the previous calculation to get higher energies (*i.e.*, iterations on energy). However, for calculating the energy, it is necessary to obtain first the irreducible self energy Σ^*. From this point, we are going to work parallel with the equations presented by Marini et al. [69] in order to map this GW picture with the computational software we are going to use in chapter 4.

The self energy $\left\langle\psi_{nk}^{KS}\right|\Sigma^*(E_{nk}^{N})\left|\psi_{nk}^{KS}\right\rangle$ can be expanded when we use the GW approxima-

tion and the Dyson equation

$$\begin{aligned}\left\langle \psi_{nk}^{KS}\right| \Sigma^*(E_{nk}^N)\left|\psi_{nk}^{KS}\right\rangle &= \left\langle \psi_{nk}^{KS}\right| G(E_{nk}^N)W(E_{nk}^N)\left|\psi_{nk}^{KS}\right\rangle, \\ &= \left\langle \psi_{nk}^{KS}\right| G_0(E_{nk}^N)W(E_{nk}^N)\left|\psi_{nk}^{KS}\right\rangle, \\ &+ \left\langle \psi_{nk}^{KS}\right| G_0(E_{nk}^N)\Sigma^* G(E_{nk}^N)W(E_{nk}^N)\left|\psi_{nk}^{KS}\right\rangle, \end{aligned} \tag{2.160}$$

where the first term on the right hand side can be expressed in terms of the dielectric function (by using the screened Coulomb definition),

$$\begin{aligned}\left\langle \psi_{nk}^{KS}\right| G_0 W\left|\psi_{nk}^{KS}\right\rangle &= \left\langle \psi_{nk}^{KS}\right| G_0 v\left|\psi_{nk}^{KS}\right\rangle + \left\langle \psi_{nk}^{KS}\right| G_0 v\Pi^* W\left|\psi_{nk}^{KS}\right\rangle, \\ &= \left\langle \psi_{nk}^{KS}\right| G_0 v\left|\psi_{nk}^{KS}\right\rangle + \left\langle \psi_{nk}^{KS}\right| G_0 v\Pi v\left|\psi_{nk}^{KS}\right\rangle, \\ &= \left\langle \psi_{nk}^{KS}\right| G_0 v\varepsilon^{-1}\left|\psi_{nk}^{KS}\right\rangle. \end{aligned} \tag{2.161}$$

In the last step we have used the dielectric equation (2.75). On the other hand, the term $\left\langle \psi_{nk}^{KS}\right| G_0(E_{nk}^N)\Sigma^* G(E_{nk}^N)W(E_{nk}^N)\left|\psi_{nk}^{KS}\right\rangle$ is rather difficult to analize, so it is approximated to $\left\langle \psi_{nk}^{KS}\right| v\left|\psi_{nk}^{KS}\right\rangle$ due to the fact that for high frequencies ($\omega \to \infty$) the dielectric constant becomes 1 and the Coulomb interaction tends to the unscreened v [64]. This approximation corresponds to the exchange self-energy and is given in reciprocal space by:

$$\Sigma_{nk}^x = -\sum_m \int_{BZ} \frac{d\mathbf{q}}{(2\pi)^3} \sum_{\mathbf{G}} v(\mathbf{q}+\mathbf{G})|\rho_{nm}(\mathbf{k},\mathbf{q},\mathbf{G})|^2 f_{m(\mathbf{k}-\mathbf{q})}, \tag{2.162}$$

where $\rho_{nm}(\mathbf{k},\mathbf{q},\mathbf{G}) = \left\langle \Psi_{nk}^{KS}\right| \exp[i(\mathbf{q}+\mathbf{G}).\mathbf{r}]\left|\Psi_{nk}^{KS}\right\rangle$ are the reciprocal lattice vectors (the indexes n and m represent the bands), $v(\mathbf{q}+\mathbf{G}) = 4\pi/|\mathbf{q}+\mathbf{G}|^2$, and $f_{m(\mathbf{k}-\mathbf{q})}$ is the occupation function (1 or 0 for occupied and unoccupied states respectively). On the other hand, equation (2.161) is the correlation part of the self energy, and is expressed in reciprocal space by

$$\begin{aligned}\Sigma_{nk}^c(\omega) = i\sum_m \int_{BZ} \frac{d\mathbf{q}}{(2\pi^3)} \sum_{\mathbf{G},\mathbf{G}'} \frac{4\pi}{|\mathbf{q}+\mathbf{G}|^2} \rho_{nm}(\mathbf{k},\mathbf{q},\mathbf{G})\rho_{nm}^*(\mathbf{k},\mathbf{q},\mathbf{G}) \\ \mathrm{x}\int d\omega' G_{m\mathbf{k}-\mathbf{q}}^0(\omega-\omega')\varepsilon_{\mathbf{G}\mathbf{G}'}^{-1}(\mathbf{q},\omega'). \end{aligned} \tag{2.163}$$

So, in order to get the correlation part of Self energy, the dielectric function can be calculated from the reducible polarization Π which would be represented by χ:

$$\varepsilon_{\mathbf{G},\mathbf{G}'}^{-1}(\mathbf{q},\omega) = \delta_{\mathbf{G}\mathbf{G}'} + v(\mathbf{q}+\mathbf{G})\chi_{\mathbf{G}\mathbf{G}'}(\mathbf{q},\omega), \tag{2.164}$$

and the relation between the irreducible (χ^0) and reducible (χ) polarizations (According to equation (2.128)) can be expressed in reciprocal space as

$$\chi_{\mathbf{G},\mathbf{G}'}(\mathbf{q},\omega) = [\delta_{\mathbf{G},\mathbf{G}'} - v(\mathbf{q}+\mathbf{G}'')\chi_{\mathbf{G},\mathbf{G}'}^0(\mathbf{q},\omega)]^{-1}\chi_{\mathbf{G}'',\mathbf{G}'}^0(\mathbf{q},\omega). \tag{2.165}$$

Due to the GW approximattion we are able to determine the irreducible polarization χ^0 in terms of the Green's functions. But since the Green's functions depend on the QP energies trough the self energy, it is reasonable to take the RPA approximation [69] here and let χ^0 be the KS polarization Π^{KS} (equation (2.61)) in order to avoid self-consistency,

$$\chi^0_{\mathbf{G},\mathbf{G}'}(\mathbf{q},\omega) = 2\sum_{mn'}\int_{BZ}\frac{d\mathbf{k}}{(2\pi)^3}\rho^*_{n'n\mathbf{k}}(\mathbf{qG})\rho_{n'n\mathbf{k}}(\mathbf{q},\mathbf{G}')f_{n\mathbf{k}-\mathbf{q}}(1-f_{n'\mathbf{k}}) \\ \mathrm{x}\left[\frac{1}{\omega+E_{n\mathbf{k}-\mathbf{q}}-E_{n'\mathbf{k}}+i\eta}-\frac{1}{\omega+E_{n'\mathbf{k}}-E_{n\mathbf{k}-\mathbf{q}}-i\eta}\right]. \tag{2.166}$$

This last equation represents the whole skeleton of the GW approximation. Once it is calculated, we can start computing the equations until we arrive to the final quasiparticle energies and to the GW bandstructure.

2.4 Bethe Salpeter equation

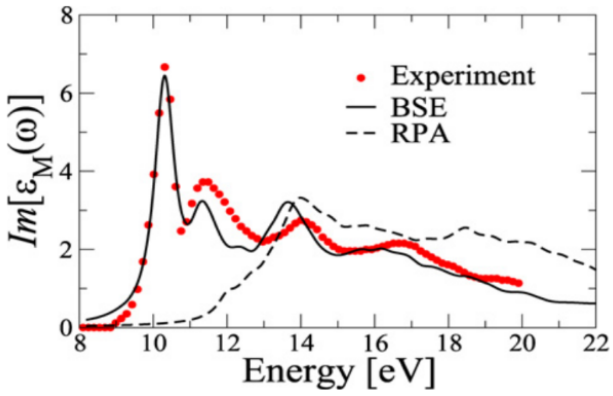

Figure 2.2: Optical spectra of SiO_2 for different levels of theory: experiment (red dots), BSE (black lines) and RPA (black segmented lines) extracted from [69]

The absorption spectrum can be calulated from the relation between the microscopic dielectric constant and the macroscopic via equation (2.72) (eq.14 of [69]). This spectrum obtained from the first iteration of the GW approximation corresponds to the random phase approximation (RPA) case. This is showed when Hedin's equation (2.128) is approximated by equation (2.165), corresponding to the result we arrive in linear response theory section (2.47) (where the RPA case emerges with kernel $f_{xc} = 0$). The discrepancy, arrives for the approximation on the irreducible polarization to be the KS polarization. The result on the RPA for GW shows accurate results when applied to metals in general, due to the efficient screening in the Fermi surface that prevents the formation of excitonic states [69]. However, when applied to semiconductors or insulators, the RPA does not yield optical absorption spectra in good agreement with experiments. For example, in the case of SiO_2, this discrepancy has led to extensive debates about the nature of the four well defined peaks observed in the ex-

periment (shown in figure 2.2). The RPA results are sensitive to the size of the gap correction. Typically, the larger the gap, the less adequate is the RPA [69]. For instance in the case of 10eV gap of SiO_2, the RPA is not even qualitatively correct.

The drawbacks of the RPA can be solved by using a more elaborate equation for Π, that takes into account the effect of electron-electron correlations. This is the Bethe Salpeter equation that can be introduced by the second Green's function $G_2(1,2,3,4)$ [65, 89], *i.e.*, if we start with equation (2.143) with $2 = 1^\dagger$

$$\frac{\delta G(1,1^\dagger)}{\delta\varphi(2)} = G(1,1^\dagger)G(2,2^\dagger) - G_2(1,1^\dagger,2,2^\dagger), \tag{2.167}$$

and replace the right hand side term with the definition for $\Pi(1,2)$ (equation (2.121)):

$$\Pi(1,2) = i(G(1,1^\dagger)G(2,2^\dagger) - G_2(1,1^\dagger,2,2^\dagger)), \tag{2.168}$$

the right hand side of the equation will be the Bethe Salpeter (BSE) term $L(1,1^\dagger,2,2^\dagger)$. Consequently, an analysis of the origin of the two particle Green's function has to be done. This is achieved by making an analogous treatment of the propagator $G(1,2)$ using the Dyson equation. The 4-point Green's function can be decomposed in terms of single propagators (non interacting) plus a reducible kernel term K (similar to the reducible self energy) which accounts for all the intermediate processes [65, 89]:

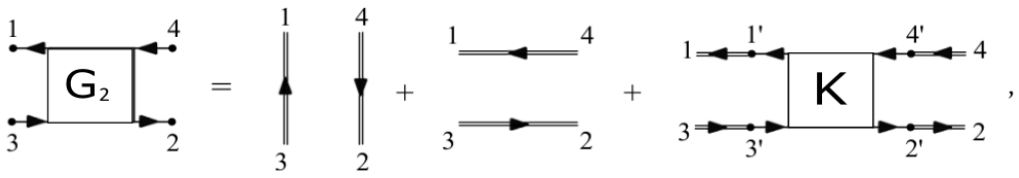

$$\begin{aligned} G_2(1,2,3,4) =& G(1,3)G(2,4) + G(1,4)G(2,3) \\ &+ \int d1'd2'd3'd4'G(1,1')G(3,3')K(1',2',3',4')G(4',4)G(2,2'), \end{aligned} \tag{2.169}$$

where the reducible kernel is the sum of all the Feynmann diagrams that could happen between points 1, 2 and 3, 4:

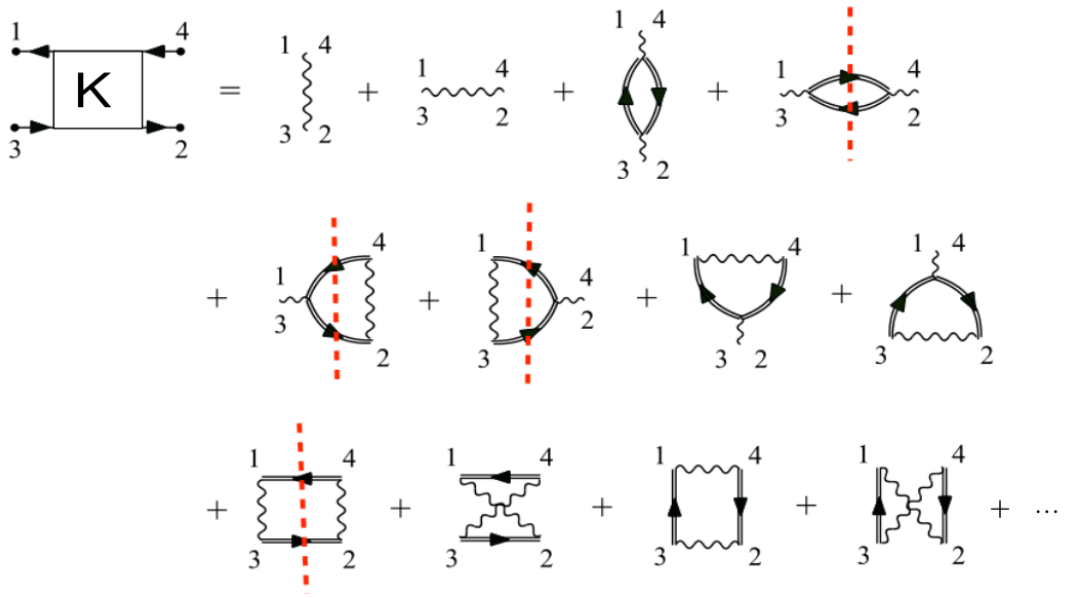

However, as in the case with the reducible self-energy, the reducible kernel can be written in terms of the irreducible one (by counting not divisible diagrams) K^*,

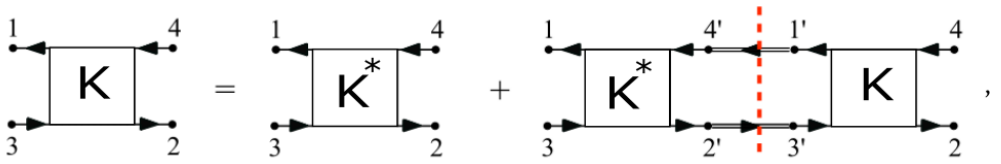

$$K(1,2,3,4) = K^*(1,2,3,4) + \int K^*(1,2',3,4')G(4',1')G(3',2')K(1',2,3',4). \tag{2.170}$$

So, the propagator is drawn in terms of the irreducible kernels:

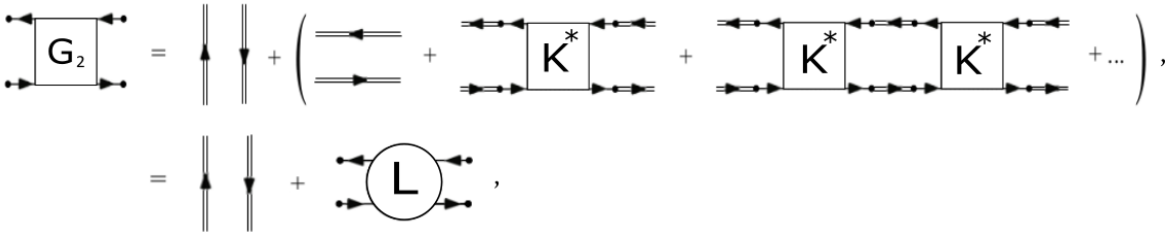

$$G_2(1,2,3,4) = G(1,3)G(2,4) + L(1,2,3,4). \tag{2.171}$$

where the last term $L(1,2,3,4)$ corresponds to the Bethe Salpeter equation [89]:

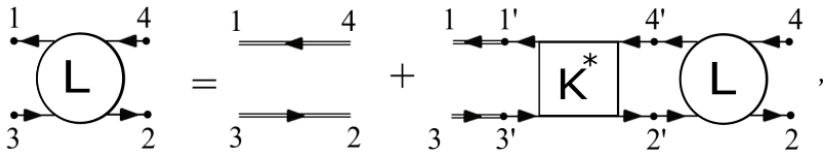

$$L(1,2,3,4) = G(1,4)G(2,3) + \int d1'd2'd3'd4'G(1,1')G(3',3)K^*(1',2',3',4')L(4',2,2',4). \quad (2.172)$$

The first term in the definition of $L(1,2,3,4)$ is called L_0 and the BSE is given more commonly as:

$$L(1,2,3,4) = L_0(1,2,3,4) + \int d1'd2'd3'd4'L_0(1,1',3,3')K^*(1',2',3',4')L(4',2,2',4). \quad (2.173)$$

Finally, the relation between L and Π becomes clear thanks to (2.171) and (2.168) ,

$$\Pi(1,2) = -iL(1,2,1^\dagger,4^\dagger). \quad (2.174)$$

So, the calculation of L becomes the skeleton to built the construction of the dielectric constant, and, the irreducible kernel K^* is now the variation of the self-energy with respect to the two point Green's function [89]:

$$K^*(1,2,3,4) = \pm\frac{\delta\Sigma(1,3)}{\delta G(4,2)}. \quad (2.175)$$

This is shown more clearly diagrammatically:

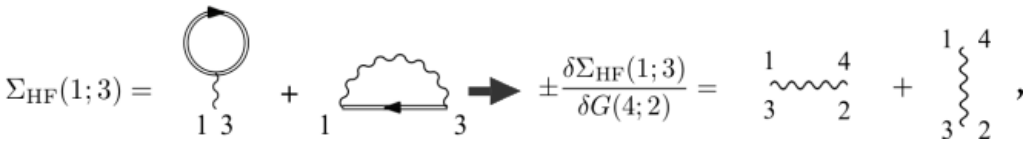

where we can extract the Hartree term for interaction between two particles $\delta\Sigma_H(1,3)/\delta G(4,2) = i\delta(1,3)\delta(2,4)v(1,2)$ (4-point Coulomb interaction). So, the rest of the contributions are enclosed in the exchange-correlation kernel,

$$\tilde{K}^*(1,2,3,4) = K^*(1,2,3,4) - i\delta(13)\delta(2,4)v(1,2), \quad (2.176)$$

where

$$\tilde{K}^*(1,2,3,4) = -\frac{\delta\Sigma_{xc}(1,3)}{\delta G(4,2)}. \quad (2.177)$$

This means that the calculation of the kernel $K^*(1,2,3,4)$ and $L(1,2,3,4)$ is for the exchange correlation self-energy obtained within the the GW approximattion. The BS equation can be

written as:

$$L(1234) = L_0(1,2,3,4) + \int d1'd2'd3'd4' L_0(1,3,1',3')\Big(\delta(1,3)\delta(2,4)v(1,2) - \frac{\delta\Sigma_{xc}(1,3)}{\delta G(4,2)}\Big)L(2,2',4,4'), \tag{2.178}$$

forming a Dyson like equation for L [65, 89]. However, the exchange-correlation self-energy is,

$$\Sigma_{xc} = \Sigma - \Sigma_H, \tag{2.179}$$

and, the derivatives with respect to the propagator gives the interactions, *i.e.*,

$$\begin{aligned}
\frac{\delta\Sigma_{xc}(1,3)}{\delta G(4,2)} &= \frac{\delta\Sigma(1,3)}{\delta G(4,2)} - \frac{\delta\Sigma_H(1,3)}{\delta G(4,2)}, \\
\frac{\delta\Sigma_{xc}(1,3)}{\delta G(4,2)} &= \delta(1,3)\delta(2,4)W(1,2) - \delta(1,3)\delta(2,4)v(1,2), \\
\frac{\delta\Sigma_{xc}(1,3)}{\delta G(4,2)} &= \delta(1,3)\delta(2,4)(W(1,2) - v(1,2)).
\end{aligned} \tag{2.180}$$

where the GWA has been used ($\Sigma(1,3) = iG(1,3)W(1,3)$), and the term $i\dfrac{G(1,3)\delta W(1,3)}{\delta G(4,2)}$ has been omitted [90]. So, equation 2.178 is now in terms of the unscreened ($v(1,2)$) and screened ($W(1,2)$) interactions calculated for QP corrections:

$$\begin{aligned}
L(1234) &= L_0(1,2,3,4) + \int d1'd2'd3'd4' L_0(1,3,1',3')\Big(\delta(1,3)\delta(2,4)\left[2v(1,2) - W(1,2)\right]\Big)L(2,2',4,4'), \\
L(1234) &= L_0(1,2,3,4) + \int d1'd2'd3'd4' L_0(1,3,1',3')\delta(1,3)\delta(2,4)\Xi L(2,2',4,4').
\end{aligned} \tag{2.181}$$

The BSE approach to find the absorption spectra gives us the contribution that electron-hole interaction (excitons) has in semiconductors and insulators. Even more importantly, it gives us complete information on the behavior of exciton wave functions. The results shows that BSE approach only gives a minor modification with the experiment [69] result as shown in figure 2.2.

Before concluding this chapter, we make a brief summary of the steps of the method and the approximations used in the determination of optical spectra in BSE. The figure 2.3 will be followed:

- First, the initial calculation correspond to a DFT one, a ground state calculation where the KS eigenvalues (ϵ_n) and wavefunctions (φ_n) are determined. **Approximations**: The use of pseudo-potentials and GGA for exchange-correlation energy.

- Second, the dielectric function calculation is performed after the calculation of the KS polarization Π^{KS}. **Approximations**: The dielectric matrix can be calculated within the

RPA.

- Third, the GW approximation is used to find the self energy, and, the quasiparticle energy corrections E_{QP}. **Approximations**: The use of GWA and the plasmon-pole approximation (PPA) to determine ε^{-1}, and the screening $W = v\varepsilon^{-1}$. Sometimes, when the band structure of the system does not change significantly in comparison to GGA bands (*i.e.*, the bands has been pulled apart), we can use the so-called rigid shift to avoid the dynamical screening and goes directly to the next step.

- Fourth, the static limit of the screening ($\varepsilon^{-1}(q,\omega = 0)$), the kernel Ξ and the polarization Π^{QP} (the GW-RPA) arising from QP corrections are calculated. **Approximations**: The static limit of W is taken. The KS wavefunctions are used to built Π^{QP} within the RPA. In addition, it is worth to say that the static screening for calculating $W = v\varepsilon^{-1}$ has been further implemented in the light of results [69, 91], showing it is show that dynamical effects in the screening are partially compensated by those of the Green's function [90].

- Fifth, the BSE calculation is performed, using Π^{QP} and Ξ. **Approximations**: Only the resonant part of the excitonic Hamiltonian (which comes from the yambo approach to solve BS equation [69]) is calculated. Once BSE is solved, the binding energies of the excitons and their wavefunctions are determined.

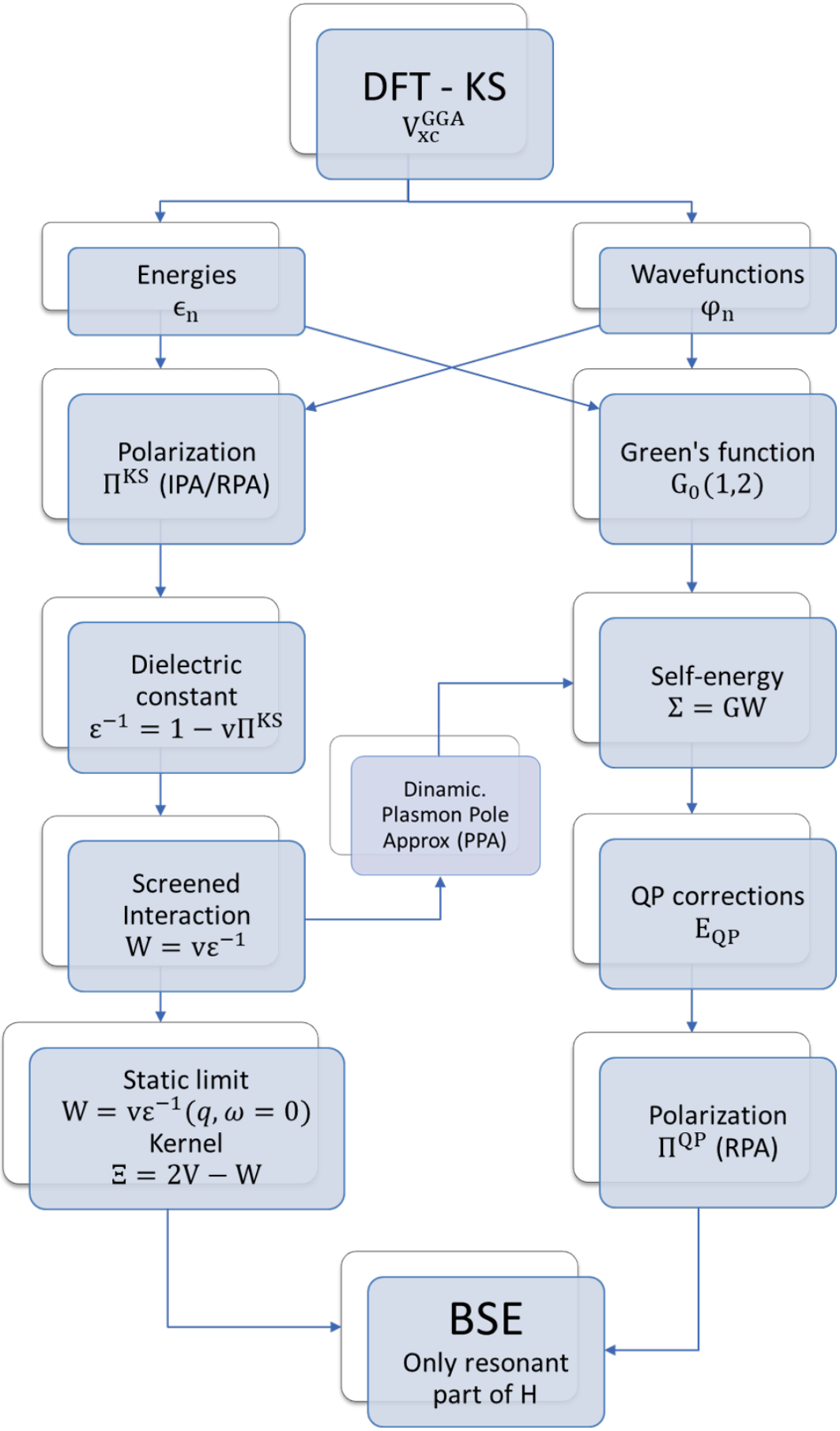

Figure 2.3: Scheme for BSE calculation inspired from [90]

CHAPTER 3

Hydrogen Effective Model

In order to get a more fundamental insight into the problem, we address the properties of excitons (such as binding energies and wavefunctions) obtained with BSE calculation by using a two-dimensional effective theory. Since QPMBPT is based on the idea of screening as we have seen in the previous chapter. The screened Coulomb interaction for isolated single layers is necessary. This was first done by Keldysh who was interested in thin semiconducting films [92]. He derived an analytical expression of the screened Coulomb interaction for metal and semiconductor thin films. On the other hand, it is also necessary a description of the exciton based in its structure which, basing on the idea that is formed by an electron and a hole (or positron), could be treat as a hydrogen-like atom. So, the hydrogen effective model is based on the idea that a hydrogen-like atom, composed with e-h (exciton), interacts with an screening potential (which for our case layer materials should be in two dimensions).
The hydrogen effective model for excitons has been treated in previous works for honeycomb monolayer systems [93, 94, 95], e.g MoS_2 and WS_2, with good agreements in comparison to experimental results. Furthermore, the treatment can be extended to anisotropic systems by adding the anisotropy to the effective mass on the Hamiltonian as is done for black phosphorus in [43, 96] with excellent agreement. In particular, [96] solves the Schrodinger equation of the system by using the Numerov method. The advantage of this simple model of excitons is that their results are less expensive (computationally speaking) in contrast to QPMBPT results, so, they can be used in other areas of research on single layer materials. For this reason, in order to enrich the knowledge on the hydrogen effective model, we are applying it on tellurene allotropes. In this chapter I will derive the 2D excitonic model that we will apply in chapter 4.

3.1 2D screened potential

The Coulomb interaction on dielectric sheets has a non-trivial form due to screening [92]. Two works reproduce the Keldysh calculation in a more simple way for a monolayer built on vacuum and on top of a dielectric slab [96, 97]. We will follow the work of P. Cudazzo and V. Tokatly et al.

The system under consideration consists of a dielectric sheet confined on the plane $z = 0$ embedded into vacuum and subject to an external potential $\phi_{\text{ext}}(\mathbf{r})$ [97]. The electric potential is produced by a point charge located at the origin, thus having a charge distribution $n_{\text{ext}}(\mathbf{r}) = e\delta(\mathbf{r})$ [97]. So, the electric potential of the system is described by the Poisson's equation,

$$\nabla^2\phi(\mathbf{r}) = -4\pi n(\mathbf{r}), \tag{3.1}$$

where $n = n_{\text{ext}} + n_{\text{ind}}$ is the contribution from the external charge density and the induced charge density on the monolayer. The induced charge density is confined on the xy-plane at $z = 0$, and is related to the 2D macroscopic polarization $\mathbf{P}_{2D}$ (in the long wave length limit)

[97] through

$$n_{\text{ind}} = -\nabla \cdot \mathbf{P}_{2D}, \tag{3.2}$$

which is proportional to the electric field inside the plane $z = 0$. The 2D polarizability α_{2D} of the dielectric sheet is related to the polarization:

$$\mathbf{P}_{2D}(\rho) = -\alpha_{2D}\nabla_{\rho}\phi(\rho, z = 0), \tag{3.3}$$

where ρ is the radial component in polar coordinates and $\phi(\mathbf{r}, z = 0)$ is the in-plane potential. By replacing equation (3.3) into (3.2) we get an expression of the induced charge density in terms of the macroscopic potential at $z = 0$ [97], *i.e.*,

$$n_{\text{ind}}(\mathbf{r}) = \delta(z)\alpha_{2D}\nabla_{\rho}^2\phi(\rho, z = 0). \tag{3.4}$$

Consequently, the Poisson equation reads:

$$\nabla^2\phi(\mathbf{r}) = -4\pi e\delta(\mathbf{r}) - 4\pi\alpha_{2D}\nabla_{\rho}^2\phi(\rho, z = 0)\delta(z), \tag{3.5}$$

and, in the reciprocal space is:

$$(|\mathbf{q}|^2 + k_z^2)\phi(\mathbf{q}, k_z) = 4\pi e - 4\pi\alpha_{2D}|\mathbf{q}|^2 \int \frac{dk_z}{2\pi}\phi(\mathbf{q}, k_z), \tag{3.6}$$

where $\mathbf{q}$ corresponds to the reciprocal transform for x, y components of ρ. The k_z component defines the reciprocal of z and is left in its integral form on the last right hand term in order to define the 2D potential $\phi_{2D}(\mathbf{q})$ [97], *i.e.*,

$$\phi_{2D}(\mathbf{q}) = \int \frac{dk_z}{2\pi}\phi(\mathbf{q}, k_z). \tag{3.7}$$

For solving equation (3.6), it is necessary first to find the derivation over k_z:

$$\frac{d\phi(\mathbf{q}, k_z)}{dk_z} = -\frac{2k_z}{|\mathbf{q}|^2 + k_z^2}\phi(\mathbf{q}, k_z). \tag{3.8}$$

And, integrate to obtain $\phi(\mathbf{q}, k_z)$:

$$\begin{aligned} \int \frac{d\phi}{\phi} &= \int -\frac{2k_z}{|\mathbf{q}|^2 + k_z^2}, \\ \phi(\mathbf{q}, k_z) &= \frac{A(\mathbf{q})}{|\mathbf{q}|^2 + k_z^2}, \end{aligned} \tag{3.9}$$

where A is a function that depends only on $\mathbf{q}$ and can be determined with another integra-

tion of $\phi(\mathbf{q}, k_z)$ over k_z as follows:

$$\begin{aligned}\int_{-\infty}^{+\infty} \phi(\mathbf{q}, k_z)\, dk_z &= 2\pi\phi_{2D}(\mathbf{q}),\\ \int_{-\infty}^{+\infty} \frac{A(\mathbf{q})}{|\mathbf{q}|^2 + k_z^2}\, dk_z &= 2\pi\phi_{2D}(\mathbf{q}),\end{aligned} \tag{3.10}$$

so:

$$\begin{aligned}A(\mathbf{q})\frac{\arctan\left(\frac{k_z}{\mathbf{q}}\right)}{\mathbf{q}}\Big|_{-\infty}^{+\infty} &= 2\pi\phi_{2D}(\mathbf{q}),\\ A(\mathbf{q}) &= 2\mathbf{q}\phi_{2D}(\mathbf{q}).\end{aligned} \tag{3.11}$$

Thus, the corresponding $\phi(\mathbf{q}, k_z)$ in terms of $\phi_{2D}(\mathbf{q})$ is:

$$\phi(\mathbf{q}, k_z) = \frac{2\mathbf{q}\phi_{2D}(\mathbf{q})}{|\mathbf{q}|^2 + k_z^2}. \tag{3.12}$$

And, by replacing on (3.6) we get:

$$\phi_{2D}(\mathbf{q}) = \frac{2\pi e}{|\mathbf{q}|(1 + 2\pi\alpha_{2D}|\mathbf{q}|)}. \tag{3.13}$$

Which defines the 2D macroscopic screening of a point charge. The most notorious difference with respect to the bulk case, is that the dielectric constant $\varepsilon(\mathbf{q})$ depends intrinsically on $\mathbf{q}$, *i.e.*,

$$\varepsilon(\mathbf{q}) = 1 + 2\pi\alpha_{2D}|\mathbf{q}|. \tag{3.14}$$

The inverse Fourier transform of (3.13) is

$$\phi_{2D}(\rho) = \frac{1}{(2\pi)^2}\int_0^{+\infty}\int_0^{2\pi} q\, dq\, d\psi \frac{2\pi e}{q(1 + 2\pi\alpha_{2D}q)} e^{iq\rho\cos(\theta-\psi)}, \tag{3.15}$$

where it has been intrinsically define $\vec{\mathbf{q}} = (q_x, q_y) = (q\cos(\psi), q\,\mathrm{sen}(\psi))$ and $\vec{\rho} = (\rho_x, \rho_y) = (\rho\cos(\theta), \rho\sin(\theta))$, so, $\vec{\mathbf{q}}.\vec{\rho} = q\rho\cos(\theta - \psi)$. And, by using the definition of the first kind Bessel function of 0^{th} order:

$$J_0(z) = \frac{1}{2\pi}\int_0^{2\pi} e^{iz\cos\theta d\theta}, \tag{3.16}$$

we find:

$$\phi_{2D}(\rho) = e\int_0^{+\infty} q\, dq \frac{1}{q(1 + 2\pi\alpha_{2D}q)} J_0(q\rho), \tag{3.17}$$

which corresponds to the 0^{th} order Hankel transform and has an analytical solution with the property:

$$\int_0^{+\infty} q\left(\frac{1}{q(q+a)}\right) J_0(qs)\, dr = \frac{\pi}{2}\left[H_0(as) - Y_0(as)\right], \tag{3.18}$$

where the H_0 and Y_0 are the Struve function and second kind Bessel function respectively. By taking the value of $a = 1/r_0 = 1/2\pi\alpha_{2D}$, equation (3.17) reads as:

$$\phi_{2D} = \frac{e}{4\alpha_{2D}}\left[H_0(\frac{\rho}{r_0}) - Y_0(\frac{\rho}{r_0})\right]. \tag{3.19}$$

The effective interaction energy of an electron with the potential on the monolayer ($V = e\phi_{2D}$) is

$$V(\rho) = \frac{e^2}{4\alpha_{2D}}\left[H_0(\frac{\rho}{r_0}) - Y_0(\frac{\rho}{r_0})\right]. \tag{3.20}$$

From this result, it is easy to generalize to the case where the monolayer lies on top of a substrate (this means the substrate is localized at $z < 0$) with susceptibility χ and a dielectric constant $\varepsilon_s = 1 + 4\pi\chi$ [96], *i.e.*,

$$V(\rho) = \frac{e^2}{4k\alpha_{2D}}\left[H_0(\frac{\rho}{r_0}) - Y_0(\frac{\rho}{r_0})\right], \tag{3.21}$$

where k is $(1+\varepsilon_s)/2$. Even a further generalization can be done if we let the 2D polarization α_{2D} to be anisotropic, *i.e.*, it behaves like a tensor. This will be analyzed further in appendix 1 for our particular system of β-Te.

Let's now construct the potential in a simpler way by analyzing the asymptotic behavior of equation (3.20) in the cases where goes to zero and infinity. In the first scenario, the contribution only arises from the Bessel function, *i.e.*,

$$\mathrm{Lim}_{\rho\to 0} V(\rho) \approx -\frac{1}{r_0}\left[\ln(\frac{\rho}{2r_0}) + \gamma\right], \tag{3.22}$$

where $\gamma \approx 0.5772$ is the Euler's constant. On the other hand, for high values both the Struve and Bessel functions tend to $1/\rho$:

$$\mathrm{Lim}_{\rho\to+\infty} V(\rho) \approx \frac{1}{\rho}. \tag{3.23}$$

The simplest matching of both asymptotic results gives the so-called Keldysh interaction [92, 97]:

$$V_K(\rho) = -\frac{e^2}{r_0}\left[\ln(\frac{\rho}{\rho + r_0}) + (\gamma - Ln2)e^{-\frac{\rho}{r_0}}\right], \tag{3.24}$$

which provides an accurate description of the effective interaction for intermediate values of ρ/r_0 as it can be seen in the figure (3.1)

The two-dimensional effective potential can be understood better if the equation (3.13) is rewritten as:

$$\phi_{2D}(\mathbf{q}) = \int_{-\infty}^{+\infty} dz \frac{2\pi e}{|\mathbf{q}|} e^{-|\mathbf{q}||z|} \frac{e^{|z|/2\pi\alpha_{2D}}}{4\pi\alpha_{2D}}, \tag{3.25}$$

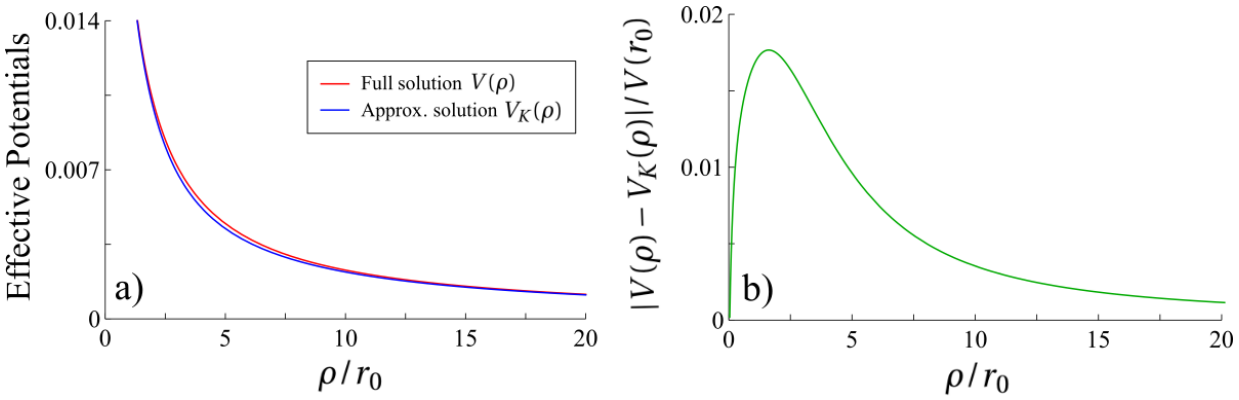

Figure 3.1: a) Comparison between the full solution $V(\rho)$ (eq. (3.21)) and the approximate solution $V_K(\rho)$ (eq. (3.24)). b) Absolute difference between the full and Keldysh potential divided by an increase factor $V(r_0)$

whose Fourier transform is:

$$V(\rho) = e^2 \int_{-\infty}^{+\infty} dz \frac{e^{|z|/r_0}}{2r_0} \left[\int_0^{+\infty} dq e^{iq\rho\cos(\alpha)} \frac{e^{qz}}{q} \right],$$
$$V(\rho) = e^2 \int_{-\infty}^{+\infty} dz \frac{e^2}{\sqrt{\rho^2 + z^2}} \frac{e^{|z|/r_0}}{2r_0}, \tag{3.26}$$

which corresponds to another formulation of equation (3.20). It represents a potential produced by a one dimensional charge distribution of the form [97]:

$$Q(\mathbf{r}) = e\delta(\rho) \frac{e^{-|z|/r_0}}{2r_0}, \tag{3.27}$$

which satisfies

$$\int Q(\mathbf{r}) d^3\mathbf{r} = e. \tag{3.28}$$

Consequently, the effect of the 2D dielectric screening can be visualized as follows: Two electrons living in a 2D dielectric plane interact as two thin charged rods of the length $\approx 2r_0$ and the line charge of density $Q(\mathbf{r}) \approx e/r_0$. The length of the rod sets the characteristic scale of the potential. From large distances $\rho >> r_0$ the rod is seen as a point charge with the potential given by the classical Coulomb interaction [97]. Thus, at large distances, the induced polarization is completely inefficient in screening the external field. On the other hand, for $\rho << r_0$ the rod looks like an infinite wire with the line charge density $e/2r_0$ so that the effective potential reduces to equation (3.22). Hence, at small distances, the effect of the induced polarization becomes dominant, and the singularity was replaced by a weaker logarithmic dependence [97].

3.2 2D polarizability

The next parameter appearing in the effective interaction is the 2D polarizability, α_{2D} of the dielectric sheet. This quantity can be extracted from an *ab-initio* calculation.
The problem, however, is to calculate this quantity when most DFT calculations employ periodic boundary conditions. This means that in a DFT calculation what is effectively simulated is an infinite set of parallel planes separated by a distance L by defining a 3D macroscopic polarization

$$P_{3D} = \alpha_{3D} E, \tag{3.29}$$

where α_{3D} is the 3D polarizability and E is the total electric field. Since the system corresponds to N layers separated by distance L, the macroscopic 3D polarization can be calculated as an average over the number of layers of the microscopic 3D polarization[97], *i.e.*,

$$P_{3D} = \frac{1}{NL}\int dz P_{3D}^{\text{mic}}(z), \tag{3.30}$$

For the quantity $P_{3D}^{\text{mic}}(z)$ a one layer average has been done. For this reason, $P_{3D}^{\text{mic}}(z)$ can be expressed in terms of the macroscopic 2D polarization $P_{2D} = \alpha_{2D} E_{\text{loc}}$

$$P_{3D}^{\text{mic}}(z) = \sum_{n=0}^{N} P_{2D}\delta(z - NL), \tag{3.31}$$

where E_{loc} is the local field acting on a single layer. By replacing eq. (3.31) into eq. (3.30) and taking the interlayer distance L to be large so that $E_{\text{loc}} \approx E$

$$P_{3D} = \frac{1}{NL}\int dz \sum_{n=0}^{N} \alpha_{2D} E_{\text{loc}}\delta(z - NL). \tag{3.32}$$

As α_{2D} is independent on the z coordinate:

$$\begin{aligned} P_{3D} &= \frac{1}{NL}\alpha_{2D} E_{\text{loc}} \sum_{n=0}^{N}\int dz\delta(z - NL), \\ P_{3D} &= \frac{\alpha_{2D} E(N+1)}{NL}. \end{aligned} \tag{3.33}$$

Finally, by making the approximation $N+1 \approx N$ and replacing the definition of P_{3D}, we obtain:

$$\begin{aligned} \alpha_{3D} &= \frac{\alpha_{2D}}{L}, \\ \alpha_{2D} &= L\alpha_{3D} = L(\frac{\varepsilon - 1}{4\pi}). \end{aligned} \tag{3.34}$$

Where ε is the macroscopic dielectric constant of the 3D layered system and can be calculated with *ab-initio* methods [97]. In practice, as we can not take $L \to \infty$, one performs

calculations for several sufficiently large values of L to ensure a good fit.

3.3 Effective masses

When constructing the Schrodinger equation it is necessary to have the masses of the particles involved and the potential. The later was already constructed in the previous chapter, however, for the deduction of electron and the hole masses participating in the exciton formation, we need to remember some basic concepts about the bandstructure of the system.

The bandstructure can be seen as a collection of Bloch wave functions [98], *i.e.*,

$$\Phi(\mathbf{r}) = \sum_k u_k e^{i\mathbf{k}.\mathbf{r}}. \tag{3.35}$$

This wave function can be written on a basis of plane waves, so the idea of group velocity appears [I]

$$v = \frac{1}{\hbar}\frac{dE}{dk}. \tag{3.36}$$

Let an external force f be applied to a band electron, the force will do work in the time interval δt

$$\delta E = f v \delta t. \tag{3.37}$$

In addition,

$$\delta E = \frac{dE}{dk}\delta k = \hbar v \delta k. \tag{3.38}$$

By equating (3.37) and (3.38), and, using $\delta t \to 0$, the derivative appears

$$f = \mathrm{Lim}_{\delta t \to 0}\hbar\frac{\delta k}{\delta t} = \hbar\frac{dk}{dt}. \tag{3.39}$$

Equation (3.39) shows that in a crystal, $\hbar\dfrac{dk}{dt}$ is equal to the external force on the electron. The rate of change of velocity with time is

$$\frac{dv}{dt} = \frac{1}{\hbar}\frac{d^2E}{dkdt} = \frac{1}{\hbar}\frac{d^2E}{dk^2}\frac{dk}{dt}, \tag{3.40}$$

and by substituting the external force on the right hand, we obtain:

$$\frac{\hbar^2}{\dfrac{d^2E}{dk^2}}\frac{dv}{dt} = m^*\frac{dv}{dt} = f, \tag{3.41}$$

[I] This derivation is done for one dimension but the generalization is straightforward.

where Newton equation of $f = ma$ has been used. The effective mass of the system is then

$$m^* = \frac{\hbar^2}{\frac{d^2E}{dk^2}}. \tag{3.42}$$

Since the effective mass depends on energy, an approximation of it is necessary around specific k_0 point. first, lets remark again that the typical optical transitions occurs around the conduction band minimum and valence band maximum respectively as is showed in the figure (3.2) for a direct gap.

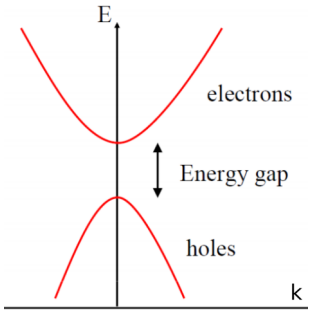

Figure 3.2: Common direct gap of semiconductor.

A particle, in general, can be treated as it were free around the small neighborhood of a specific k_0 point but with an effective mass, *i.e.*, the energy dispersion will be approximately quadratic

$$E(\mathbf{k}) \approx E_0 + \frac{\hbar^2}{2m^*}(\mathbf{k}-\mathbf{k}_0)^2, \tag{3.43}$$

where E_0 and $\mathbf{k}_0$ define the point of the band where the calculation is performed. Following this idea we are able to say that an electron should have a positive effective mass (since its parabola points upwards) and a hole must have a negative effective mass (downwards parabola) [98]. In our calculation we first obtain a bandstructure from some high level theory and subsequently fit a polynomial around the band edges.

3.4 Schrodinger equation

3.4.1 Isotropic case

The hydrogen effective model for excitons is a well known problem in quantum mechanics. It corresponds to a solution of a two dimensional Schrodinger equation for two bodies, where as similar as hydrogen atom, it is possible to transform the system to be at a particle with a reduced mass μ moving at the center of mass [99]. Of course, the center of mass of the

system experiences a central potential $V(r)$. So, the Hamiltonian reads as:

$$H = \frac{-\hbar^2}{2\mu}\left(\frac{\partial^2}{\partial x^2} + \frac{\partial^2}{\partial y^2}\right) + V\left(\frac{r}{r_0}\right), \tag{3.44}$$

where the reduced mass is given by

$$\mu = \frac{m_e M_h}{m_e + M_h}. \tag{3.45}$$

As we have seen in the previous section, the mass of the electron and the hole depend on the direction chosen. The isotropic case thus corresponds to the case in which both masses in directions x and y are equivalent for both the electron and hole [99], *i.e.*,

$$m_e = m_{ex} = m_{ey}, \;\; M_h = M_{hx} = M_{hy}. \tag{3.46}$$

So, the Schrodinger equation reads:

$$-\frac{\hbar^2}{2\mu}\left(\frac{\partial^2}{\partial x^2} + \frac{\partial^2}{\partial y^2} + V\left(\frac{r}{r_0}\right)\right)\Phi(x,y) = E\Phi(x,y). \tag{3.47}$$

By transforming it to polar coordinates:

$$\left[-\frac{\hbar^2}{2\mu}\left(\frac{1}{r}\frac{\partial}{\partial r}\left(r\frac{\partial}{\partial r}\right) + \frac{1}{r^2}\frac{\partial^2}{\partial\theta^2}\right) + V\left(\frac{r}{r_0}\right)\right]\Phi(r,\theta) = E\Phi(r,\theta). \tag{3.48}$$

Since the potential does not depend on θ, it is possible to separate variables, *i.e.*,

$$\Phi(r,\theta) = R(r)\Theta(\theta). \tag{3.49}$$

So, Schrodinger's equation reads:

$$\left[-\frac{\hbar^2}{2\mu}\left(\frac{1}{r}\frac{\partial}{\partial r}\left(r\frac{\partial}{\partial r}\right) + \frac{1}{r^2}\frac{\partial^2}{\partial\theta^2}\right) + V\left(\frac{r}{r_0}\right)\right]R(r)\Theta(\theta) = ER(r)\Theta(\theta), \tag{3.50}$$

or, in a better formulation:

$$\left[\underbrace{-\left(\frac{\partial^2 R(r)}{\partial r^2} + \frac{1}{r}\frac{\partial R(r)}{\partial r} - \frac{2\mu}{\hbar^2}\left(V\left(\frac{r}{r_0}\right) - E\right)R(r)\right)}_{k(r)} - \frac{R(r)}{r^2}\frac{\partial^2}{\partial\phi^2}\right]\Theta(\theta) = 0, \tag{3.51}$$

thus, forming an equation dependent on $\Theta(\theta)$:

$$\frac{\partial^2\Theta(\theta)}{\partial\theta^2} = -\frac{r^2 k(r)}{R(r)}\Theta(\theta). \tag{3.52}$$

Since the left hand side of the equation does not depend on r, the term $r^2k(r)/R(r)$ must be a constant a. So, the solution of (3.52) has an exponential form, *i.e.*,

$$\Theta(\theta) = \frac{1}{\sqrt{2\pi}} e^{i\sqrt{a}\theta}. \tag{3.53}$$

For the boundary condition $\Theta(0) = \Theta(2\pi)$, a is discrete:

$$\sqrt{a} = l, \;\; l \in \mathbb{Z}, \tag{3.54}$$

where l corresponds to the angular momentum quantum number and is an eigenvalue of the angular momentum operator L_z:

$$L_z\Theta(\theta) = -il\hbar\Theta(\theta). \tag{3.55}$$

The radial part of the Schrodinger equation in terms of the quantum number l is given by

$$\begin{aligned} -\left(\frac{\partial^2 R(r)}{\partial r^2} + \frac{1}{r}\frac{\partial R(r)}{\partial r} - \frac{2\mu}{\hbar^2}\left(V\left(\frac{r}{r_0}\right) - E\right)R(r)\right) + l^2\frac{R(r)}{r^2} = 0, \\ -\frac{\partial^2 R(r)}{\partial r^2} - \frac{1}{r}\frac{\partial R(r)}{\partial r} + \frac{2\mu}{\hbar^2}\left(V\left(\frac{r}{r_0}\right) - E\right)R(r) + \left(\frac{l^2}{r^2}\right)R(r) = 0. \end{aligned} \tag{3.56}$$

From here, it is possible to solve the Schrodinger equation as usual with the transformation $R(r) = u(r)/\sqrt{r}$ leading to an equation for the radial part of the form:

$$-\frac{\partial^2 u(r)}{\partial r^2}\left[2\frac{\mu}{\hbar^2}\left(V\left(\frac{r}{r_0}\right) - E\right) - \frac{(\frac{1}{4} - l^2)}{r^2}\right]u(r) = 0. \tag{3.57}$$

However, for solving this problem numerically, it is necessary to avoid the singularity at $r = 0$. This can be achieved by making a variable transformation of the form [96, 99]:

$$\begin{aligned} t = \ln\left(\frac{r}{r_0}\right) \;\rightarrow\; r = r_0 e^t, \\ \frac{dt}{dr} = \frac{1}{r} \;\rightarrow\; r\frac{d}{dr} = \frac{d}{dt}. \end{aligned} \tag{3.58}$$

So, the first two terms in equation (3.56) read

$$-\frac{\partial^2 R(r)}{\partial r^2} - \frac{1}{r}\frac{\partial R(r)}{\partial r} = \frac{1}{r}\frac{\partial}{\partial r}\left(r\frac{\partial}{\partial r}R(r)\right) = \frac{1}{r^2}\frac{\partial}{\partial t}\left(\frac{\partial}{\partial t}R(r(t))\right) = \frac{e^{-2t}}{r_0^2}\frac{\partial^2 R(t)}{\partial t^2}. \tag{3.59}$$

In that sense, equation (3.56) can be rewritten as:

$$-\frac{\partial^2 R(t)}{\partial t^2} + \left[\frac{2\mu r_0}{\hbar^2}(V(t) - E)e^{2t} + l^2\right]R(t) = 0. \tag{3.60}$$

The transformation from r to t was also made in order to obtain an equation of the form

$$R''(t) - M(t,E)R(t) = 0, \tag{3.61}$$

which can be solved by the so-called Numerov method [96, 99, 100] which will be presented in section 3.5.

3.4.2 Anisotropic case

When the effective masses of electron and hole are different in each direction:

$$m_{ex} \neq m_{ey}, \;\; M_{hx} \neq M_{hy}, \tag{3.62}$$

the anisotropy of the system can not be ignored, and must be introduced in the Hamiltonian [96, 99], *i.e.*,

$$H = -\frac{\hbar^2}{2\mu_x}\frac{\partial^2}{\partial x^2} - \frac{\hbar^2}{2\mu_y}\frac{\partial^2}{\partial y^2} + V\left(\frac{r}{r_0}\right). \tag{3.63}$$

Where the reduced masses are direction dependent:

$$\mu_x = \frac{m_{ex}M_{hx}}{m_{ex}+M_{hx}}, \;\; \mu_y = \frac{m_{ey}M_{hy}}{m_{ey}+M_{hy}}. \tag{3.64}$$

This Hamiltonian can be thought as a 4 particle problem, where two excitons (two e^- and two h^+) move in x and y direction. So, in this case our problem can be reduced to two particles with reduced masses μ_x and μ_y moving around two different centers of mass. However in order to achieve a unique center of mass, it is necessary to match both particles in a single reduced mass [96, 99], *i.e.*,

$$\mu = \frac{\mu_x\mu_y}{\mu_x+\mu_y}, \tag{3.65}$$

and the coordinates transform to the new frame as:

$$\sqrt{\frac{\mu_x}{2\mu}}x = x', \;\; \sqrt{\frac{\mu_y}{2\mu}}y = y'. \tag{3.66}$$

Thus,

$$x' = r'\cos\theta, \;\; y' = r'\sin\theta, \;\; r' = \sqrt{x'^2+y'^2}, \tan\theta = \frac{y'}{x'}. \tag{3.67}$$

So, the derivatives in the Hamiltonian transform as:

$$\begin{aligned} -\frac{\hbar^2}{2\mu_x}\frac{\partial^2}{\partial x^2} - \frac{\hbar^2}{2\mu_y}\frac{\partial^2}{\partial y^2} &= -\frac{\hbar^2}{2\mu_x}\frac{\partial^2}{\partial x'^2}\left(\frac{\partial x'}{\partial x}\right)^2 - \frac{\hbar^2}{2\mu_y}\frac{\partial^2}{\partial y'^2}\left(\frac{\partial y'}{\partial y}\right)^2, \\ &= -\frac{\hbar^2}{4\mu}\left(\frac{\partial^2}{\partial x'^2}+\frac{\partial^2}{\partial y'^2}\right). \end{aligned} \tag{3.68}$$

In addition, the central potential in terms of the distance r between the two particles of reduced mass μ_x and μ_y change to the prime coordinate system [96, 99]:

$$\begin{aligned}
r &= \sqrt{x^2+y^2} = \sqrt{\frac{2\mu}{\mu_x}x'^2 + \frac{2\mu}{\mu_y}y'^2} = \sqrt{\frac{2\mu}{\mu_x}r'^2\cos^2\theta + \frac{2\mu}{\mu_y}r'^2\sin^2\theta},\\
&= r'\sqrt{\frac{2}{\mu_x+\mu_y}}\sqrt{\mu_y\cos^2\theta + \mu_x\sin^2\theta} = r'\sqrt{\frac{2}{\mu_x+\mu_y}}\sqrt{\mu_y\cos^2\theta + \mu_x\sin^2\theta \pm \mu_y\sin^2\theta},\\
&= r'\sqrt{\frac{2}{\mu_x+\mu_y}}\sqrt{\mu_y + (\mu_x-\mu_y)\sin^2\theta} = r'\sqrt{\frac{2}{\mu_x+\mu_y}}\sqrt{\mu_y + (\mu_x-\mu_y)(\frac{1-\cos2\theta}{2})},\\
&= r'\sqrt{\frac{2}{\mu_x+\mu_y}}\sqrt{\frac{\mu_x+\mu_y}{2} + (\mu_y-\mu_x)(\frac{\cos2\theta}{2})}\\
&= r'\sqrt{1+\frac{\mu_y-\mu_x}{\mu_x+\mu_y}\cos2\theta}.
\end{aligned} \tag{3.69}$$

If the quantity $\beta = (\mu_y-\mu_x)/(\mu_x+\mu_y)$ is defined to be positive for all $\mu_y > \mu_x$, the potential will read as:

$$V\left(\frac{r}{r_0}\right) \rightarrow V\left(\frac{r'}{r_0}\sqrt{1+\beta\cos2\theta}\right). \tag{3.70}$$

Finally the hamiltonian takes the form:

$$H = \frac{-\hbar^2}{4\mu}\left(\frac{\partial^2}{\partial x'^2} + \frac{\partial^2}{\partial y'^2}\right) + V\left(\frac{r'}{r_0}\sqrt{1+\beta\cos2\theta}\right), \tag{3.71}$$

and, in polar coordinates:

$$H = \frac{-\hbar^2}{4\mu}\left(\frac{1}{r'}\left(\frac{d}{dr'}\left(r'\frac{d}{dr'}\right)\right) + \frac{1}{r'^2}\left(\frac{d^2}{d\theta^2}\right)\right) + V\left(\frac{r'}{r_0}\sqrt{1+\beta\cos2\theta}\right). \tag{3.72}$$

Since a numerical approach is needed, it is convenient to use again the transformation (3.58) to avoid the singularity [96, 99]. So, the Hamiltonian is expressed in terms of t:

$$H = \frac{-\hbar^2}{4\mu r_0^2}\left[e^{-2t}\left(\partial_t^2 + \partial_\theta^2\right)\right] + V\left(e^t\sqrt{1+\beta\cos2\theta}\right). \tag{3.73}$$

The Schrodinger equation is finally given by

$$\frac{-\hbar^2}{4\mu r_0^2}\left[e^{-2t}\left(\partial_t^2 + \partial_\theta^2\right)\right] + V\left(e^t\sqrt{1+\beta\cos2\theta}\right)\Phi(t,\theta) = E\Phi(t,\theta). \tag{3.74}$$

Even though the potential depends on both coordinates and does not allow us to express a solution as equation (3.53) for the angular part, it is still possible to establish a solution in

terms of a Fourier series,

$$\Phi(t,\theta) = \sum_l \frac{1}{\sqrt{2^{\delta_{l0}}\pi}} \left[f_l(t)\cos(l\theta) + g_l(t)\sin(l\theta) \right]. \tag{3.75}$$

This solution together with the angular dependence on the potential ($\cos 2\theta$) allow to couple sines exclusively with sines and cosines to cosines. Moreover, even and odd angular momentum coefficients do not mix, *i.e.*, even l's will only couple with even l's and the same for odd values [99]. This suggest that $\Phi(t,\theta)$ can be expressed in a simpler form:

$$\Phi^{\pm}(t,\theta) = \sum_l \frac{1}{\sqrt{2^{\delta_{l0}}\pi}} h_l \mathrm{trig}^{\pm}(l\theta), \tag{3.76}$$

where l runs over the appropiate harmonic numbers and $\mathrm{trig}^{\pm}$ is either cosine or sine respectively [99]. Equation (3.76) reflects more clearly the separation of variables, consequently, the second order derivate in θ is:

$$e^{-2t}\partial_\theta^2 \Phi(t,\theta) = -l^2 e^{-2t}\Phi(t,\theta). \tag{3.77}$$

The Schrodinger equation now reads:

$$-\sum_{l=0}^{\infty}\left(\frac{\hbar^2}{4\mu r_0^2}\left[e^{-2t}\left(\partial_t^2 - l^2\right)\right] - V\left(e^t\sqrt{1+\beta\cos 2\theta}\right)\right)\frac{1}{\sqrt{2^{\delta_{l0}}\pi}} h_l \mathrm{trig}^{\pm}(l\theta) = E\sum_{l=0}^{\infty}\frac{1}{\sqrt{2^{\delta_{l0}}\pi}} h_l \mathrm{trig}^{\pm}(l\theta). \tag{3.78}$$

If this equation is multiplied by $\mathrm{trig}^{\pm}(n\theta)$ and integrated over θ [99], the values $h_l(t)$ will correspond to the orthogonality result of the integral:

$$h_n(t) = \sum_l \int \frac{1}{\sqrt{2^{\delta_{l0}}\pi}} d\theta\, h_l(t)\mathrm{trig}^{\pm}(l\theta)\mathrm{trig}^{\pm}(n\theta). \tag{3.79}$$

Where the kinetic term in the Schrodinger equation is:

$$-\sum_l \frac{\hbar^2}{4\mu r_0^2}\left[e^{-2t}\left(\partial_t^2 - l^2\right)\right]\int d\phi \frac{1}{\sqrt{2^{\delta_{l0}}\pi}} h_l(t)\mathrm{trig}^{\pm}(l\theta)\mathrm{trig}^{\pm}(n\theta) = \frac{\hbar^2}{4\mu r_0^2}\left[e^{-2t}\left(\partial_t^2 - n^2\right)\right] h_n(t), \tag{3.80}$$

the energy is simply

$$E\sum_l \int d\theta \frac{1}{\sqrt{2^{\delta_{l0}}\pi}} h_l(t)\mathrm{trig}^{\pm}(l\theta)\mathrm{trig}^{\pm}(n\theta) = E h_n(t), \tag{3.81}$$

with the potential

$$\sum_l \int d\theta\, V\left(e^t\sqrt{1+\beta\cos 2\theta}\right)\frac{1}{\sqrt{2^{\delta_{l0}}\pi}} \mathrm{trig}^{\pm}(l\theta)\mathrm{trig}^{\pm}(n\theta) h_l(t) = \sum_l V_{nl} h_l(t), \tag{3.82}$$

where:

$$V_{nl} = \int d\theta \frac{1}{\sqrt{2^{\delta_{l0}}\pi}} V\left(e^t\sqrt{1+\beta\cos 2\theta}\right)\mathrm{trig}^{\pm}(l\theta)\mathrm{trig}^{\pm}(n\theta). \tag{3.83}$$

Gathering terms, the Schrodinger equation becomes

$$\frac{-\hbar^2}{4\mu r_0^2} e^{-2t}\left(\partial_t^2 - n^2\right) h_n(t) - \sum_l V_{nl} h_l(t) = E h_n(t), \tag{3.84}$$

which can be expressed in a more suitable form to apply the Numerov method. This is achieved if a vector function is defined as,

$$\mathbf{f}(t) = \left[f_{n_0}(t), f_{n_0+2}(t), ..., f_{n_0-2+2N}(t), f_{n_0+2N}(t)\right], \tag{3.85}$$

where each entry corresponds to an angular momentum, resulting in $N+1$ terms due to the end of the sum on $n_0 - 2 + 2N$. So, n_0 can be $n_0 = 0$ which corresponds to even n cosine-like functions; $n_0 = 1$ is used for cosine- and sine-like functions; and $n_0 = 2$ is necessary for even n sine-like functions due to the fact that $n_0 = 0$ results in vanishing sine-like terms [99]. In addition, the terms n^2 and E are multipĺied by the identity $\mathbf{I}$ in order to obtain a matrix formulation of equation (3.84), *i.e.*,

$$\mathbf{f}''(t) = \mathbf{M}(t)\mathbf{f}(t),\ \mathbf{M}(t) = \mathbf{n}^2 - be^{2t}(\mathbf{V} - \mathbf{E}), \tag{3.86}$$

where the constant b represents:

$$\frac{-4\mu r_0^2}{\hbar^2}. \tag{3.87}$$

The form of equation (3.86) is again exactly what is required for the Numerov method (now in matrix form).

3.5 Numerical approach

Looking at the functional form of Schrodinger equation for isotropic and anisotropic cases we notice that it has the form of a second order linear eigenvalue problem. A numerical solution can thus be obtained via the so-called Numerov method. In this section we explain the Numerov method from its origins to later give the initial ansatz to solve equations (3.61) and (3.86).

3.5.1 Numerov method

The Numerov method, was designed to numerically solve Ordinary differential equations (ODEs) of the form:

$$\frac{d^2y}{dx^2} + k(x)\,y(x) = 0, \tag{3.88}$$

in which $k(x)$ can be any function. note that this ODE corresponds to the time independent Schrodinger equation. Even though the Rugen-Kutta algorithm already exist to solve EDO's, the Numerov method is an order more accurate and can be applied to ODEs without the first order derivate [100]. For solving equation (3.88), first let an operator $1+\frac{h^2}{12}\frac{d^2}{dx^2}$ act on it, *i.e.*,

$$\left[1+\frac{h}{12}\frac{d^2}{dx^2}\right]\left(\frac{d^2y}{dx^2}+k^2(x)y(x)\right)=0,$$
$$\frac{h'^2}{12}\frac{d^4y}{dx^4}+\frac{h^2}{12}\frac{d^2}{dx^2}\left[k(x)y(x)\right]+\frac{d^2y}{dx^2}+k(x)y(x)=0. \tag{3.89}$$

To get rid of the 2nd and fourth order derivatives on y, lets write the Taylor series for y centered around $x+h$ where h is small [100]:

$$y(x+h)=y(x)+hy'(x)+\frac{h^2}{2!}y''(x)+\frac{h^3}{3!}y'''(x)+\frac{h^4}{4!}y''''(x)+\ ... \tag{3.90}$$

and expand $y(x)$ for $x-h$ as well, *i.e.*,

$$y(x-h)=y(x)-hy'(x)+\frac{h^2}{2!}y''(x)-\frac{h^3}{3!}y'''(x)+\frac{h^4}{4!}y''''(x)+\ ...\ . \tag{3.91}$$

If we add these equations and solve for $y''(x)$ (considering all odd powers of h vanish)

$$y''(x)=\frac{y(x+h)-2y(x)+y(x-h)}{h^2}-\frac{h^2}{12}y''''(x)+O(h^6). \tag{3.92}$$

Plugging this equation back into (3.89), the 4th order derivatives also vanish

$$\frac{h^2}{12}\frac{d^2}{dx^2}\left[k(x)y(x)\right]+\frac{y(x+h)-2y(x)+y(x-h)}{h^2}+k(x)y(x)=0. \tag{3.93}$$

And the 2nd derivative of $k(x)y(x)$ can also be Taylor expanded,

$$\frac{d^2\left[k(x)y(x)\right]}{dx^2}\approx\frac{\left[k(x+h)y(x+h)-k(x)y(x)\right]+\left[k(x-h)y(x-h)-k(x)y(x)\right]}{h^2}. \tag{3.94}$$

By replacing it on to eq. (3.93), and rearranging the terms yields the Numerov algorithm [100]:

$$y(x+h)=\frac{2\left[1-\frac{5}{12}h^2k(x)\right]y(x)-\left[1+\frac{h^2}{12}k(x-h)\right]y(x-h)}{1+\frac{h^2}{12}k(x+h)}, \tag{3.95}$$

If the x variable is discrete, $x = jh$, then

$$y_{j+1} = \frac{2\left[1 - \frac{5}{12}h^2 k_j\right] y_j - \left[1 + \frac{h^2}{12}k_{j-1}\right] y_{j-1}}{1 + \frac{h^2}{12}k_{j+1}}. \tag{3.96}$$

By defining $P_j = 1 + \frac{h^2}{12}k_j$, equation (3.96) reads as

$$y_{j+1} = P_{j+1}^{-1}\left[(12 - 10P_j)y_j - P_{j-1}y_{j-1}\right]. \tag{3.97}$$

This equation gives the power to find y_j when the values y_{j-1} and y_{j-2} are known. This means, of course, that we need to know the values of y_0 and y_1 and go forward along the lattice, or, know the values of y_{N-1} and y_{N-2} and go backwards through the lattice. The two boundary conditions are expected since we are treating with a 2nd order ODE, and can be obtained by considering the physical system at hand [100].

3.5.2 Solution of Isotropic case

Equation (3.61) can be discretized $t \to t_i$,

$$f''(t_i) = M(t_i, E) f(t_i). \tag{3.98}$$

So, it can be solved by the Numerov method for variable t_i if the initial conditions are determined (Numerov equations are the same but with $k(t) = -M(t)$). In addition, we need to solve equation (3.98) for a particular value of E. So, if different values of E are tested, we need to search the point in which the function f and its derivate $f^{'}$ are continuous (this comes from the fact that wave function must be continuous), *i.e.*, propagate the solution from both extremes ($f(t_1)$,$f(t_2)$ for the initial and $f(t_{N-1})$,$f(t_N)$ for the final) and find the middle point t_m which satisfies

$$\left(f^L(t_m) - f^R(t_m)\right) + \left(f'^L(t_m) - f'^R(t_m)\right) = 0. \tag{3.99}$$

If condition (3.99) is satisfied, then the energy chosen for that propagation is an eigenvalue of the Schrodinger equation.

In the case of the isotropic system, the initial conditions can be inferred from the asymptotic behaviour of equation (3.60). In the case where $r \to 0$ or $t \to -\infty$, equation (3.60) reduces to

$$-\frac{\partial^2 R(t)}{\partial t^2} + l^2 R(t) = 0, \tag{3.100}$$

which has a solution of:

$$R(t) = e^{lt}. \tag{3.101}$$

Thus, our initial values $f(t_1) = R(t_1)$, $f(t_2) = R(t_2)$ for $l = 0$ are [99]:

$$R(t_1) = 1 - 2t_1,\ R(t_2) = 1 - 2t_2, \tag{3.102}$$

and, for $l \neq 0$, those are,

$$R(t_1) = 0,\ R(t_2) = dt. \tag{3.103}$$

On the other hand, when $r \to \infty$ or $t \to \infty$, the wavefunction must vanish towards the infinity, thus, we can choose:

$$R(t_N) = 0,\ R(t_{N-1}) = dt. \tag{3.104}$$

3.5.3 Solution of the Anisotropic case

A generalization of the Numerov method is necessary in order to solve (3.86). In this case it corresponds to a matrix Numerov method. The method is essentially the same, but Numerov equations for propagation now are matrices and vectors [96], *i.e.*,

$$\begin{aligned} \mathbf{P}_j &= 1 + \frac{h^2}{12}\mathbf{k}_j \\ \mathbf{f}_{j+1} &= \mathbf{P}_{j+1}^{-1}\left[(12 - 10\mathbf{P}_j)\mathbf{f}_j - \mathbf{P}_{j-1}\mathbf{f}_{j-1}\right], \end{aligned} \tag{3.105}$$

where in comparison to equation (3.86), the value of $\mathbf{k}_j = -\mathbf{M}_j$ is a matrix and $\mathbf{f}_j$ is a vector. As similar to the isotropic case, it is necessary to settle the values of initial conditions for the vectors $\mathbf{f}(t_1)$, $\mathbf{f}(t_2)$, $\mathbf{f}(t_{N-1})$ and $\mathbf{f}(t_N)$ and then start the propagation forward and backwards respectively for each energy. When an energy is a solution of the Schrodinger equation, *i.e.*, is an eigenvalue of the system, both propagations from the right (backwards) and left (upwards) must meet at an arbitrary point t_m and satisfy the relation

$$\sum_l \mathbf{f}^{l,R}(t_m) = \sum_l \mathbf{f}^{l,L}(t_m),\ \sum_l \mathbf{f'}^{l,R}(t_m) = \sum_l \mathbf{f'}^{l,L}(t_m), \tag{3.106}$$

or in determinant form:

$$\det\begin{pmatrix} \mathbf{f}^{1,R}(t_m) & \mathbf{f}^{2,R}(t_m) & \dots & \mathbf{f}^{N,R}(t_m) & \mathbf{f}^{1,L}(t_m) & \mathbf{f}^{2,L}(t_m) & \dots & \mathbf{f}^{N,L}(t_m) \\ \mathbf{f'}^{1,R}(t_m) & \mathbf{f'}^{2,R}(t_m) & \dots & \mathbf{f'}^{N,R}(t_m) & \mathbf{f'}^{1,L}(t_m) & \mathbf{f'}^{2,L}(t_m) & \dots & \mathbf{f'}^{N,L}(t_m) \end{pmatrix} = 0. \tag{3.107}$$

This equation ensures the continuity of the wavefunction. For the initial conditions we apply the same analysis as for the isotropic case, at $r \to 0$, equation (3.101) is still valid, but in this case the degeneracy of vector $\mathbf{f}$ must be accounted for

$$\mathbf{f}^n(t_1) = e^{l t_1}\delta_{nl},\ \mathbf{f}^n(t_2) = e^{l t_2}\delta_{nl}. \tag{3.108}$$

But, since $t \to -\infty$ we arrive at the same conclusion for the isotropic case, *i.e.*, for $l = 0$:

$$\mathbf{f}^n(t_1) = 1 - 2t_1,\ \mathbf{f}^n(t_2) = 1 - 2t_2, \tag{3.109}$$

and, for any other value of l,

$$\mathbf{f}^n(t_1) = 0,\ \mathbf{f}^n(t_2) = dt. \tag{3.110}$$

On the other hand, the wave function must vanish at infinity, thus implying

$$\mathbf{f}^n(t_N) = 0,\ \mathbf{f}^n(t_{N-1}) = dt, \tag{3.111}$$

for any l. Having set the initial conditions for the Numerov method, we are now able to determinate the correct eigenvalues of the exciton for a two dimensional material.

CHAPTER 4

Tellurene

Having described a general methodology for calculating the electronic and optical properties, we turn to the topic of this dissertation by describing the different properties of Bulk-Te and tellurene allotropes. The results where achieved by using Quantum Espresso with a PBE pseudopotential for calculating: structural properties, band structure, density of states and phonons calculations; and Yambo for calculating: quasiparticle corrections (GW), GW-RPA and GW-BSE, in order to estimate the presence of excitons. Lastly, the Numerov method develop in Chapter 3 was computed using MATLAB for estimate the exciton binding energies and the wave-functions. The results will be compared with previous on the literature and will lead us to interesting conclusions.

4.1 Computational Details

The DFT calculations were performed using Quantum Espresso, where we have converged the following parameters: *ecutwfc* = 90 Ry, *ecutrho* = 450 Ry, *k-points* = $40x40x1$ (for monolayer), *k-points* = $15x15x15$ (for isolated tellurium) and *k-points* = $25x25x25$ (for bulk). Also, in the case of monolayers, the vacuum used in the unitary cells was 31 Å, and, for bulk, we turn on the Van der Waals (vdW) force trough the variable *vdw-corr* where the Tkatchenko-Scheffler (*ts-vdw*) dispersion correction was used. For GW calculation we have performed firstly a non self consistent calculation (using Quantum Espresso) with a number of bands, in the case of α-Te, of *nbnd* = 350 and a mesh of *k-points* = $30x30x1$; while for β-Te, the converged values were *nbnd* = 580 and *k-points* = $23x23x1$. After the non-self consistent calculation, the GW approximation was performed using Yambo with the following converged parameters: the Coulomb potential truncation (*rim-cut*, *CutGeo* = 18Å); the exchange energy components was *ExxRLvcs=26 Ry*, for α-Te, and *ExxRLvcs* = 16 Ry, for β-Te; the polarization function bands (*BndsRnXp*) used in the dynamical dielectric constant has the same value as *nbnd*; the response function block size of the dynamical screening (*NGsBlkXp*) was 6 Ry, for both cases; the number of bands enter in the GW calculation (*GBndRnge*) were 280, for α-Te, and 250, for β-Te; the number of k-points in the QP (quasiparticle) correction (*QPkrange*) were 452 , for α-Te, and 265, for β-Te; lastly the band indices entering in the calculation were 20-30 (11 bands), for α-Te, and 22-30 (9 bands), for β-Te.

The absorption spectras were performed using Yambo. In the case of IPA the converged parameters were the response block size of the KS polarization *NGsBlkXd* = 4 Ry and a number of polarization function bands of *BndsRnXd* = 100 for both α-Te and β-Te phases. The GW-RPA and GW-BSE were obtained using the Coulomb potential truncation (*rim-cut*), the diagonalization solver (*BSSmod* = *d*), the QP corrections and the GW converged parameters (*BSEBands* = $20-30$ for α-Te, and *BSEBands* = $22-30$ for β-Te). Furthermore, the double-grid were performed using the static screening from the BSE calculation in a grid of *k-points* = 4001 (for α-Te) and *k-points* = 6001 (for β-Te). In what respect to the BSE calculation for the β-Te with spin orbit coupling, we performed a rigid shift trough the scissor

operator (*KfnQP-E*) of 1.03 eV and used almost the same parameters as in the non-SOC case but with larger number of bands $nbnd = BndsRnXs = 580$ and band indices in the range of $43-54$ (12 bands).

4.2 Structural and Electronic Properties

Tellurium atoms arrange in an unique semiconductor bulk form which can be exfoliated in the z^{th} direction (see figure 4.1-a) to form β-phase or pass through a thickness-dependent structural phase transition to built the α-phase. Furthermore, it has an unique 2D conducting material, γ-phase, who lacks 3D counterpart.

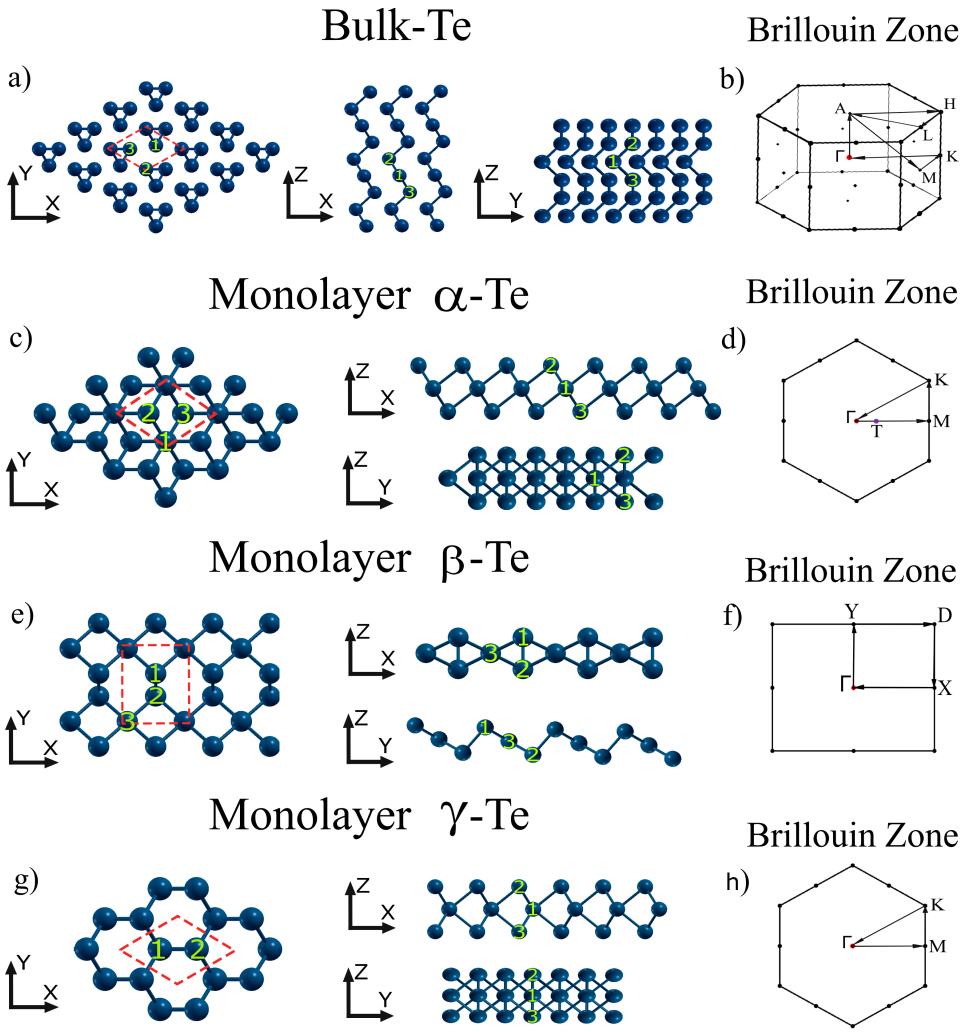

Figure 4.1: Tellurium optimized structures from different sides xy, zx and zy for a) bulk phase, c) α-Te, e) β-Te and g) γ-Te allotropes. In addition, the unitary cell is detailed for each phase with atoms labeled by numbers. Furthermore, the first Brillouin zone for each phase and the path taken for the band structure is detailed in b,d,f and h.

4.2.1 Bulk-Te

	a(Å)	b(Å)	c(Å)	d(Å)	d_z(Å)	$E_C(eV/atom)$
Te-Bulk	4.45	4.45	5.96	2.90	3.97	-3.10
Previous Results	4.46 [101] 4.47 [58] 4.46 [102]	4.46 [101] 4.47 [58] 4.46 [102]	5.93 [101] 5.90 [58] 5.92 [102]	2.90 [53]	-	-2.79 [53]

Table 4.1: Structural parameters, lattice constants and electronic properties for bulk-Te (α-Te, β-Te and γ-Te) such as bond length d, separation from top and bottom layers of atoms d_z(Å) and cohesive energy E_C

The optimized structure of bulk tellurium is presented in figure 4.1-a. The main characteristic of bulk lie in its construction, formed by arrays of Te chains which are stacked together via vdW interactions [53]. Those chains seen from the top form triangular arrangements that covers the xy plane. Using DFT calculations, the lattice constants of the relaxed structures were obtained with a=4.45 Å, b=4.45 Å and c=5.96 Å which are in excellent agreement with available results [53, 58, 103, 101, 102] as shown in table 4.1. In addition, the coordination number (n_c) of atoms labeled as 1, 2 and 3 (see figure 4.1-a) are two with a bond length corresponding to 2.90 Å. Furthermore, the z^{th} length, which is the separation between the upper (atom 2) and lower (atom 3) atoms, in an unit cell, is 3.97 Å as is presented in table 4.1. Lastly, the cohesive energy with respect to isolated tellurium is -3.10 eV.

4.2.2 Monolayer-Te

	a(Å)	b(Å)	d(Å)	d_z(Å)	$E_C(eV/atom)$	$E_L(eV/layer)$
α-Te	4.18	4.18	3.04	3.65	-3.15	-0.14
Prev. Res.	4.15 [53]	4.15 [53]	3.02 [53]	3.67 [53]	-2.62	-
β-Te	4.17	5.49	2.77	2.18	-3.17	-0.21
Prev. Res.	4.17 [53, 103] 4.20 [58]	5.49 [53, 103] 5.60 [58]	2.77 2.75 [53]	2.18 2.16 [53]	-3.17 -2.56	-0.21 -
γ-Te	4.02	4.02	3.09	4.05	-2.96	-0.43
Prev. Res.	3.92 [53]	3.92 [53]	3.08 [53]	4.16 [53]	-2.46	-

Table 4.2: Structural parameters, lattice constants and electronic properties for monolayer-Te (α-Te, β-Te and γ-Te) such as bond length d, separation from top and bottom layers of atoms d_z(Å), cohesive energy E_C and layer energy E_L

The relaxed structures of the different phases of monolayer-Te, tellurene, are shown in figure 4.1. The α-Te corresponds to 4.1-b, the β-Te phase is in 4.1-c and γ-Te is presented in 4.1-d. α-Te is formed via a mechanism of thickness-dependent phase transition (see appendix B). It has an hexagonal structure like $1T - MoS_2$ with lattice parameters a=b=4.18 Å (see table 4.3), where the upper and lower atom labeled as 2 and 3 have coordination number

$n_c = 3$, and the central atom (Mo in the comparison with $1T - MoS_2$) has $n_c = 6$. The bond length is 2.77 Å and the interlayer distance is 3.65 Å. The cohesive energy in comparison with isolated tellurium is 3.15 $eV/atom$ and the layer coupling energy in comparison with bulk-Te is 0.14 $eV/layer$ (see table 4.3).

On the other hand, β-Te is the natural monolayer phase emerging from bulk Te, nano sheets of β phase can be obtained by exfoliating the Te slab along the z direction (truncating the bulk helical chain structure) and has been successfully synthesized [59, 60, 61]. Orthorombic β-Te has a planar four-membered layer of atoms in the top layer, and has structure constants of a=4.17 Å and b=5.49 Å (see table 4.3). The upper and lower atoms (labeled as 1 and 2) have $n_c = 3$, while the central Te atom has $n_c = 4$. The bond length is 2.77 Å, the interlayer distance 2.18 Å and the layer coupling energy is 0.21 $eV/layer$ (see table 4.3). This phase is the most stable phase due to its cohesive energy of 3.17 $eV/atom$. Lastly, the hexagonal γ-Te has a similar structure to $2H - MoS_2$ with lattice constants of a=b=4.02 Å smaller in comparison with α-Te (see table 4.3). Its bond length has a value of 3.09 Å, the interlayer distance is 4.05 Å, the cohesive energy is the lowest, 2.96 $eV/atom$, and the layer coupling energy is 0.43 $eV/layer$. Thermodinamical analysis were carried by Zhili Zhu et. al, showing that the three phases are stable due to the absence of imaginary frequency phonon modes even at room temperature (see figure 4.2-d,e,f). The total charge density analysis extracted from [53] shows a metal ligand bonding between central and outer atoms for α-Te and γ-Te; a σ-bond between outer atoms and metal ligand bonding for central interaction with outer atoms (see figure 4.2-a,b,c).

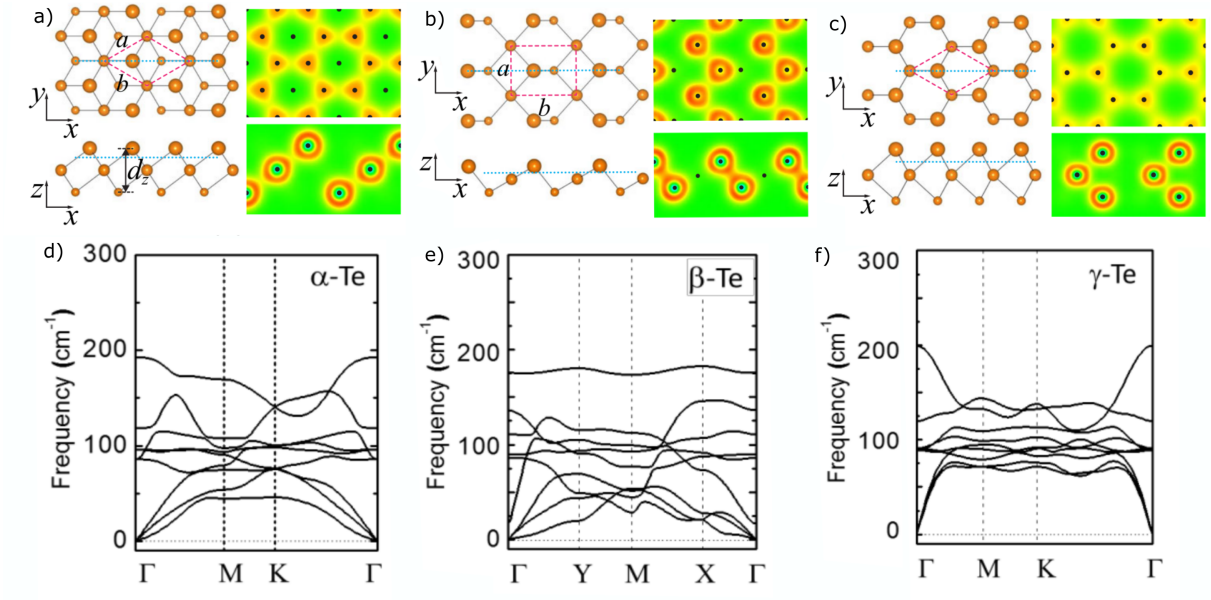

Figure 4.2: Total charge density of (a) α-Te , (b) β-Te and (c) γ-Te. Phonon spectra of (d) α-Te, (e) β-Te and (f) γ-Te extracted from [53, 54]

4.3 Band Structure and Density of States

	$\mathbf{E}_{Dg}^{PBE}(eV)$	$\mathbf{E}_{Ig}^{PBE}(eV)$	$\mathbf{E}_{Dg}^{PBE+SOC}(eV)$	$\mathbf{E}_{Ig}^{PBE+SOC}(eV)$
Bulk-Te	0.19	0.17	-	-
Prev. Res.	0.19 [58]	0.17 [58]	0.03 [58]	-
α-Te	0.90	0.75	0.51	0.39
Prev. Res.	-	0.76 [53]	-	0.46 [53]
β-Te	1.50	1.13	1.04	1.04
Previous Results	1.17 [53]	1.20 [58] 1.45 [58]	1.02 [58]	1.03 [53] 1.02 [58]

Table 4.3: Band structure direct ($\mathbf{E}_{Dg}^{PBE}$) and indirect gaps ($\mathbf{E}_{Ig}^{PBE}$) as well as SOC inclusion ($\mathbf{E}_{Dg}^{PBE+SOC}$, $\mathbf{E}_{Ig}^{PBE+SOC}$) for Bulk-Te and monolayer-Te phases: α-Te and β-Te.

4.3.1 Bulk-Te

The band structure calculated with DFT using a PBE pseudopotential (valence electron contributions arise from $4s^2 4p^6 3d^{10} 5s^2 5p^4$) is shown in figure 4.3, whose high-symmetry points in the brillouin zone are presented in figure 4.1-a, where the 0 corresponds to the Fermi energy E_F. The conduction band minimum (CBM) is located at point H, while the valence band maximum (VBM) is slightly away from the H point. Thus, bulk Te is a nearly direct band gap semiconductor. The indirect gap value is approximately 0.17 eV and the direct band gap is about 0.19 eV at the H point. In addition, the density of states (DOS) shows a predominant contribution in the conduction and valence bands coming from the 5p orbitals, while the 5s has a minor impact, and, deeper orbitals contributions such as 4s, 4p or 3d are negligible. In addition, the projected density of states per atom (see figure 4.3-c,d,e) shows identical orbital distributions (s, p_x, p_y, p_z) for atoms labeled as 1 and 2, behavior expected from the symmetry of the system, while atom 3 has similar s and p_z component, but p_x and p_y are interchange. Furthermore, the contribution around the CBM comes from a mixture of p_x, p_y and p_z orbitals on atom 1 and 2, while on atom 3 the p_y orbital gives a stronger contribution. The same happens on the VBM for atom 1 and 2, but atom 3 overall contribution arises from p_x orbital. On the other hand, the projected density of states on p states (figure 4.3-f) shows an identical distribution for x and y directions, while p_z has an slightly major contribution around the CBM but not at the VBM where p_x and p_y has a stronger presence.

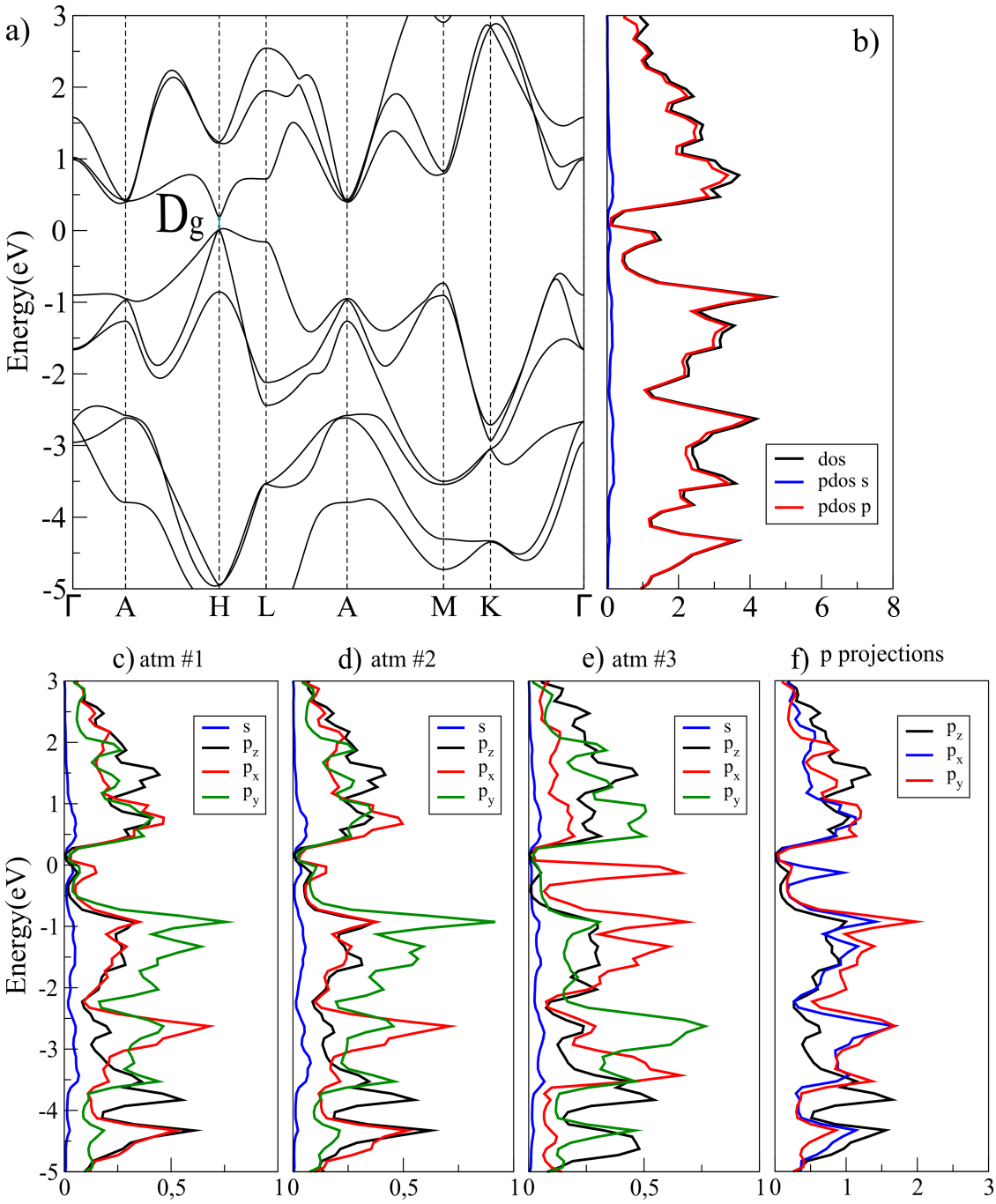

Figure 4.3: (a) Band structure of Bulk-Te, (b) density of states (black lines) as well as the projected density of states for s (p) as blue (red) lines. Projected density of states per (c) atom 1, (d) 2 and (e) 3 , and, (f) per p state projection in each direction.

4.3.2 Monolayer-Te

Tellurene allotropes has hexagonal brillouin zone for α-Te and γ-Te, while a rectangular shape for β-Te (see figure 4.1). The band structure plotted in figures 4.4, 4.5, 4.7 for the non spin orbit coupling (SOC) case; and, 4.6, 4.8 when SOC is including in the calculation. The SOC inclusion has only be done on semiconductor phases, α-Te and β-Te, in order to determine how much the gap will change.

The γ-Te band structure shows a metalic behaviour, that means, no exciton can be formed in this particular phase due to the absence of a gap. Its density of states shows, by a large difference, that almost all contributions around the Fermi level come from p states as similar to α-Te and β-Te (see figure 4.4-a,b). In the case of the projected density of states per atom (figure 4.4-c-e) we can appreciate that the distribution for atom 2 and 3 are the same as we expect from the structure of the system. However, both atoms are asymmetric with respect to atom 1, this is clearly seen in the interval range from -3.5 to -2 eV where the s orbital has the large contribution for from atom 1 meanwhile atoms 2 and 3 are dominated by p orbitals in that energy range. Furthermore, the p_x and p_y distributions of the three atoms are the same due to the x/y symmetry. This fact is seen clearly on the projected density of states for each direction (see figure 4.4-f) where p_x and p_y are identical.

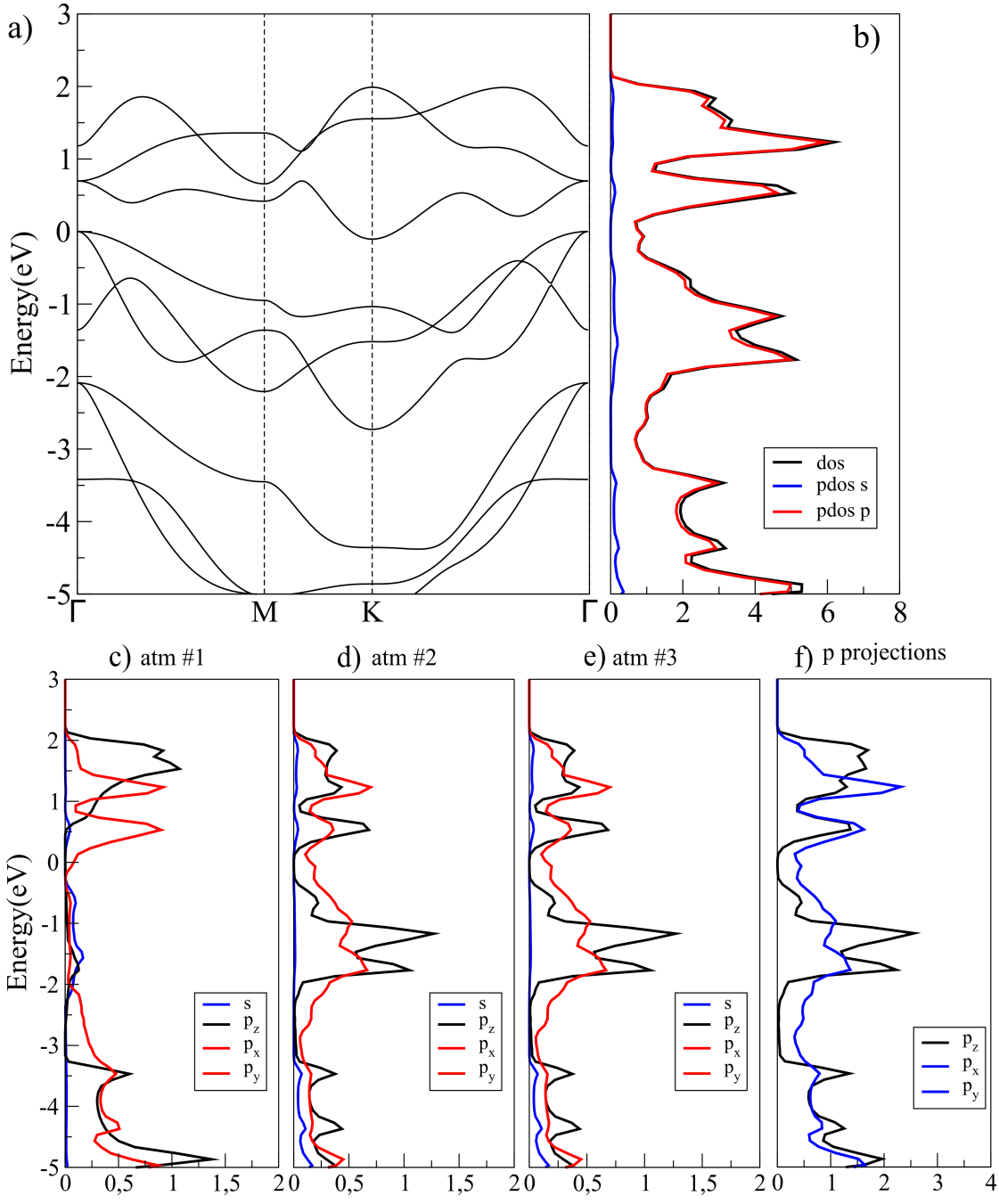

Figure 4.4: (a) Band structure, (b) density of states (black lines) as well as the projected density of states for s (p) as blue (red) lines for γ-Te allotrope. Projected density of states for (c) atom 1, (d) 2 and (e) 3, and, (f) per p state projection in each direction

The α-Te phase (figure 4.5) shows a semiconductor behavior with the CBM located at the Γ point and the VBM located at two points: T and T^*. The former is located in the first half of the path between Γ and M, while the later is in the last half of the path between K and Γ. Both indirect gaps are 0.75 eV in size, while the direct gap is 0.90 eV, and is located at T. The density of states contributions arise from the same orbitals as in bulk phase, namely 5p (predominant) and 5s. In addition, the projected density of states per atom shows the symmetry between atom 2 and 3 (figure 4.5-c-e), while atom 1 is different. This difference is more notable in the range of energies between 0 eV and -1.8 eV where the s orbital dominates in atom 1 but on atom 2 and 3 contributions come from the p orbitals. For the CBM we have a slightly higher p_z contributions in contrast to p_x and p_y for all three atoms. On the other hand, the projected density of states in each direction (figure 4.5-f) clearly shows the hexagonal symmetry due to the equal distribution of p_x and p_y states. One more time, the contribution from the p_z component is slightly higher at the CBM, but the three directions contribute the same at the VBM.

Since Te is a heavy atom and a semiconductor for α-Te allotrope, we are also interested as well in the behavior of the gap when SOC is turned on. For α-Te, the direct band gap becomes smaller, and changes from T to Γ position, as can be appreciated from figure 4.6-a with a value of 0.51 eV. On the other hand, the indirect gap is now 0.39 eV, and is still formed by the points $\Gamma - T$ and $\Gamma - T^*$. In respect to the DOS for SOC case (figure 4.6-b), we can conclude that the largest contribution comes from p orbitals with total angular momentum equal to $j = 1/2$ and $j = 3/2$, where the first contribute slightly more to the CBM, and the second to the VBM. In addition, the projected density of states per atom (figure 4.6-c,d,e) shows previous results for non-SOC case, *i.e.*, the identical spectras for atom 2 and 3, and the total contribution from s state of atom 1 in the region from 0 eV to -1.8 eV. The major contributions to the CBM coming equally from p($j = 3/2$, $m_j = \pm 3/2$) (black lines), p($j = 3/2$, $m_j = \pm 1/2$) (red lines) and p($j = 1/2$, $m_j = \pm 1/2$) (green lines). While VBM contributions arise mostly from p($j = 3/2$, $m_j = \pm 3/2$). Figures 4.6-c,d,e,f also show that contributions arising from m_j projections with opposing signs are identical.

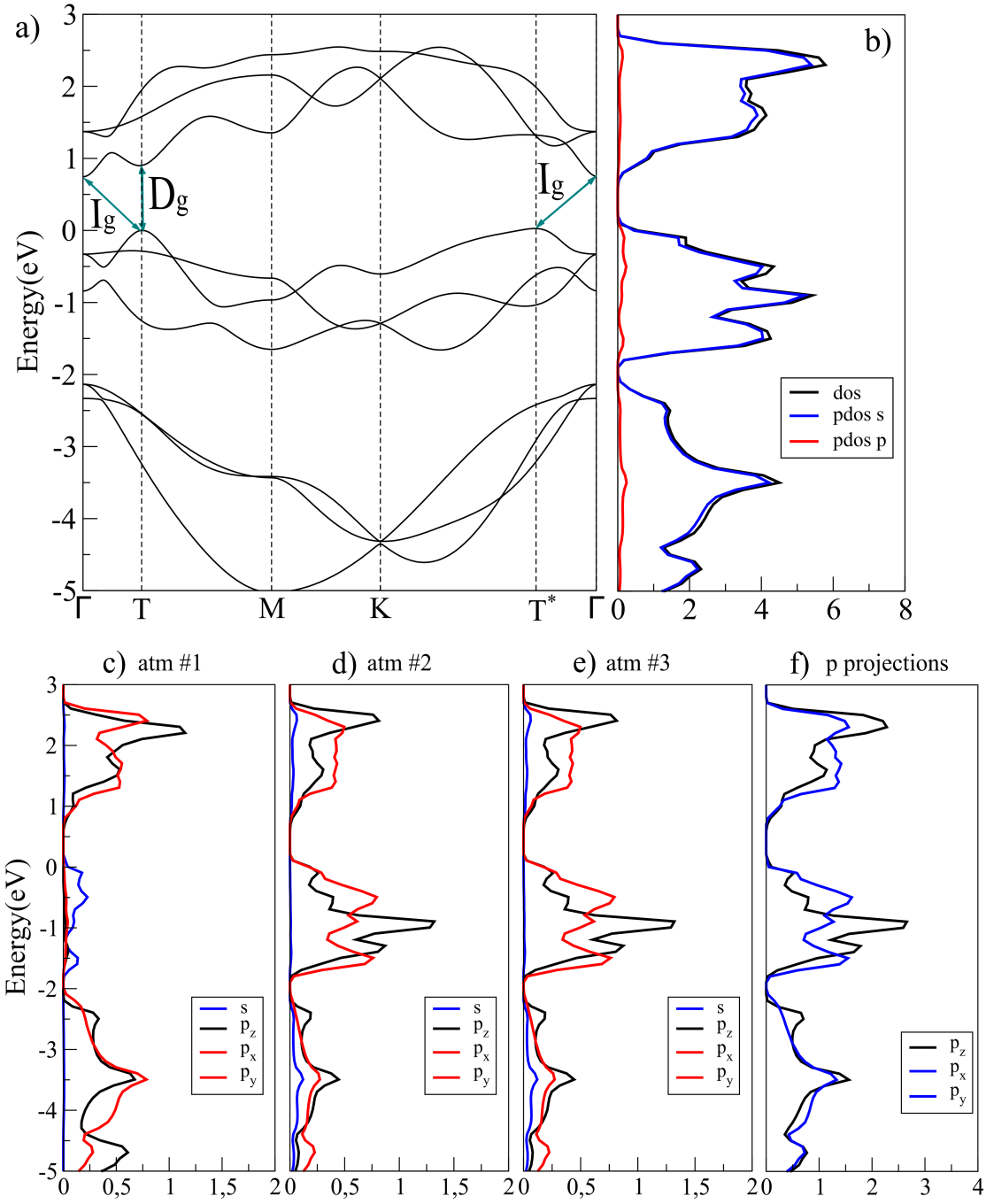

Figure 4.5: (a) Band structure, (b) density of states (black lines) as well as the projected density of states for s (p) as blue (red) lines for α-Te allotrope. Projected density of states for (c) atom 1, (d) 2 and (e) 3, and, (f) per p state projection in each direction

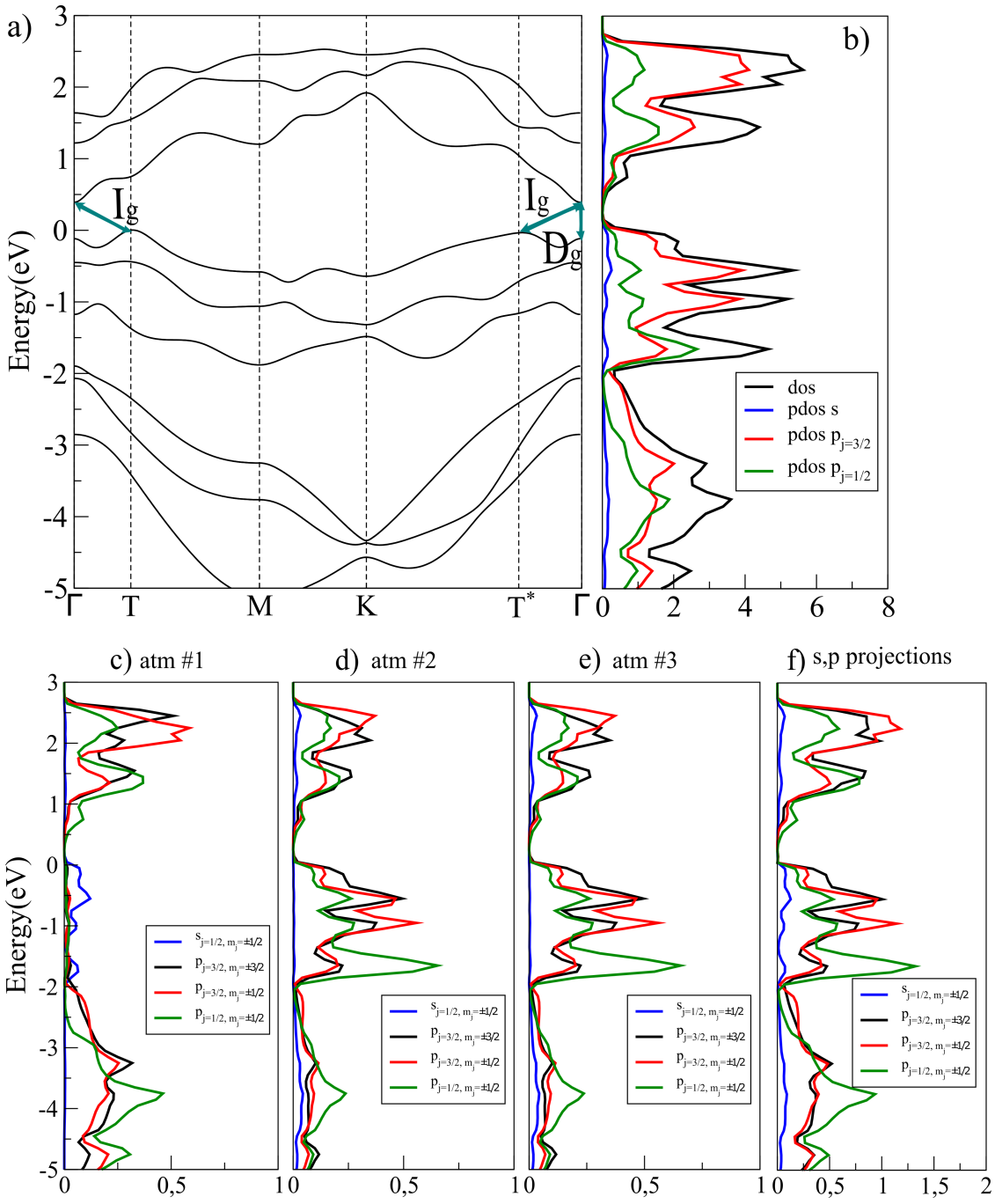

Figure 4.6: (a) Band structure, (b) density of states (black lines) as well as the projected density of states for s ($p_{j=3/2}$, $p_{j=1/2}$) as blue (green, red) lines for α-Te allotrope in the presence of SOC. Projected density of states for (c) atom 1, (d) 2, (e) 3, and, (f) per m_j projection

Lastly, β-Te allotrope has a semiconductor behavior with a direct band gap of 1.50 eV located at the Γ point, while and indirect band gap with 1.13 eV as is presented in figure 4.7-a. Its density of states, as in previous cases, has a dominant p contribution coming from 5p orbital and a non-zero distribution coming from 5s (figure 4.7-a). In addition, the projected density of states per atom show the symmetry of the system in the distributions for atom 1 and 2 (figure 4.7-c,d,e). The biggest contribution to the CBM arises from p_z and p_y in case of atoms 1 and 2, and from p_x and p_y for atom 3. On the other hand, for the VBM we have slightly larger contributions coming from p_x and p_y for atom 1 and 2, but on atom 3 we conclude that s states overlap p ones. Furthermore, the calculations on projected density of states per direction shows different distributions for all directions (figure 4.7-f), which is expected since the system has no x/y symmetry. Around the CBM, we have slightly dominant p_z and p_y components, meanwhile on VBM it is p_x.

When SOC is turned on, the direct band gap becomes narrow at Γ because of a change in curvature on the CBM (see figure 4.8-a). Now, the size of both, the direct and indirect gap, becomes approximately 1.04 eV. In respect to the density of states, we can conclude that the large contribution comes from 5p orbitals with total angular momentum equal to $j = 1/2, 3/2$, where $j = 1/2$ contributes slightly more to the VBM, while the CBM presents a mixture of $j = 1/2$ and $j = 3/2$. Furthermore, the projected density of states per atom (figure 4.8-c,d,e) shows the simmetry of atom 1 and 2. The major contributions to the CBM come p($j = 1/2$, $m_j = \pm 1/2$) (green lines), while at the VBM we have equal contributions from p($j = 3/2$, $m_j = \pm 3/2$) (black lines) and p($j = 1/2$, $m_j = \pm 1/2$) (green lines) (see figure 4.8-f). Figures 4.8-c-f also show that contributions arising from m_j projections with opposing signs are identical.

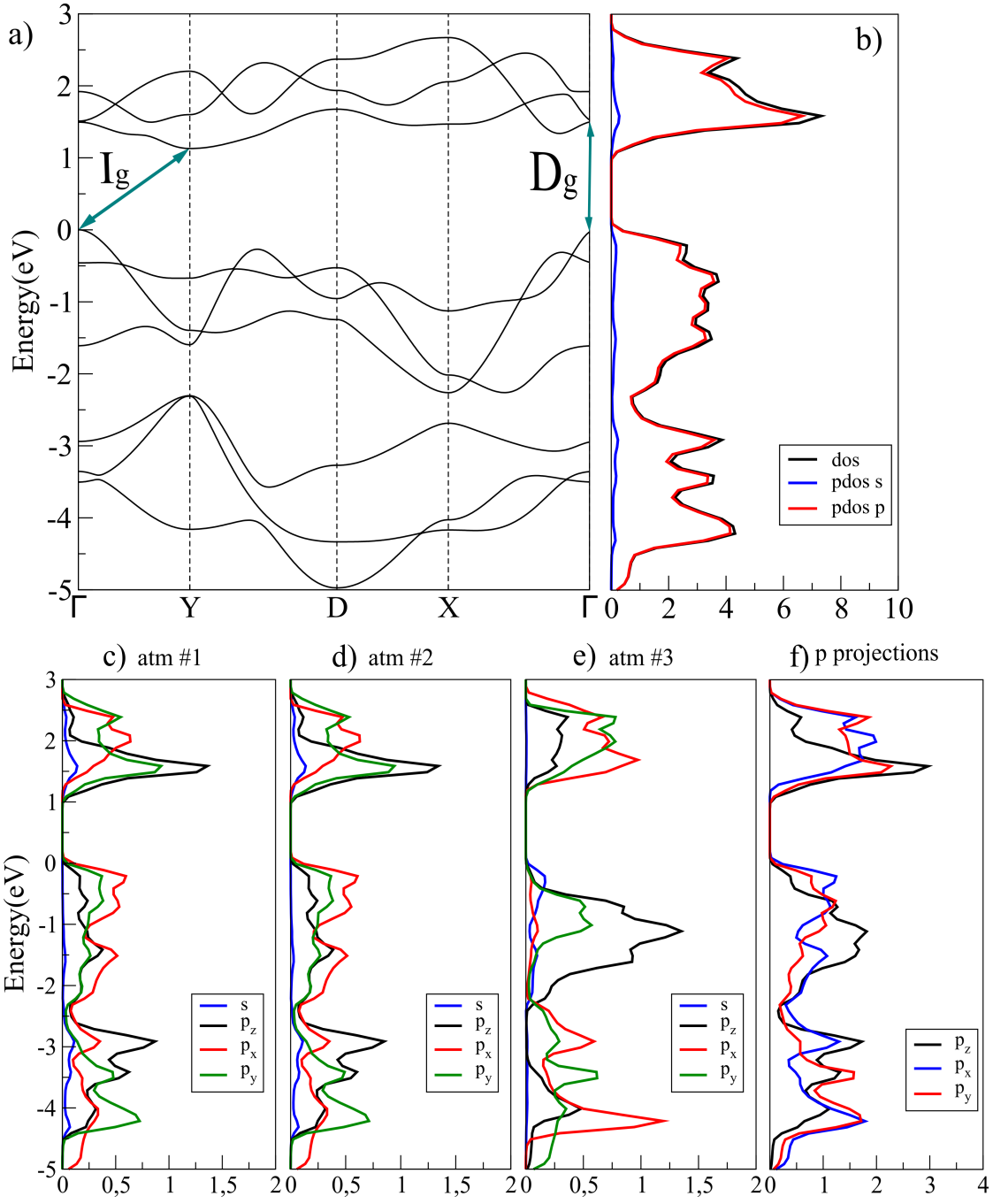

Figure 4.7: (a) Band structure, (b) density of states (black lines) as well as the projected density of states for s (p) as blue (red) lines for β-Te allotrope. Projected density of states for (c) atom 1, (d) 2 and (e) 3, and, (f) per p state projection in each direction

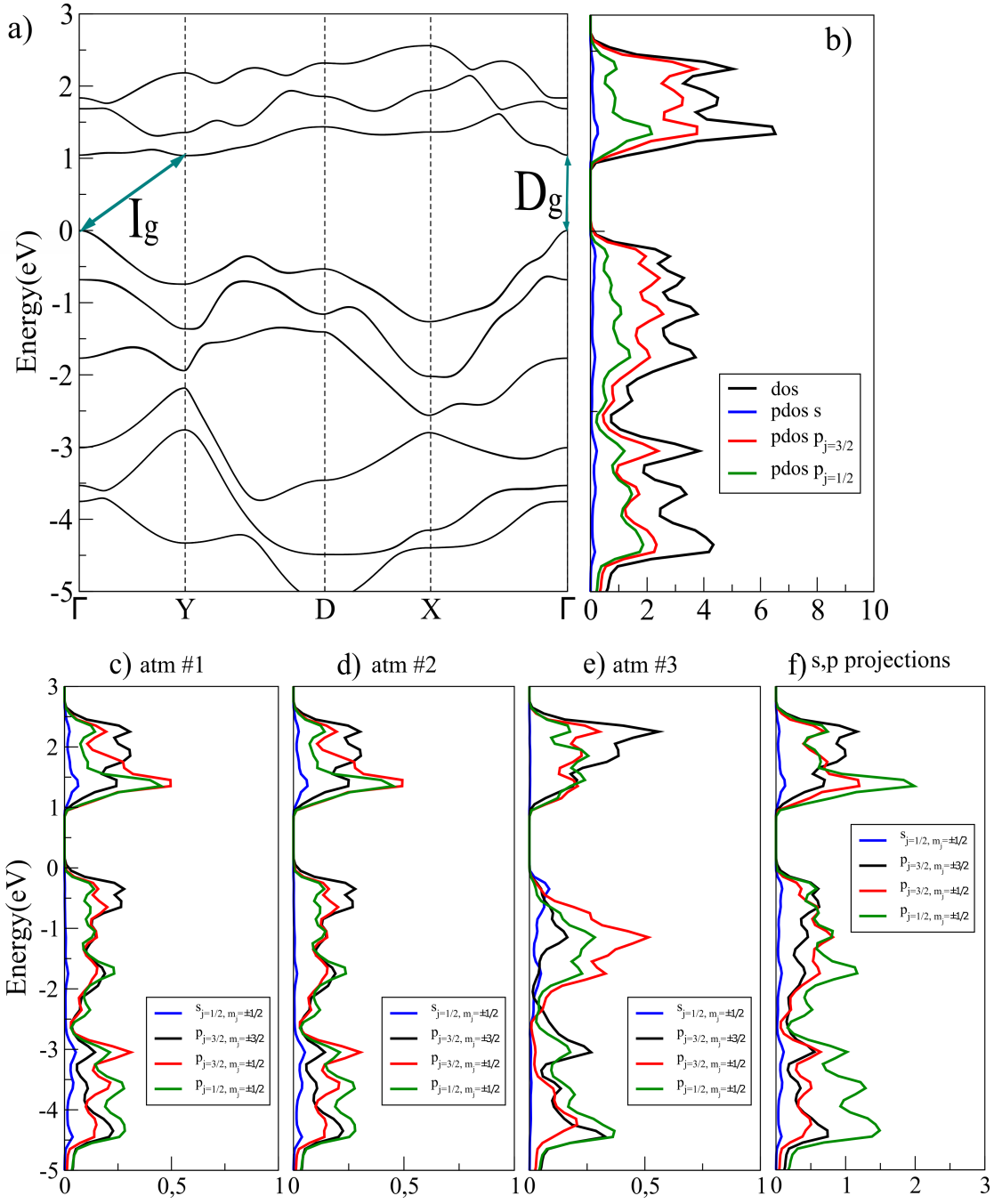

Figure 4.8: (a) Band structure, (b) density of states (black lines) as well as the projected density of states for s ($p_{j=3/2}$, $p_{j=1/2}$) as blue (green, red) lines for β-Te allotrope in the presence of SOC. Projected density of states for (c) atom 1, (d) 2, (e) 3, and, (f) per m_j projection

4.3.3 Effective Masses

The hydrogenic model described in chapter 3 for predicting exciton binding energies, first requires the identification of the most probable places in the band structure where transitions happen. This corresponds (ignoring electron-phonon interactions for indirect transitions) to the direct transitions. So, in this section, we extract the curvature (equation (3.43)), and, the effective masses using equation (3.42) for both semiconductor phases, α-Te and β-Te. In respect to the SOC case, since SOC tends to reduce the size of the band gap, we are going to analyze just the β-Te with SOC because the direct band gap of the α-Te phase becomes too small (it changes from 0.90 eV to 0.51 eV) to form excitons. Consequently, our analysis will be applied to three cases: α-Te, β-Te and β-Te with SOC which are detailed in figures 4.9, 4.10 and 4.11 respectively.

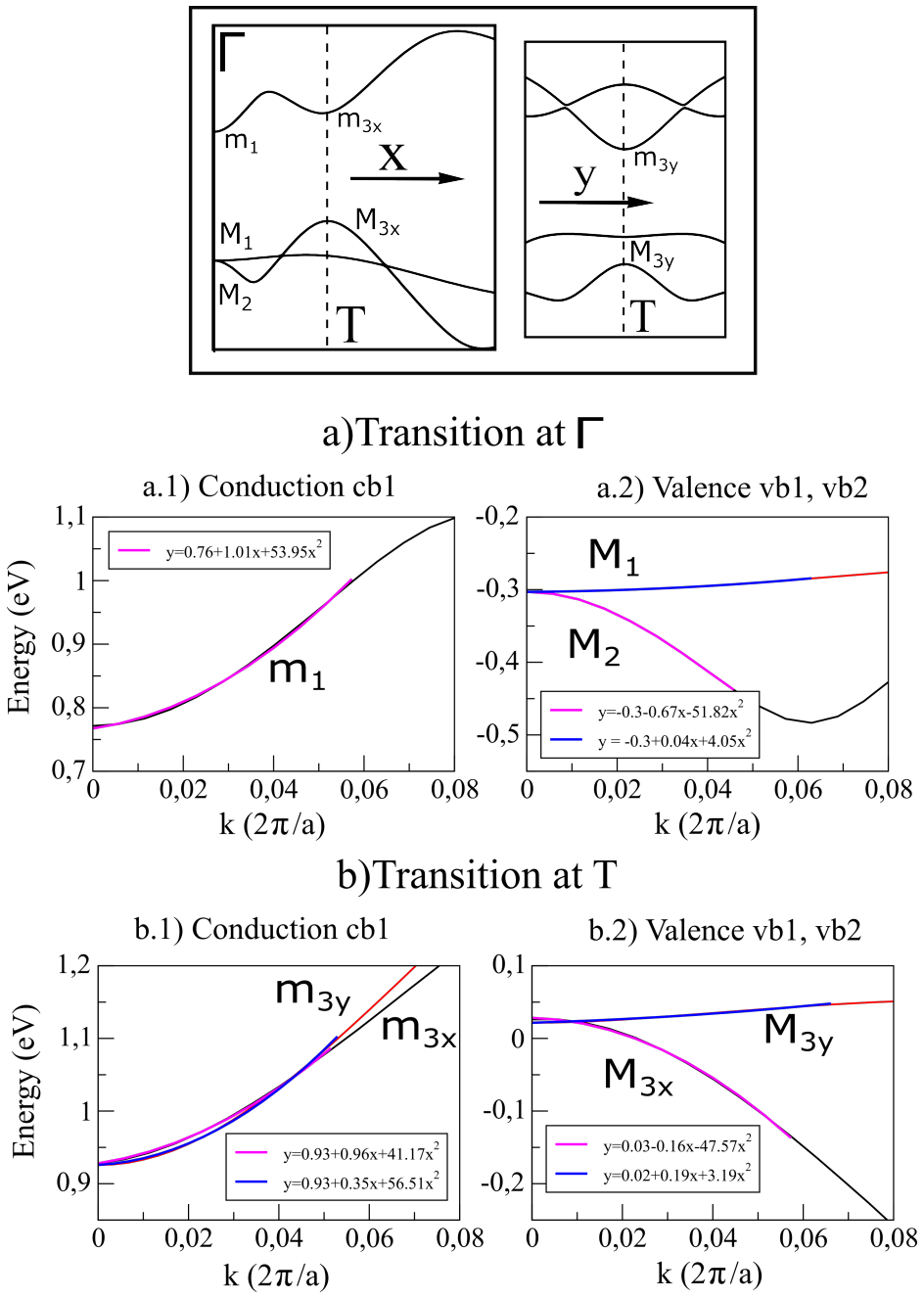

Figure 4.9: Detailed α-Te band structure for transitions happening at a)Γ and b)T, as well as the conduction (a.1, b.1) and valence (a.2, b.2) bands involved in the transitions(at Γ, T).

The band structure of α-Te presents two regions in k-space where the transition could happen, Γ and T (see figure 4.5-a), both transitions can be zoomed in directions x and y as is printed in 4.9-a,b respectively. At point Γ(where x/y directions are equivalent due to the symmetry of α-Te), we identify two possible transitions from the valence bands labeled as vb1 and vb2 (figure 4.9-a.2), whose effective masses for the hole are positive $M_1 = +2.12$ m_e and negative $M_2 = -0.17$ m_e depending on the curvature respectively, to the conduction band cb1 (figure 4.9-a.1) with an effective mass for the electron $m_1 = +0.16$ m_e. On the other hand, At point T we observe that the conduction band cb3 (figure 4.9-b.1) presents the same curvature for both directions with electron masses in x and y direction equal to $m_{3x} = +0.21$ m_e and $m_{3y} = +0.15$ m_e respectively, while the valence band vb3 presents inverted curvature for y direction with a value of $M_{3y} = +2.70$ m_e and a mass in x direction of $M_{3x} = -0.18$ m_e. A summary with the masses of electrons and holes is represented in table 4.4.

Transition	e-mass(m)	h-mass(M)	Reduced mass(μ)
$vb1 \rightarrow cb1$ at Γ	$m_1 = +0.16$	$M_1 = +2.12$	$\mu_{x/y} = 0.17$
$vb2 \rightarrow cb1$ at Γ	$m_1 = +0.16$	$M_2 = -0.17$	$\mu_{x/y} = 0.08$
at T	$m_{3x} = +0.21$ $m_{3y} = +0.15$	$M_{3x} = -0.18$ $M_{3y} = +2.70$	$\mu_x = 0.10$ $\mu_y = 0.16$

Table 4.4: α-Te masses for electrons(m) and holes(M) in units of the electron mass m_e (with signs +/- depending on the curvature of the band), the effective masses are deduced using equations (3.42), (3.43)), and the reduced mass is calculated using (3.64)

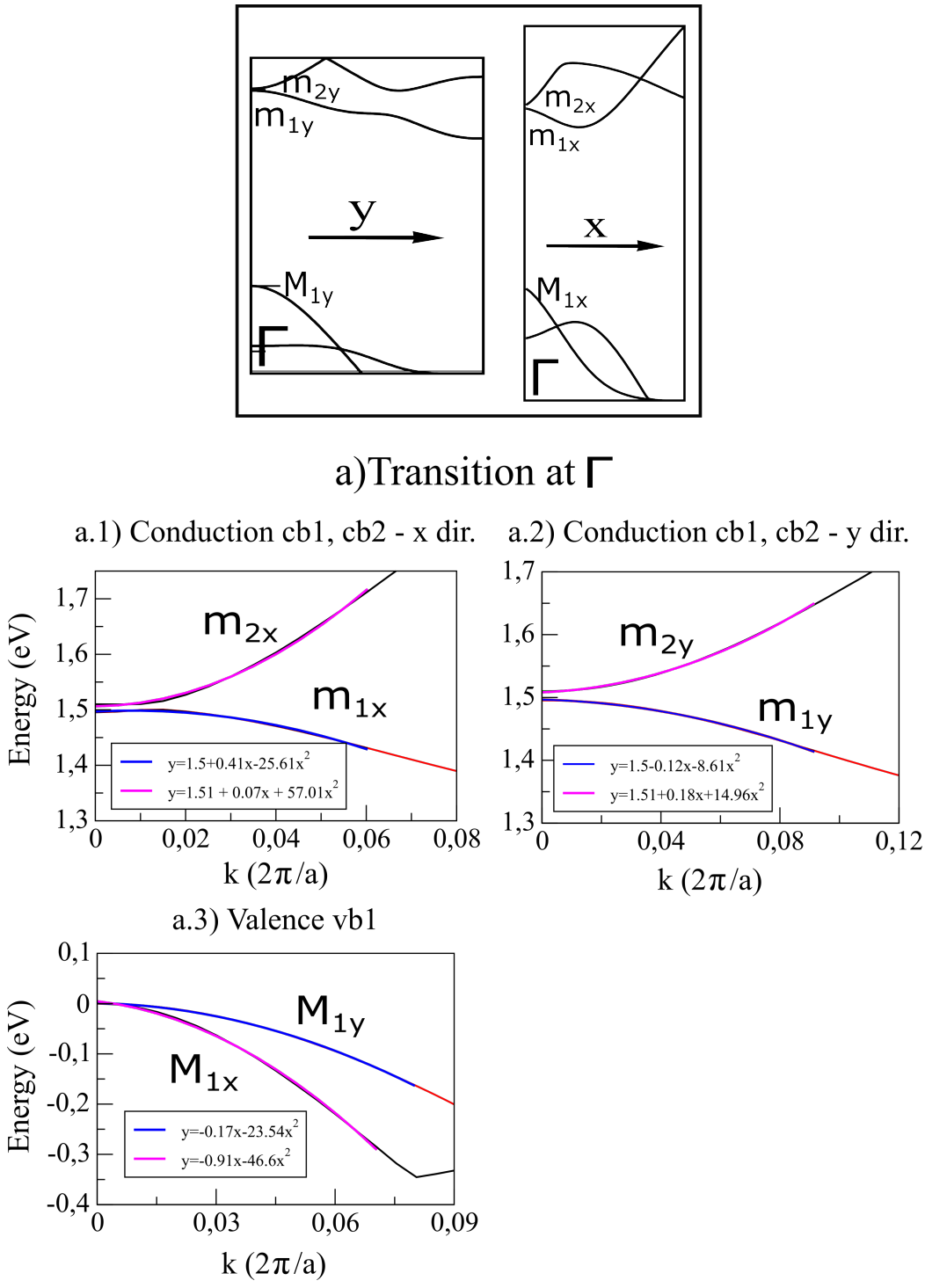

Figure 4.10: Detailed β-Te band structure for transitions happening at a)Γ, as well as the curvature in each direction (x, y) for the conduction (a.1, a.2) and valence (a.3) bands involved in the transitions from vb1 to cb1 or cb2.

For β-Te phase we identify two transitions at Γ due to the degeneracy of the conduction band (see figure 4.10). These are the transitions from valence band vb1 to the conduction bands cb1 and cb2. By zooming at Γ, the conduction band cb1 and cb2 (figure 4.10-a.1,a.2) present negative and positive effective electron masses shown in table 4.5. And, the valence band vb1 (figure 4.10-a.3) has a negative hole mass for both x and y directions respectively. Results on β-Te are summarized on table 4.5.

Transition	e-mass(m)	h-mass(M)	Reduced mass(μ)
$vb1 \rightarrow cb1$ at Γ	$m_{1x} = -0.34$	$M_{1x} = -0.19$	$\mu_x = 0.41$
	$m_{1y} = -1.01$	$M_{1y} = -0.37$	$\mu_y = 0.58$
$vb1 \rightarrow cb2$ at Γ	$m_{2x} = +0.15$	$M_{1x} = -0.19$	$\mu_x = 0.08$
	$m_{2y} = +0.58$	$M_{1y} = -0.37$	$\mu_y = 0.23$

Table 4.5: β-Te masses for electrons(m) and holes(M) in units of the electron mass m_e (with signs +/- depending on the curvature of the band), the effective masses are deduced using equations (3.42), (3.43)), and the reduced mass is calculated using (3.64)

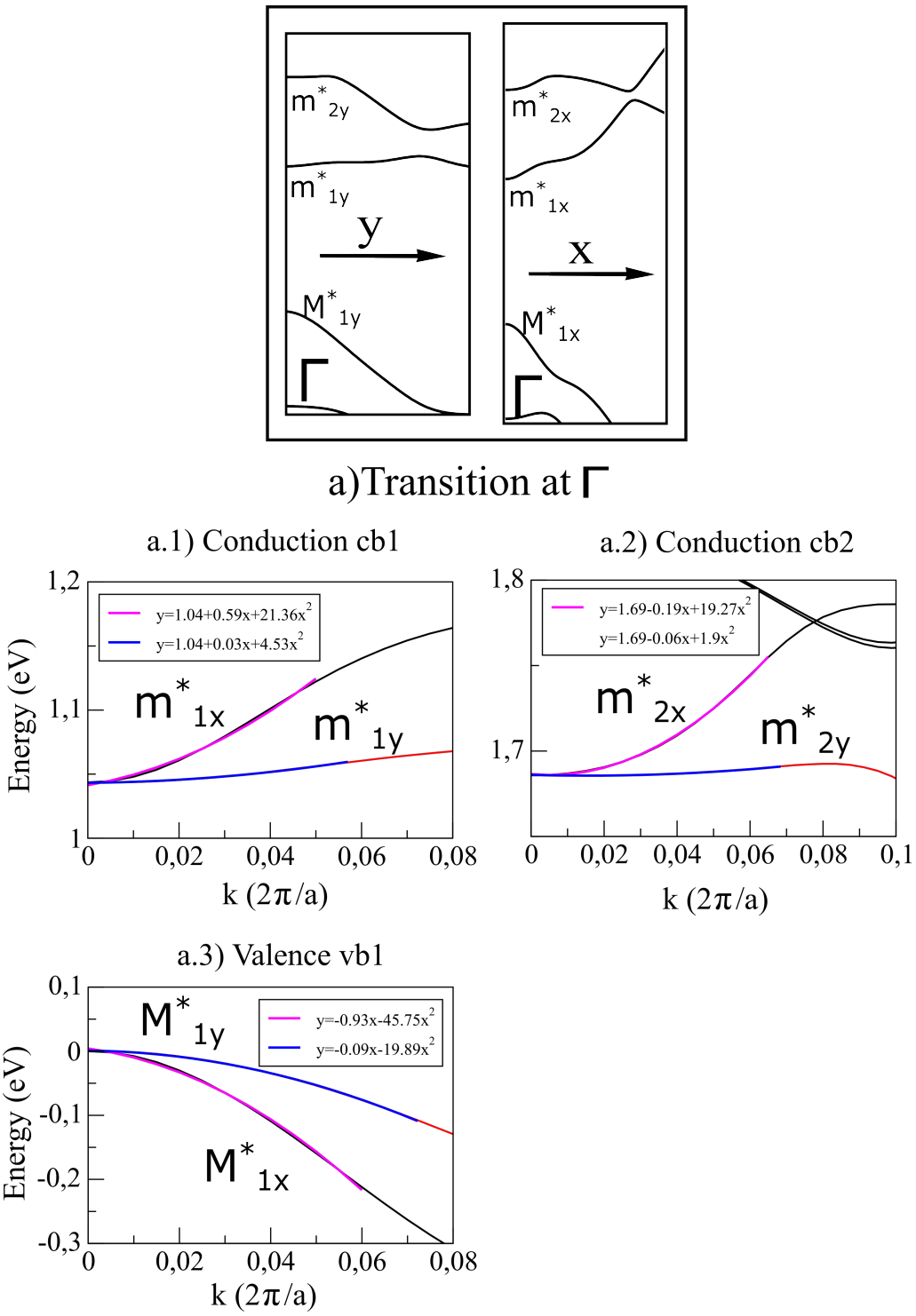

Figure 4.11: Detailed β-Te + SOC band structure for transitions happening at a)Γ, as well as the curvature in each direction (x, y) for the conduction cb1(a.1) and cb2(a.2) and valence vb1(a.3) bands involved in the transitions.

The last case is when SOC is turned on. Here we found that the degeneracy on the conduction band is no longer present. In addition, it is possible to notice that the conduction band cb1 change its curvature to positive. However, transitions will possibly be happening with the same band index as in the non-SOC case (*i.e.* from vb1 to cb1 and vb1 to cb2). The effective masses of the hole and electron are represented with an $*$ in table 4.6.

Transition	e-mass(m^*)	h-mass(M^*)	Reduced mass(μ^*)
$vb1 \rightarrow cb1$ at Γ	$m^*_{1x} = +0.41$ $m^*_{1y} = +1.91$	$M^*_{1x} = -0.19$ $M^*_{1y} = -0.44$	$\mu^*_x = 0.13$ $\mu^*_y = 0.36$
$vb1 \rightarrow cb2$ at Γ	$m^*_{2x} = +0.45$ $m^*_{2y} = +4.56$	$M^*_{1x} = -0.19$ $M^*_{1y} = -0.44$	$\mu^*_x = 0.13$ $\mu^*_y = 0.40$

Table 4.6: β-Te + SOC masses for electrons(m^*) and holes(M^*) in units of the electron mass m_e (with signs +/- depending on the curvature of the band), the effective masses are deduced using equations (3.42), (3.43)), and the reduced mass is calculated using (3.64)

4.4 Dielectric constant and 2D polarization

The structures described on section 4.1 correspond to the lowest energy configurations, and, the most stable ones with respect to phonon perturbations. The dielectric constant of the system can be calculated by performing a perturbation (with a small electric field) in the system. Furthermore, as we have shown in chapter 3, the dielectric constant is linearly dependent on the interlayer distance (see equation (3.34)), whose slope gives us the 2D polarization α_{2D}. For this reason, by performing phonon calculations, we are able to construct the dielectric constant in terms of the interlayer distance, and so, calculate the 2D polarizability. Phonons calculations were also performed using Quantum Espresso package for the semiconductor phases: α-Te and β-Te with and without SOC as a function of the vacuum (shown in figure 4.12-a,b,c). In our calculations we varied the interlayer distance from 6 Å to 15 Å. The 2D polarization for α-Te is symmetric for x/y directions and has a value of α_{2D} = 17.70 Å. For β-Te we observe an anisotropic dielectric constant where x direction take a value of α_{2D} = 8.04 Å and y is α_{2D} = 5.76 Å. Our analysis extended to β-Te with SOC case show that the polarization does not change drastically, *i.e.*, for x direction we obtain α_{2D} = 9.29 Å and y is α_{2D} = 6.01 Å. The results then show that in case of α-Te we have a large dielectric constant, almost twice the value for β-Te.

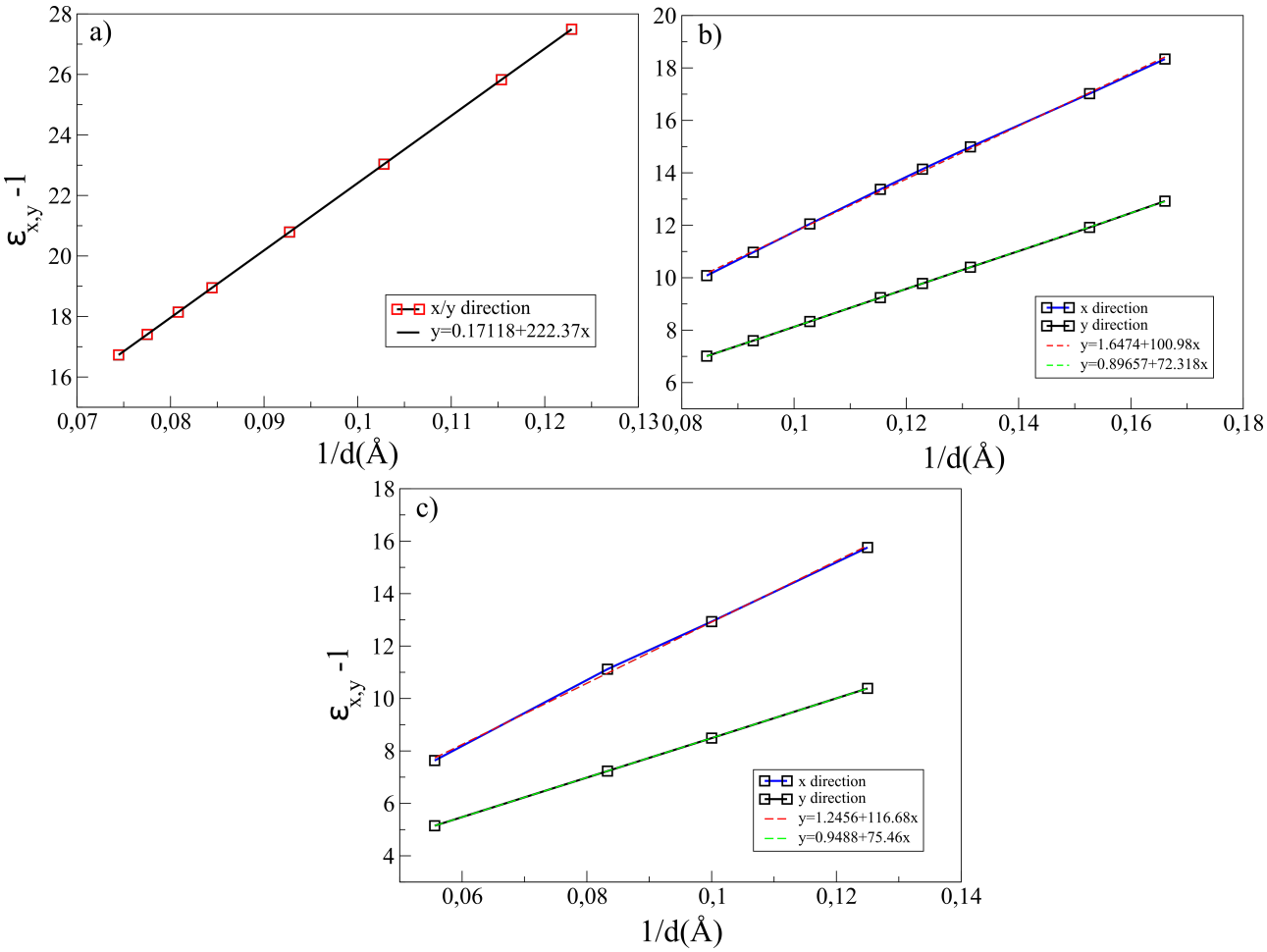

Figure 4.12: Imaginary part of the dielectric constant as a function of the inverse of the inter-layer distance for the different Te allotropes: (a) α-Te, (b) β-Te and (c) β-Te + SOC

4.5 GW Band Structure

In chapter 2, we have stated that GGA-PBE calculations underestimate the band structure of the system. For this reason, we perform quasiparticle corrections (GW Approximation) to the energies in the band structure. The GW approximation has been calculated using the Yambo code [69] with the results shown in figures 4.13 and 4.14.

	$\mathbf{E}_{Dg}^{GW}(eV)$	$\mathbf{E}_{Ig}^{GW}(eV)$
α-Te	1.70	1.49
β-Te	2.53	2.4
Prev. Res.	2.35 [58]	-

Table 4.7: Band structure direct($\mathbf{E}_{Dg}^{PBE}$) and indirect gaps($\mathbf{E}_{Ig}^{PBE}$) as well as SOC inclusion ($\mathbf{E}_{Dg}^{PBE+SOC}$, $\mathbf{E}_{Ig}^{PBE+SOC}$) for Bulk-Te and monolayer-Te phases: α-Te, β-Te and γ-Te.

α-Te results show high dispersion in what respect to the quasiparticle energy corrections (see figure 4.13-b). For this reason, the GW bands can not be considered as a rigid shift of GGA bands (see figures 4.13-a). The new indirect and direct gap have values of 1.49 eV

and 1.70 eV and are located at a different position with respect to DFT calculations, they are located in the path $\Gamma - M$ at points C for direct transitions and $C - D$ for the indirect transition. On the other hand, for β-Te, we observe that quasiparticle energies differ by a rigid shift of DFT bands. So, the direct gap changes its value to 2.53 eV, which is almost 1 eV in difference with respect to GGA; while the indirect gap is enlarged up to 2.4 eV, which is 1.27 larger than the DFT indirect gap. The former is still happening at the Γ point, while the later links the new CBM at B and the VBM at Γ.

The results on α-Te band structure after considering the self energy correction through G_0W_0 approach are new on the literature and still need to be compared with other results for this allotrope. On the other hand GW correction on β-Te can be compared with reference [58]. There is just 8% in discrepancy, that can be attributed to different parameters in the calculations.

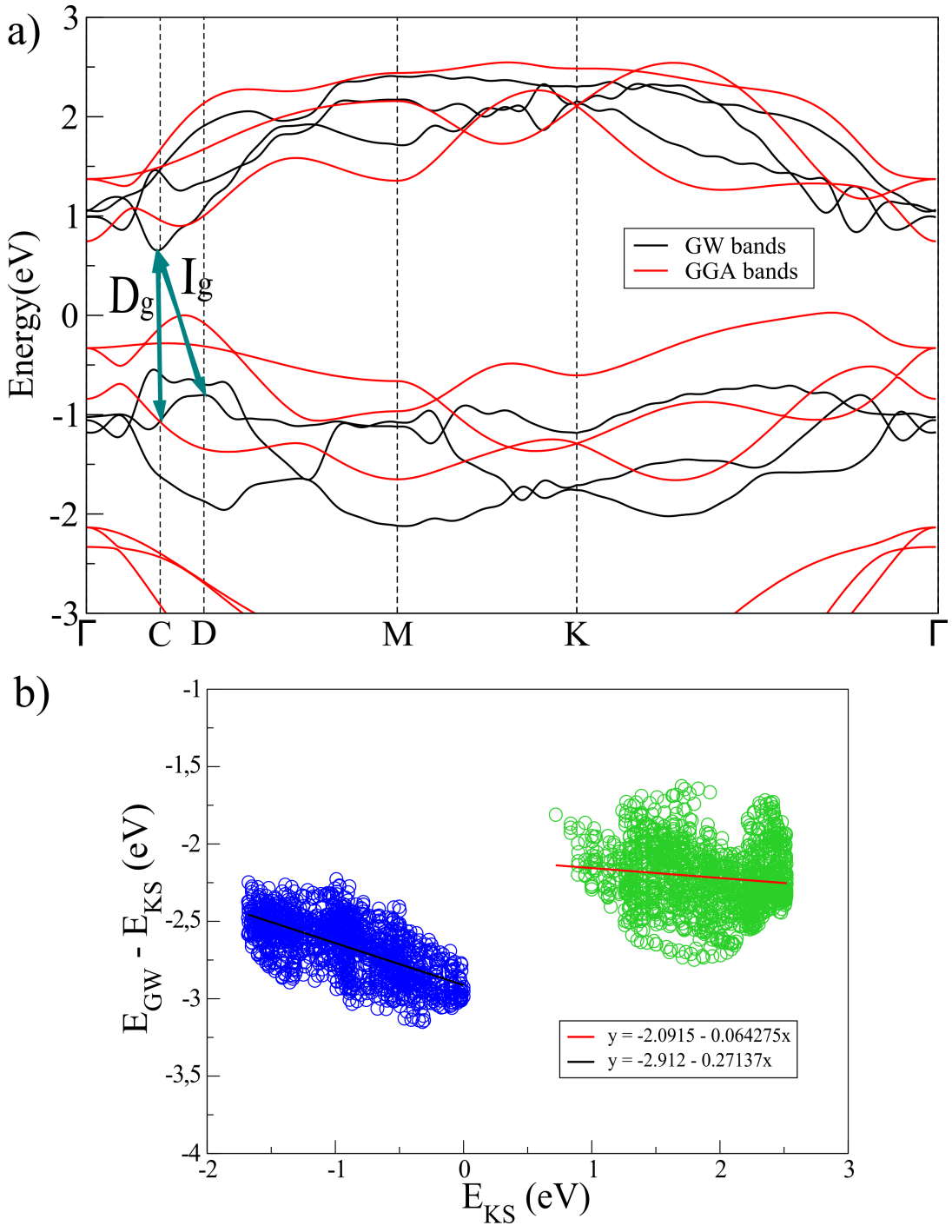

Figure 4.13: (a) Band structure for GW (black lines) and GGA (red lines) levels of theory, and (b) energy dispersion between GW approximation and KS for α-Te, for valence (blue) and conduction bands (green). A straight line indicates that GW calculation corresponds to a rigid shift of the bands. Both lines present high dispersion with a total sum of squares of 56.79 for the red line (regression of the conduction band), and 47.24 for the black one (regression of the valence band).

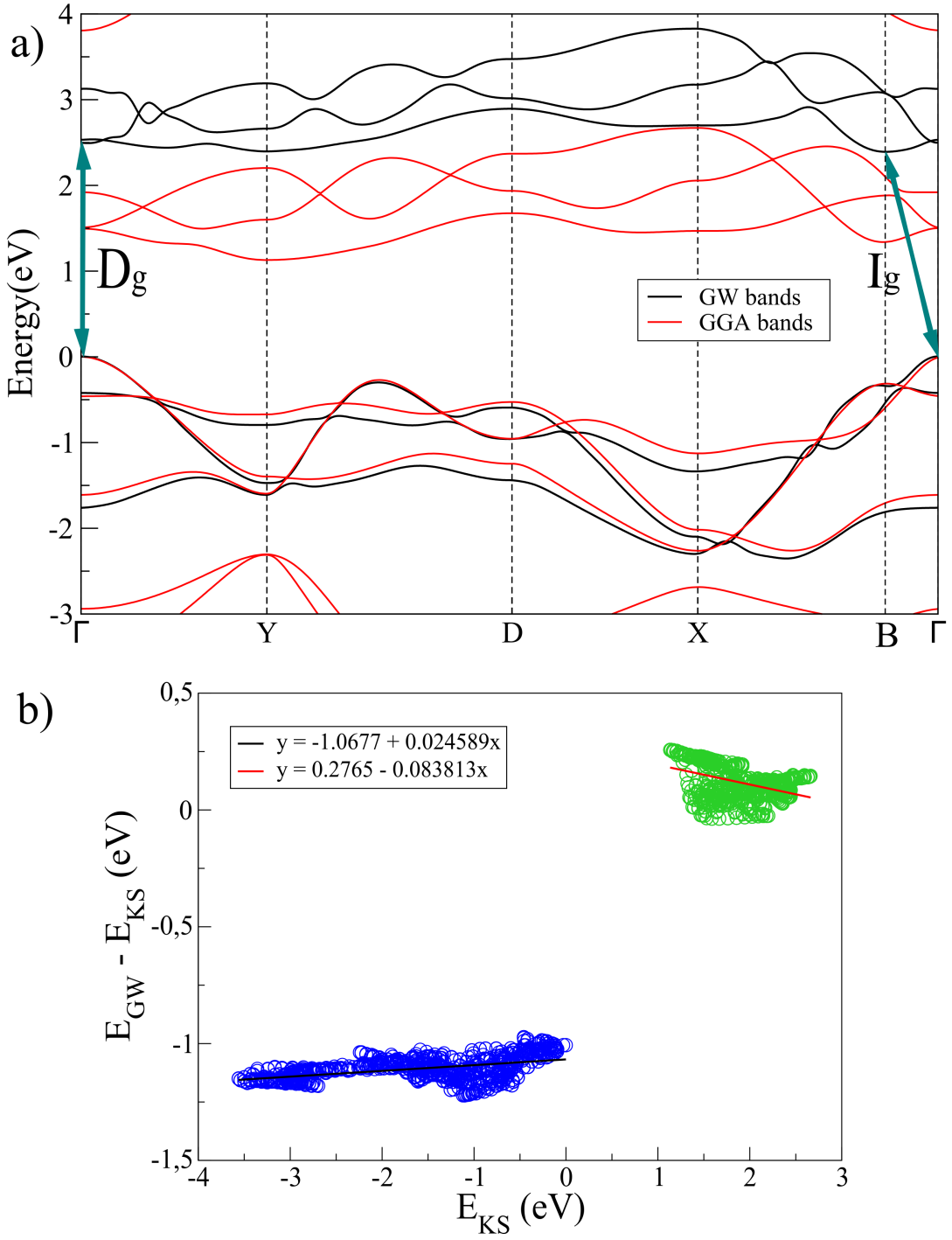

Figure 4.14: (a) Band structure for GW(black lines) and GGA(red lines) levels of theory, and (b) energy dispersion between GW approximation and KS for β-Te, for valence (blue) and conduction bands (green). A straight line indicates that GW calculation corresponds to a rigid shift of the bands.

4.6 Optical Absorption

The calculations for the imaginary part of the dielectric constant can be obtained within different levels of theory as we have seen in chapter 2. The IPA level does not include information on the Hartree potential nor of the kernel for the linear response theory (equation 2.48). In the RPA, on the other hand, one considers the Hartree term on the polarization but not the exchange-correlation potential. And, lastly the BSE dielectric constant is obtained after solving the Bethe Salpeter equation, in which the exchange-correlation kernel $\tilde{K}^*$ is considered. The best approximation for the dielectric constant, specially for semiconductors, corresponds to the BSE level of theory; but, the RPA, as we have seen in chapter 1, defines the band edge for which it is possible to identify the exciton binding energies.

4.6.1 α-Te

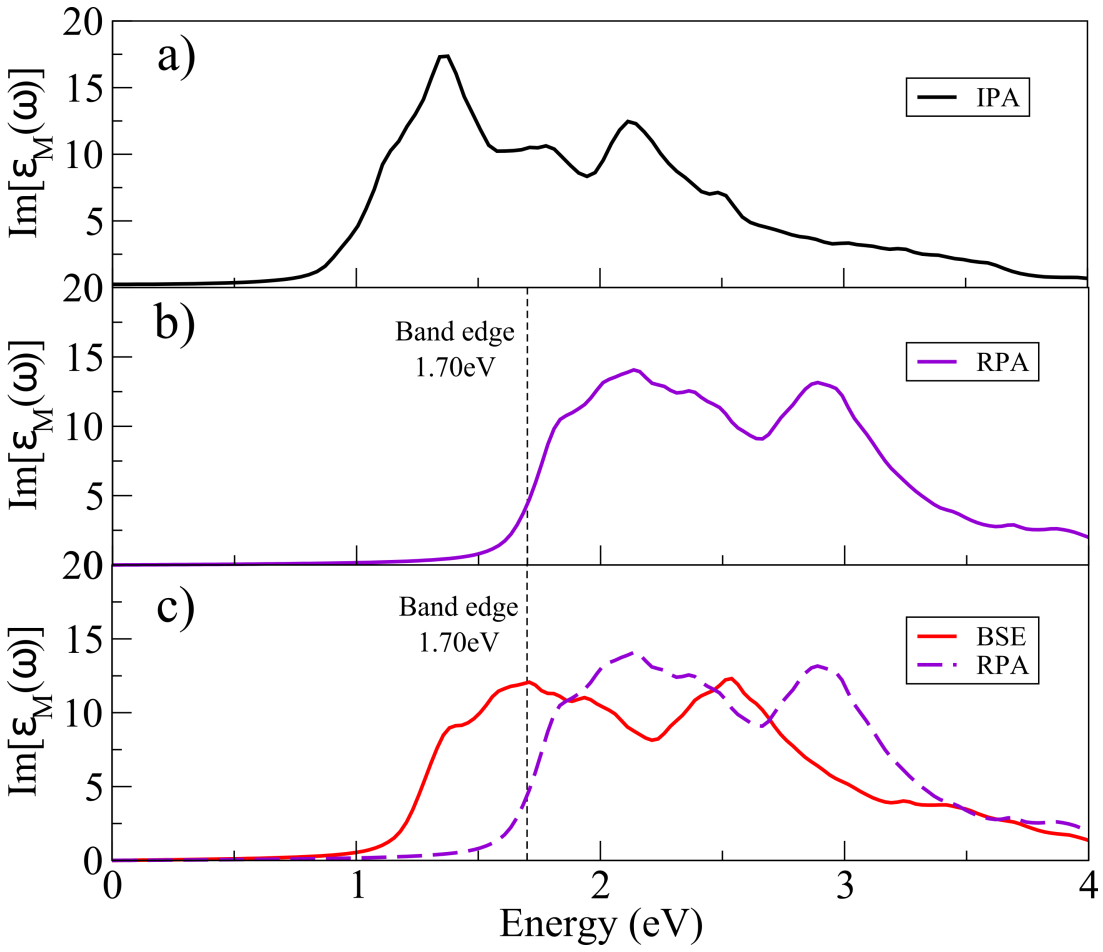

Figure 4.15: Imaginary part of the dielectric constant as a function of energy for different levels of theory: (a) IPA, (b) GW-RPA and (c) GW-BSE for α-Te allotrope

Absorption spectra calculations for α-Te allotrope are printed in figure 4.15. The imaginary part of the dielectric constant in the IPA (blue lines) shows two peaks at 1.36 eV and 2.13 eV. After performing the RPA with quasiparticle corrections for the band structure (GW), the two peaks are red shifted by 0.82 eV. This position defines the band edge at 1.70 eV. And, in the GW-BSE level, we obtain the same spectra as in GW-RPA but shifted by 0.42 eV to the left side (with the two main elevations located at 1.75 eV and 2.53 eV). This red shift has been previously observed for monolayer GeSe in the zigzag direction [40]. The BSE spectra was constructed by the transitions happening at the Γ and T points (see figure 4.16). In addition, since the GW-BSE does not present large peaks in intensity, and has the same shape as the GW-RPA, we can affirm that no stable excitons are formed in the α-Te allotrope.

4.6.2 β-Te

Figure 4.17 and 4.18 show the absorption using three level of theories: IPA, RPA and BSE for light polarized in x and y directions, whereas figure 4.19 compares BSE for diagonal (d), x (ZZ) and y (AC) directions. The anisotropy of β-Te allotrope is clearly seen for the different levels of theory. For example, when the Hartree contribution is not included (IPA), we observe two peaks located at 1.82 eV and 2.62 eV for y-polarization, while in x-polarization there is only one peak located at 1.79 eV . If the exchange correlation kernel is zero but not the Hartree term (RPA), we can see that contribution becomes small in intensity for both directions, and, the starting point on the RPA, which is the value of the direct band gap, defines the band edge of the system with value of 2.53 eV for both directions. Lastly, when e-h correlations are included, it is possible to observe excitons in the brightest peaks. We have select three directions (x,y and diagonal-d) for this allotrope in order to have a complete knowledge on how the anisotropy affects e-h quasiparticles. For x-polarized light direction (see figure 4.17) we have the first exciton located (optical band gap) at 1.87 eV (exciton 1) with a binding energy (BE) of 0.66 eV, and a second peak at 2.08 eV (exciton 2) with a binding energy of 0.45 eV. On the other hand, the vertical direction shows a unique peak at 1.96 eV (exciton 3) with a binding energy of 0.57 eV, which is a third intensity one when compared to the horizontal direction. So, the anisotropy of the imaginary part of the dielectric constant is almost negligible since the brightest peaks are located at almost the same position but with different intensity. Both contributions in x and y can be appreciated on the diagonal direction, where the peaks along the zigzag direction (x) overlap with the ones coming from the armchair direction (y). Consequently, we only observe the excitons labeled 1 and 2. We located three excitons in the band structure (see figure 4.16) and noticed that transitions only occur at Γ. Furthermore, due to the closeness of conduction band cb1 and cb2, we have characterized the bands involved in each transition. So, excitons 1 and 3 (see figure 4.19) are happening between valence band vb1 and conduction band cb1; while exciton 2 enroll transition to conduction band cb2. The large peaks in intensity correspond to bright

excitons which tend to be s states, for example, excitons 1 and 2 correspond to states 1s and $1s^*$ respectively. The nature of 1s-like states comes from the fact that the transition occur to a degenerate conduction band. In addition, we have a 2s and $2s^*$ states located at 2.16 eV and 2.22 eV which contribute with 10% in intensity and has a BE of 0.36 eV (blue solid lines in figure 4.24-a). On the other hand, there are peaks with zero intensity which can not be appreciated in the BSE spectra, and correspond to dark excitons located at the blue dashed lines in the figure 4.24-a and are labeled as p orbitals. The first characterized dark state can be recognized as p_y. BSE spectra in the diagonal is similar to Black phosphorus (BP), for this reason, it is expected that the photoluminiscence will be dictated only by the exciton located at 1.87 eV (labeled as exciton 1) with the linear polarization along the zigzag direction similar to BP. The binding energy of excitons showed for β-Te are similar to BP and TMD's, so it is an strong candidate for development of excitonic-type solar cells. A comparison with previous results is shown in table 4.8.

	ZZ dir. (x)	AC dir. (y)
Optical Gap	1.87 eV	1.96 eV
Prev. Res.	1.68 eV [58]	1.88 eV [58]
Binding Energy	0.66 eV	0.57 eV
Prev. Res.	0.67 eV [58]	0.47 eV [58]

Table 4.8: β-Te brightest exciton comparison with previous results [58] for zigzag - x and armchair - y directions

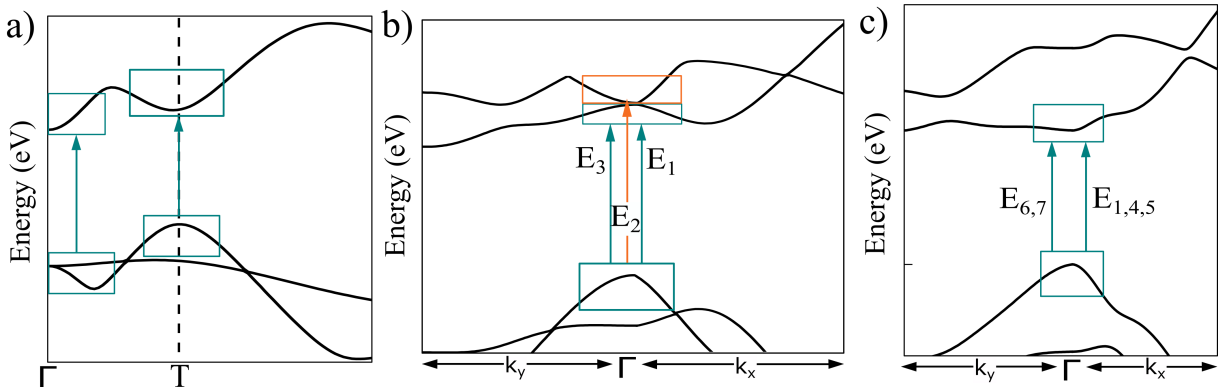

Figure 4.16: (a) Regions where the transitions form the majority of GW-RPA and GW-BSE in α-Te allotrope. Places where the transitions form excitonic states for (b) β-Te and (c) β-Te with SOC, labeled according to sections 4.6.2 and 4.6.3.

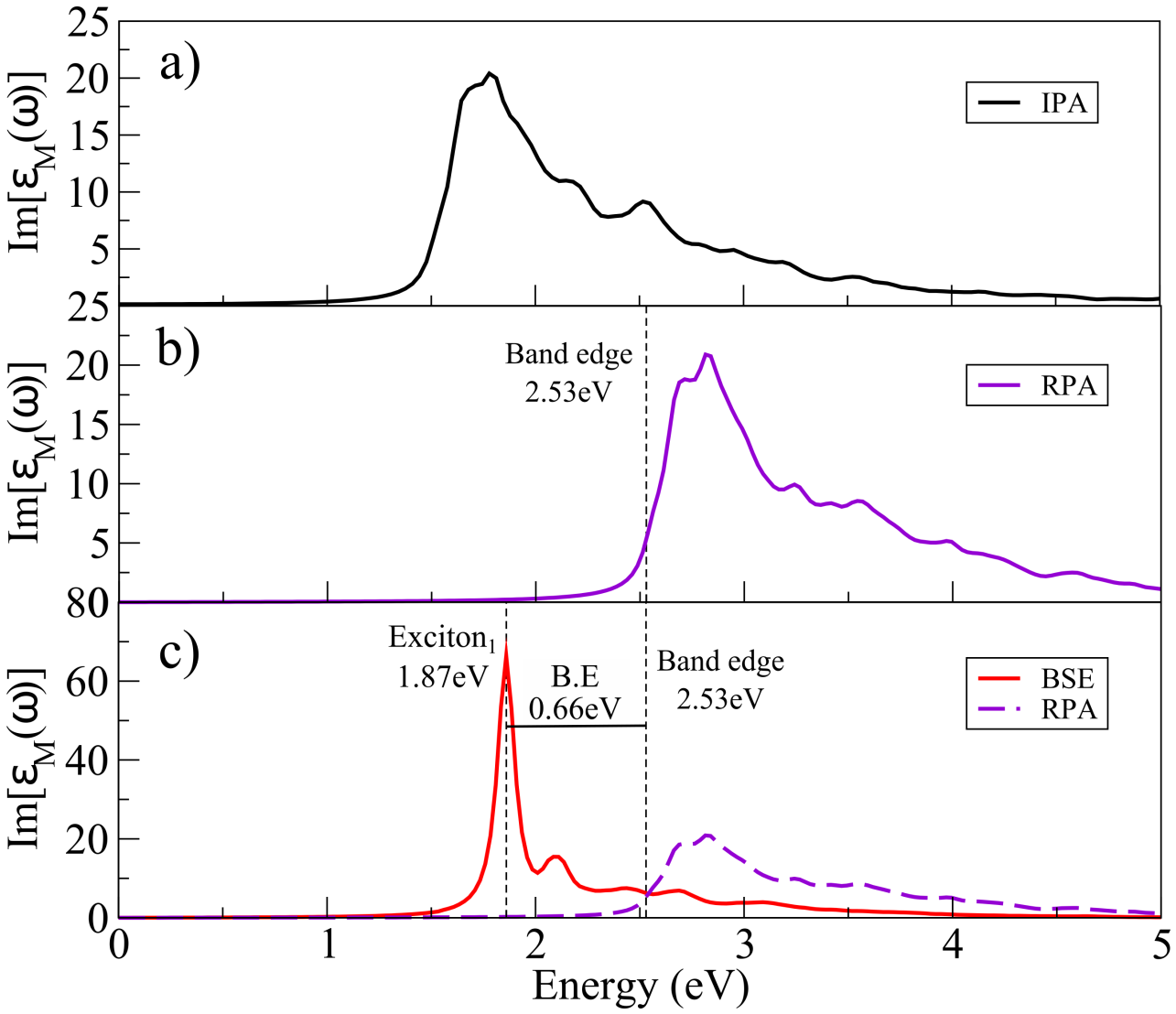

Figure 4.17: Imaginary part of the dielectric constant vs energies for different levels of theory: (a) IPA, (b) GW-RPA and (c) GW-BSE for the zigzag (x) direction in β-Te allotrope

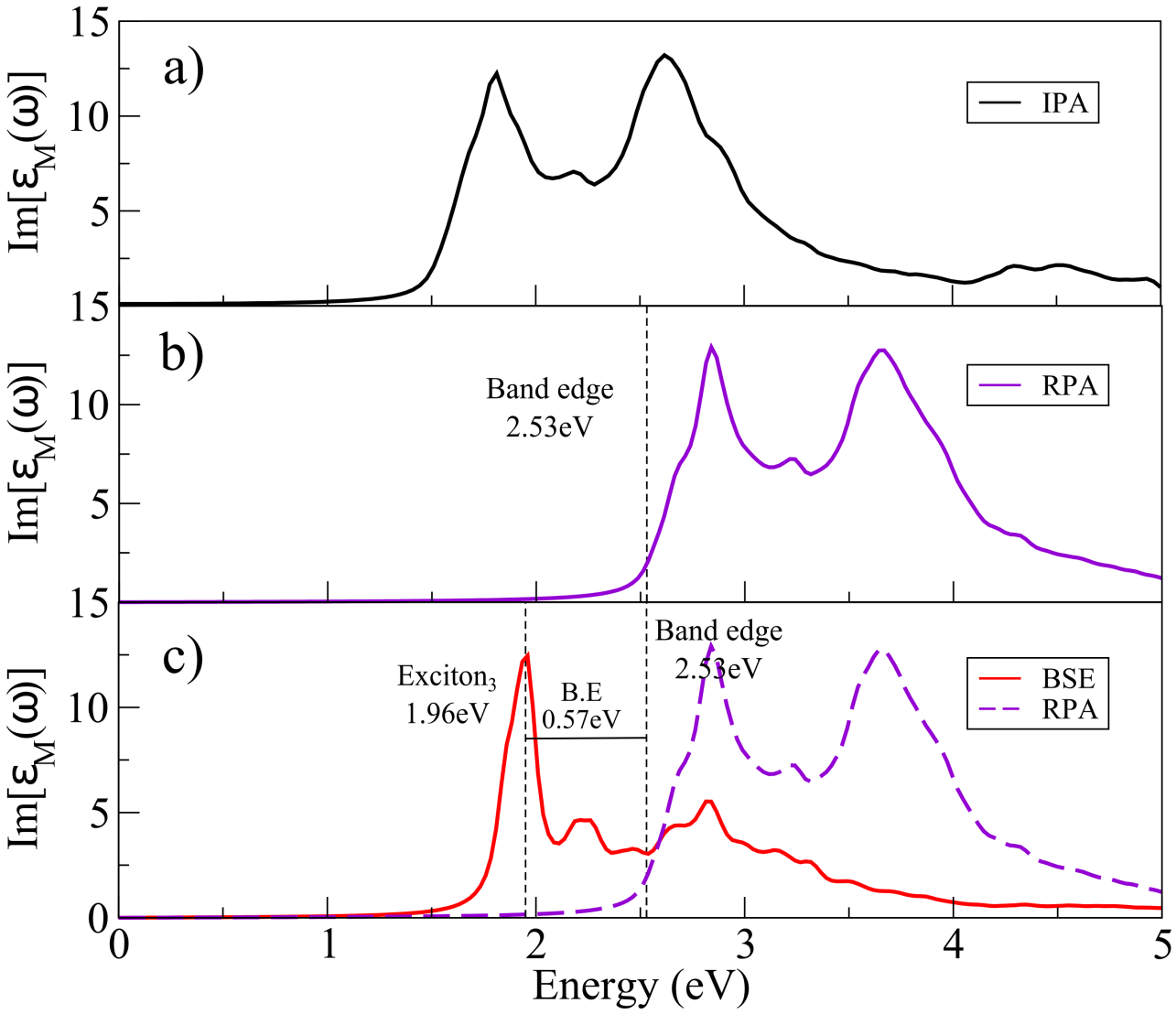

Figure 4.18: Imaginary part of the dielectric constant vs energies for different levels of theory: (a) IPA, (b) GW- RPA and (c) GW-BSE for the armchair (y) direction in β-Te allotrope

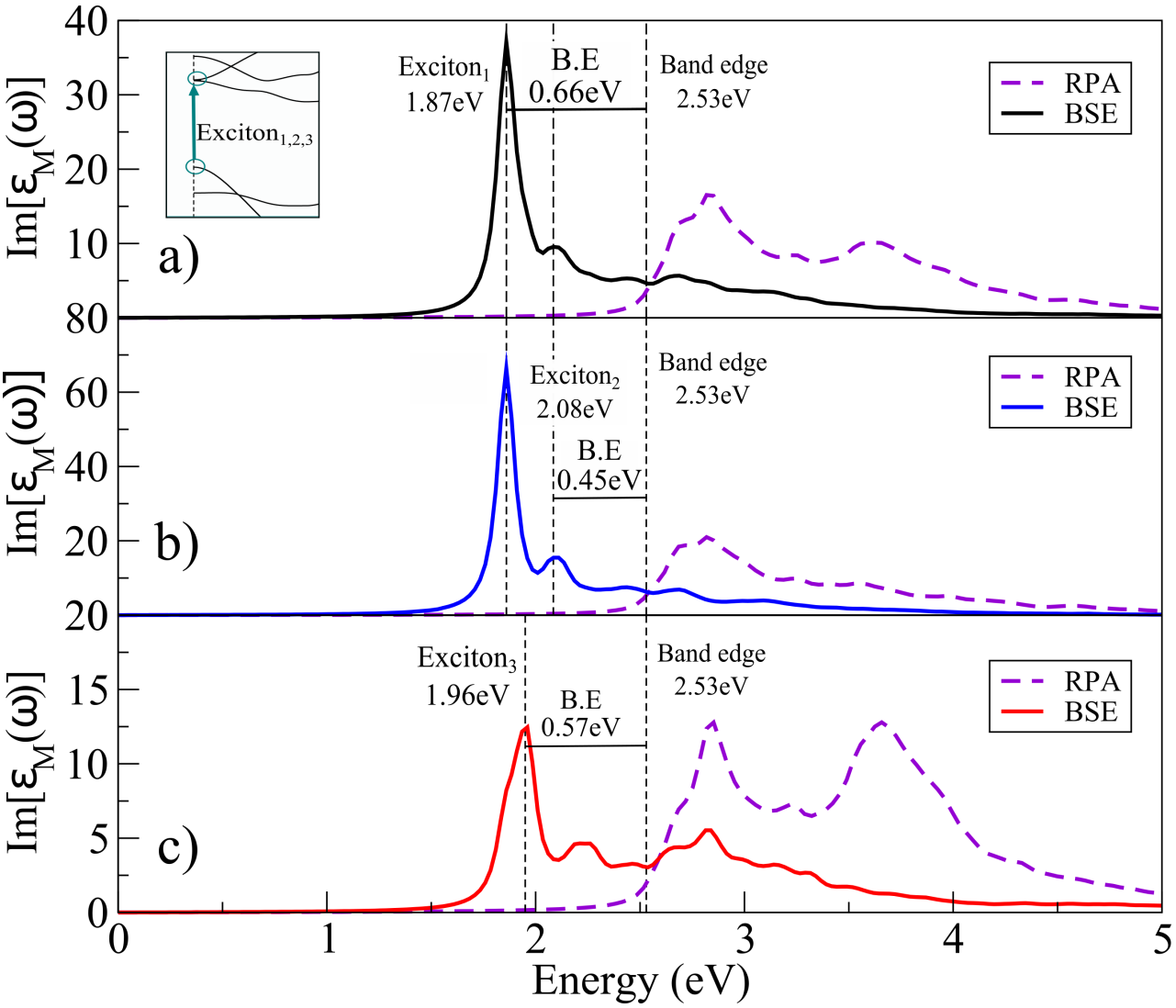

Figure 4.19: Imaginary part of the dielectric constant vs energies for solutions (excitons) on Bethe-Salpeter equation in (a) diagonal , (b) x and (c) y direction for β-Te allotrope. The optical gap of the bright excitons, the band edge of the system and the place where the transition occur are detailed as well.

4.6.3 β-Te with Spin Orbit Coupling

Figures 4.20 and 4.21 show the three level of theories: IPA, RPA and BSE for x and y directions of light polarization in the presence of SOC (spin orbit coupling); figure 4.22 compare the BSE for diagonal (d), x (ZZ) and y (AC) directions; and, figure 4.23 compare the BSE spectra for SOC and non-SOC cases. The independent particle approximation (IPA) shows two peaks located at 1.60 eV and 1.80 eV for the x direction, and 1.80 eV and 2.52 eV for y direction. Those two peaks at x show the difference from the non-SOC case. Here the splitting of the peak is caused by the additional index in the band structure due to the spin. At the RPA level of theory, we see the usual right shift for the spectra in contrast to the IPA due to the Hartree term inclusion. Here, the two peaks located at 2.62 eV and 3.51 eV for x direction have an improved definition. Even more so, the first peak in the IPA (located at 1.80 eV) is divided in two well defined peaks located at 2.62 eV and 2.8 eV. The RPA defines the band edge located at 2.07 eV (which is a good value in comparison to 1.92 eV calculated in [58]). The size of the direct gap was calculated by an approximation considering the previous results on the quasi-particle corrections (GW) from the non-SOC case, *i.e.*, we have taken the QP corrections from the non-SOC case (1.03 eV) and made a rigid shift for the band structure in the presence of SOC (whose direct gap was 1.04 eV), thus resulting in 2.07 eV. In this sense, the solution of Bethe Salpeter equation gives three notable peaks in the ZZ direction with energies of $E_1 = 1.45\ eV$, $E_4 = 1.66\ eV$ and $E_5 = 1.85\ eV$; and, two well defined peaks in the AC direction with energies $E_6 = 1.74\ eV$ and $E_7 = 1.93\ eV$ (see figures 4.20 and 4.21).

Here, we appreciate that the intensity in the x direction is twice the one in y, and that peaks are located at almost the same position to the non-SOC case. Thus, the anisotropy at the BSE level is just noticeable for the first exciton ($E_1 = 1.45\ eV$) and, when comparing intensities. The BSE results in the diagonal direction (see figure 4.22) clearly show three excitonic states located at $E_1 = 1.45\ eV$ (exciton 1), $E_2 = 1.70\ eV$ (exciton 2) and $E_3 = 1.88\ eV$ (exciton 3). Exciton 1 comes fully from x direction contribution, while exciton 2 and 3 are composed by the contributions from E_4 and E_6, and E_5 and E_7 respectively. Those excitonic states have binding energies (red solid lines in figure 4.24-b) corresponding to 0.62 eV (exciton 1), 0.37 eV (exciton 2) and 0.19 eV (exciton 3) and occur from transitions from vb1 to cb1 in the vicinity of the Γ point (see figure 4.16), where the direct gap is located. In this case, the flip in the curvature of the band and the separation between the two nearest conduction bands due to the SOC inclusion causes the suppression of transitions from vb1 to cb2. So, in this case, The three brightest excitons are s states, *i.e.*, excitons 1 is 1s, exciton 2 is 2s and exciton 3 is 3s in character. On the other hand, the dark excitons (see the red dashed lines in figure 4.24-b), which are solutions of the BS equation with zero intensity (not appearing in bse spectra) are located at 1.61 eV, 1.70 eV and 1.82 eV with binding energies of 0.46 eV, 0.37 eV and 0.25 eV respectively.

In conclusion, the SOC causes the BSE spectra of our β-Te phase to move to the left (due

to the reduction in size of the direct gap), an splitting of the peaks (due to the additional index of the spin) and lowers the intensity of the peaks in the zigzag and diagonal light polarization direction (since the armchair direction is almost constant) (see figure 4.23).

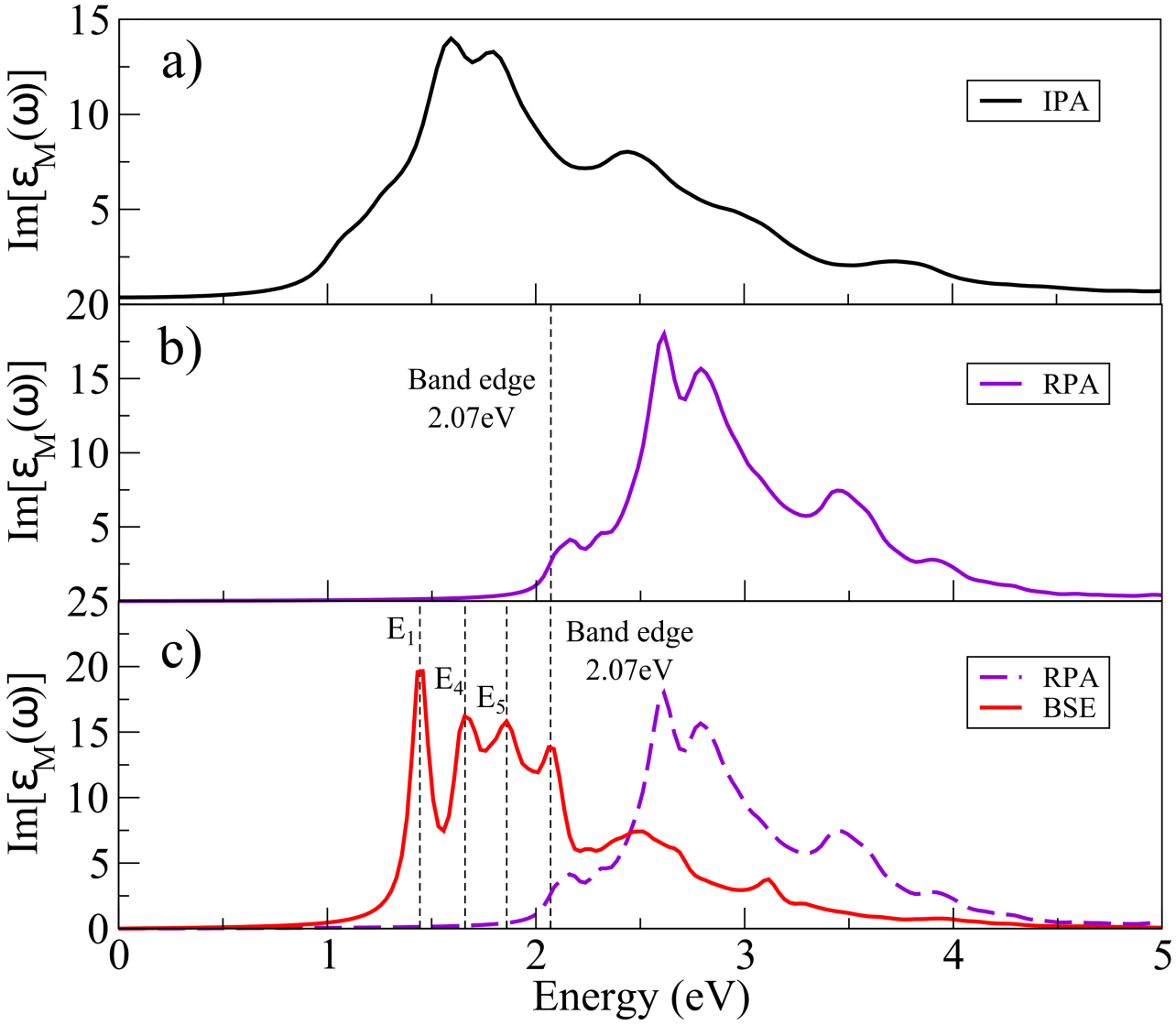

Figure 4.20: Imaginary part of the dielectric constant vs energies for different levels of theory: (a) IPA, (b) GW-RPA and (c) GW-BSE for light polarized in the zigzag(x) direction for β-Te allotrope in the presence of SOC

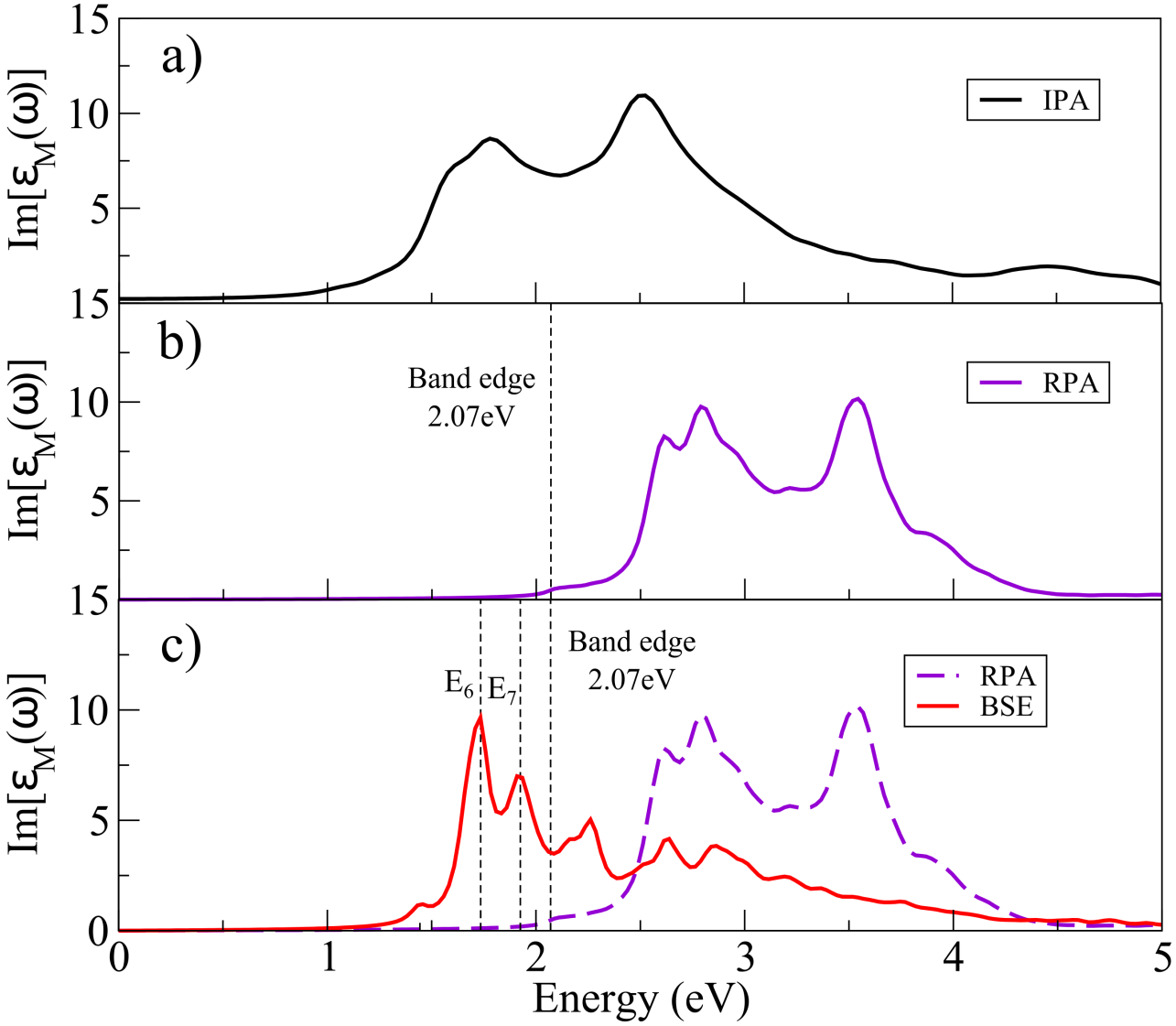

Figure 4.21: Imaginary part of the dielectric constant vs energies for different levels of theory: (a) IPA, (b) GW- RPA and (c) GW-BSE for light polarized in the armchair(y) direction for β-Te allotrope in the presence of SOC

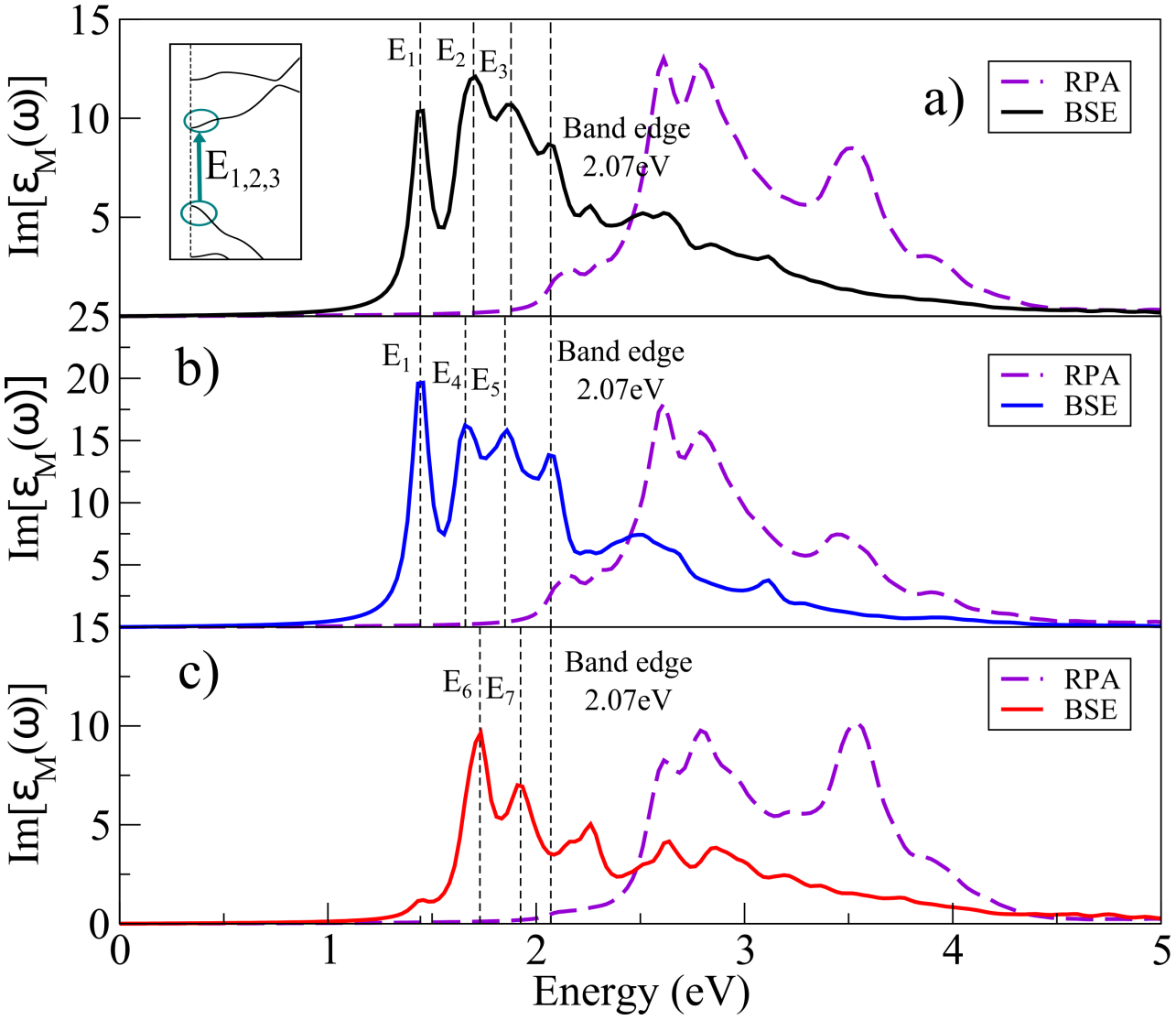

Figure 4.22: Imaginary part of the dielectric constant vs energies for solutions (excitons) on Bethe-Salpeter equation for light polarized in the (a) diagonal , (b) x and (c) y direction for β-Te allotrope in the presence of SOC. The optical gap of the bright excitons, the band edge of the system and the place where the transition occur are detailed as well.

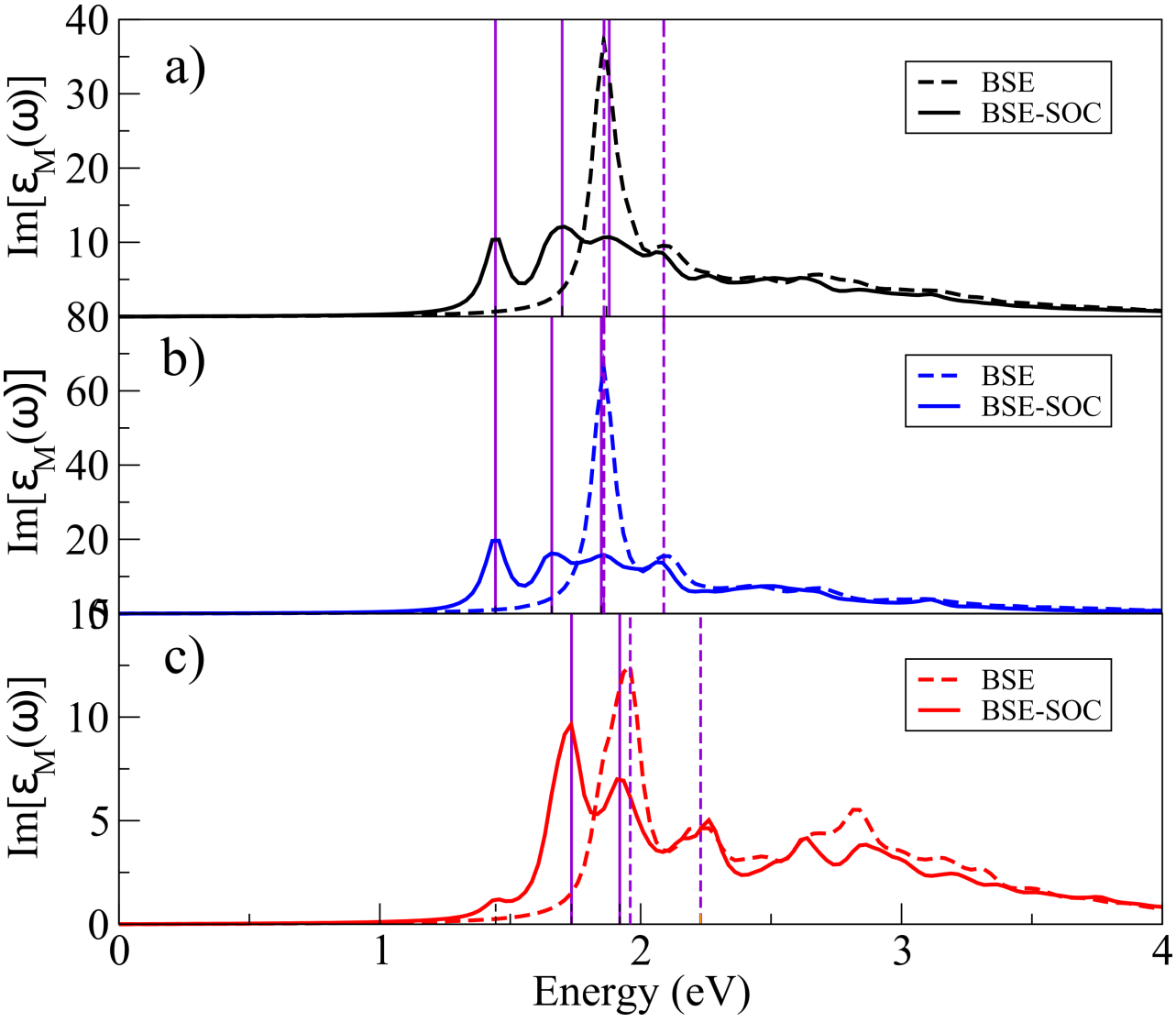

Figure 4.23: BSE comparison for SOC (solid lines) and non-SOC (dashed lines) cases for light polarized in (a) diagonal, (b) x and (c) y for β-Te allotrope. The vertical purple solid (dashed) lines show the peaks for SOC (non-SOC) case.

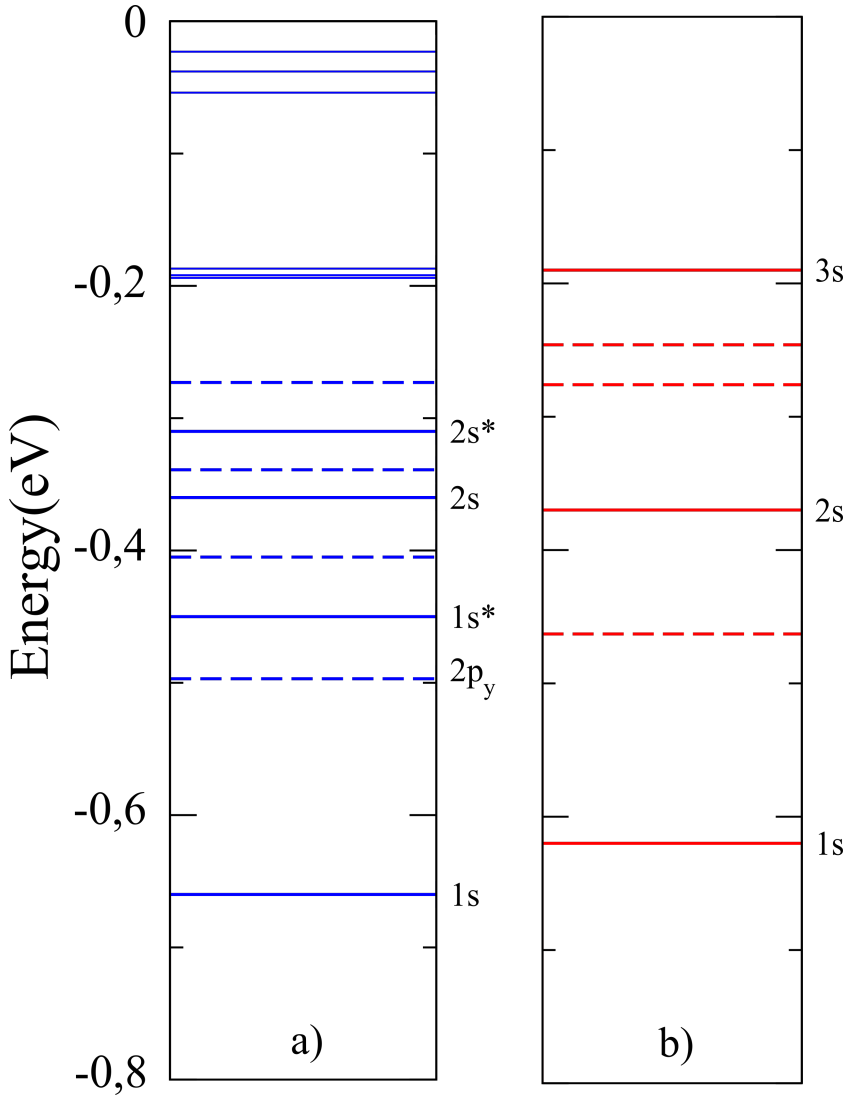

Figure 4.24: Excitonic binding energies comparison between the results on solving the full Bethe-Salpeter equation (a) in the DFT level of theory and (b) in the presence of SOC

4.7 Hydrogenic Model for Excitons

Once we have determined where the transitions occur in the monolayer α-Te and β-Te. We are able to test the hydrogenic model in order to predict the binding energies. So, in this section we will analyze the transitions for α-Te and β-Te with and without SOC. Even though the α-Te allotrope does not present clearly excitons, we can in principle predict binding energies due to the existence of a direct gap in its bandstructure.

4.7.1 Eigenvalues

In the case of α-Te we have identified three possible transitions:

Transitions at Γ

There are two transitions happening at this point, from valence band vb1 and vb2 to cb1; since Γ is symmetric in x/y direction, the reduced masses in each direction are equivalent and with values of $\mu_{x/y}^{\text{vb1}\to\text{cb1}} = 0.17\ m_e$ and $\mu_{x/y}^{\text{vb2}\to\text{cb1}} = 0.08\ m_e$. The computed binding energies with a $\alpha_{2D} = 17.70$ Å are $E_1^{\text{vb1}\to\text{cb1}} = 0.24\ eV$ and $E_1^{\text{vb2}\to\text{cb1}} = 0.20\ eV$ (see figure 4.25-a), and correspond to $1s$-like states as seen in the figure 4.25-b,d.

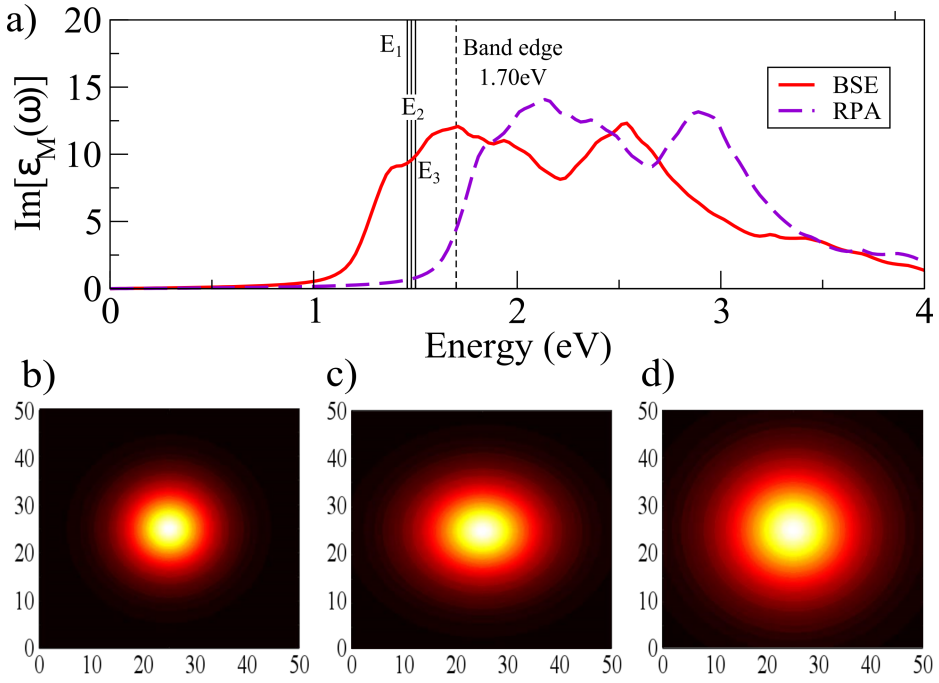

Figure 4.25: (a) Predicted excitonic binding energies $E_1^{\text{vb1}\to\text{cb1}} = E_1 = 0.24\ eV$, $E_1^T = E_2 = 0.22\ eV$ and $E_1^{\text{vb2}\to\text{cb1}} = E_3 = 0.20\ eV$ (black vertical lines) for monolayer α-Te using the hydrogen effective model in comparison with BSE and RPA spectras. Excitonic wave functions for the transitions at Γ and T: (b) $E_1^{\text{vb1}\to\text{cb1}}$, (c) E_1^T and (d) $E_1^{\text{vb2}\to\text{cb1}}$.

Transition at T

It involves bands whose reduced masses are $\mu_x = 0.10\ m_e$ and $\mu_y = 0.16\ m_e$ and 2D polarization of $\alpha_{2D} = 17.70$ Å. The first binding energy calculated trough the Numerov method correspond to a $1s$ state with value of $E_1^T = 0.22\ eV$ (see figure 4.25-a,c).

So, the simple model predicts small exciton binding energies for α-Te allotrope. However, as we have seen in the BSE spectra, this phase does clearly present bound excitons. We conclude that the structure of α-Te is unable to form stable excitons because of the large size of the polarization, but, since it has an small direct gap, the hydrogen model will always predict values for binding energies.

For the β-Te phase we have identified two transitions happening at Γ:

Transition from vb1 to cb1

For this transition, we have the particular case where the conduction band has a negative curvature, for this reason we are considering it negative when computing the reduced masses. They have values of $\mu_x = 0.41\ m_e$ for zigzag direction and $\mu_y = 0.58\ m_e$ for the armchair. With a 2D polarization value equal to the mean of both directions, *i.e.*, $\alpha_{2D} = 6.90$ Å. The computed binding energies are represented in figure 4.26-b. The exciton binding energies of interest correspond to the bright ones colored in black solid lines, the first $1s$ is located at $E_{1s} = 0.63\ eV$, and the $2s$ state at $E_{2s} = 0.33\ eV$. Values which are in good agreement with BSE results (see figure 4.26-a for 1s and 2s blue lines). Furthermore, we recognize dark excitons which are drawn as black dashed lines and correspond to p states. The only comparable state of this kind, with respect to Yambo energies, is the state $2p_y$ which is displaced an amount of 1.1 eV. The remaining bright or dark excitons in the energy range considered here have been characterized according to the probability distribution in analogy to the hydrogen atom wave functions.

Transition from vb1 to cb2

In this case, electron and hole effective masses have values of $\mu_x = 0.08\ m_e$ in the zigzag direction and $\mu_y = 0.26\ m_e$ for armchair. The binding energies are represented with magenta lines in figure 4.26-c where we identify the first two states 1s and 2s labeled with a star $*$, whose values are $E_{1s^*} = 0.45\ eV$ and $E_{2s^*} = 0.20\ eV$. Those energies correspond to the BSE energy states of $1s^*$ and $2s^*$ (see figure 4.26-a); we can see that $1s^*$ state show a good accuracy, while the $2s^*$ state present an error when we compare to the predicted value in the hydrogen model.

In conclusion, the 2D hydrogen model predicts correctly the brightest excitons (*i.e.*, the $1s$, $2s$ and $1s^*$ on figure 4.26-a) in the β-Te phase coming from the solution of Bethe Salpeter

equation. In this particular case, the correct application of the hydrogen model deals with a degeneracy on the conduction band causing the excitonic binding energies to be splitted in two transitions. The first transition predicts correctly states $1s$, $2s$; while, the second transition gives the $1s^*$ state. This reaffirms, one more time, the power of the Hydrogenic model, since it has been previously applied to Phosphorus and TMD's [43, 93, 94, 95] and now to tellurene with good accuracy for predicting exciton formation in monolayer slabs.

For β-Te with SOC we have identified one transition happening at Γ:

Transition from vb1 to cb1

For this transition, we have the reduced masses with values of $\mu_x = 0.13\ m_e$ for zigzag direction and $\mu_y = 0.36\ m_e$ for the armchair. And, a 2D polarization, equal to the mean of both directions, of $\alpha_{2D} = 7.65$ Å. So, the computed binding energies are represented with green lines in the figure 4.27-b. The exciton binding energies of interest correspond to the first three s states: the $1s$ state has a value of $E_{1s} = 0.47\ eV$, the $2s$ state is $E_{2s} = 0.23\ eV$ and the $3s$ state is $E_{3s} = 0.15\ eV$. In this case, this results does not match the excitons obtained with BSE (see figure 4.27-a), the difference is 0.15 eV for the $1s$ state, 0.14 eV for $2s$ and 0.04 eV for $3s$.

So, we can conclude the pure 2D hydrogen model has limitations when trying to predict results from spin orbit coupling calculations. However, this errors could possibly decrease if fine structure terms such as the relativistic (p^4) and spin-orbit ($\vec{\mathbf{L}} \cdot \vec{\mathbf{S}}$) are included in the model. This implementation is left as a future research project.

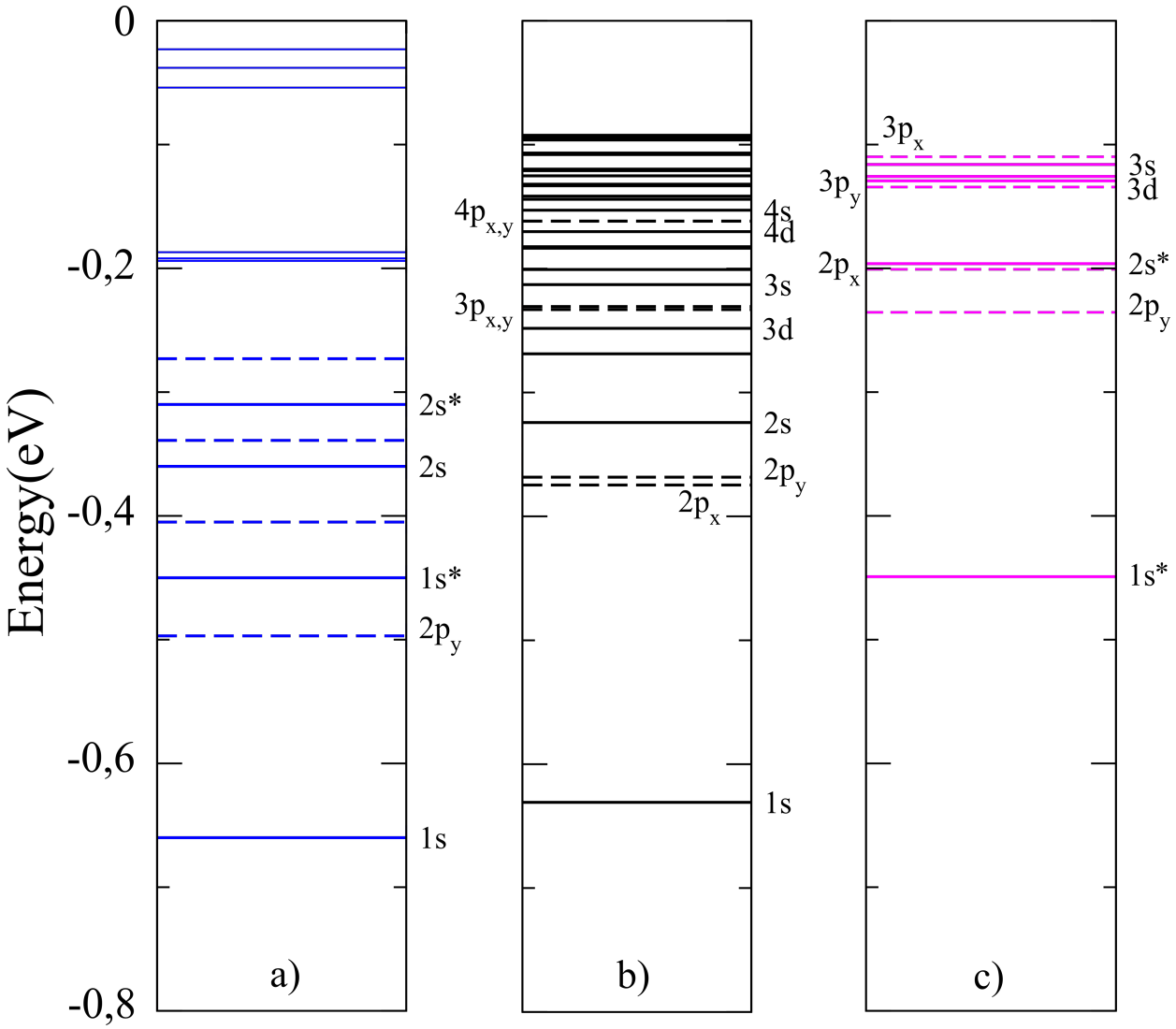

Figure 4.26: Excitonic binding energies comparison between (a) the results on solving the full BS equation with DFT and with the hydrogen model for (b) transition between vb1-cb1, and (c) transition between vb1-cb2.

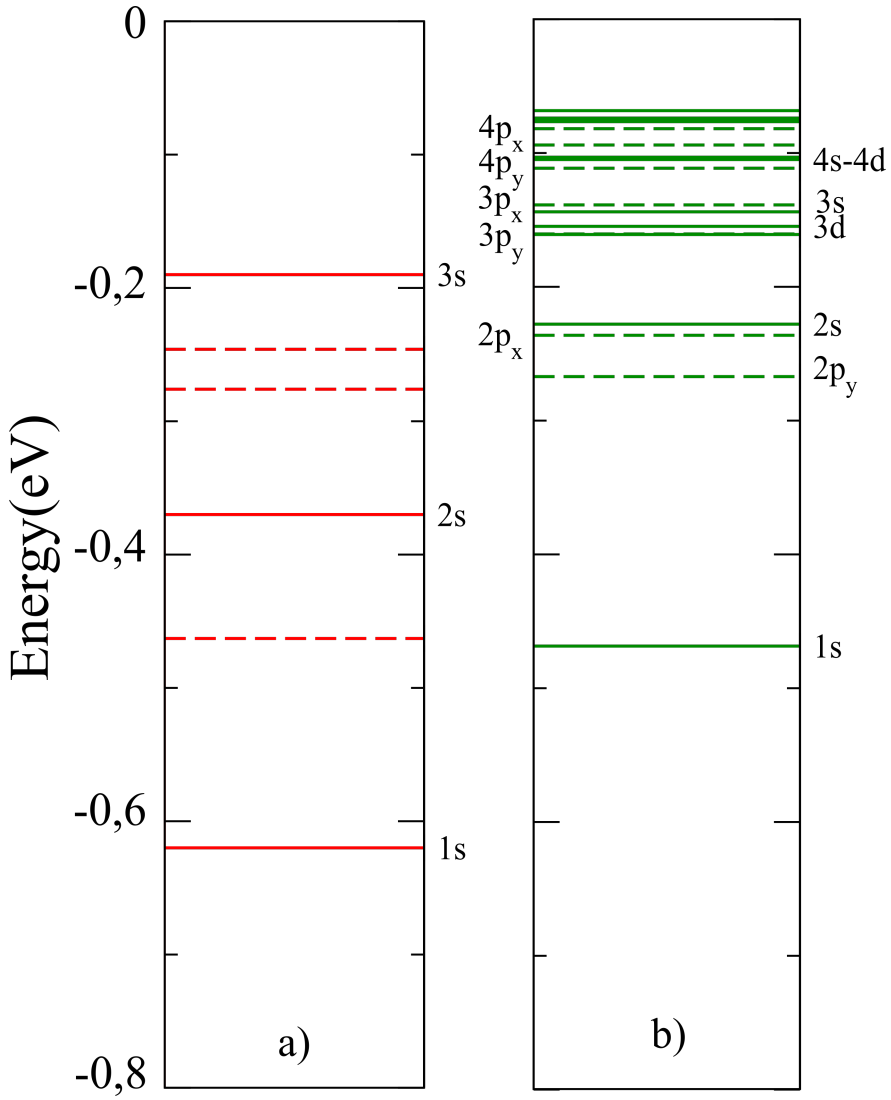

Figure 4.27: Excitonic binding energies comparison between (a) the results on solving the full BS equation in the presence of SOC and (b) with the hydrogen model for transition between vb1-cb1.

4.7.2 Exciton Wavefunctions

Excitonic wave function for β-Te are described in figures 4.28-a-e, where we have selected the five matched states in binding energies between BSE solution and the hydrogen method. Figure 4.28-a,b shows the first two $1s$ states (from the transition vb1 to cb1) and $1s^*$(transition vb1 to cb2) coming from hydrogen model (left figures of 4.28) and BSE (right figures of 4.28); even though the shape of the states correspond to a 1s-like wave function, there is a discrepancy in the size of the radius for the first state. We manage to identify the states $2s$ (transition from vb1 to cb1) and $2s^*$(transition from vb1 to cb2) represented in figure 4.28-c,d, where both the size (70 Å-80 Å) and the shape of the exciton wave function agree between BSE (right) and hydrogen model (left). Lastly, figure 4.28 correspond to a dark exciton which can be identified as a $2p_y$ state. The anisotropy of β-Te does not affect the system significantly, since the effective masses for the first transition (vb1 to cb1) are not so different, so that is why we observe almost spherical wave functions. However, transitions describing $1s^*$ and $2s^*$ (*i.e.*, from vb1 to cb2) show more clear the anisotropy of the system due to a the smaller value of the x-directional effective mass.

In case of β-Te in the presence of spin orbit coupling, the excitonic wave functions for the first and second peaks are represented in figure 4.29, they correspond to the $1s$ and $2s$ states respectively. Since the difference of the directional effective masses is large, we see the deformation in favor of the x direction for the hydrogen model (left figures of 4.29). This shape is identical to the one found in the BSE (right figures of 4.29). Lastly, the size of the wave functions has a difference of 30 Å when both models are compared.

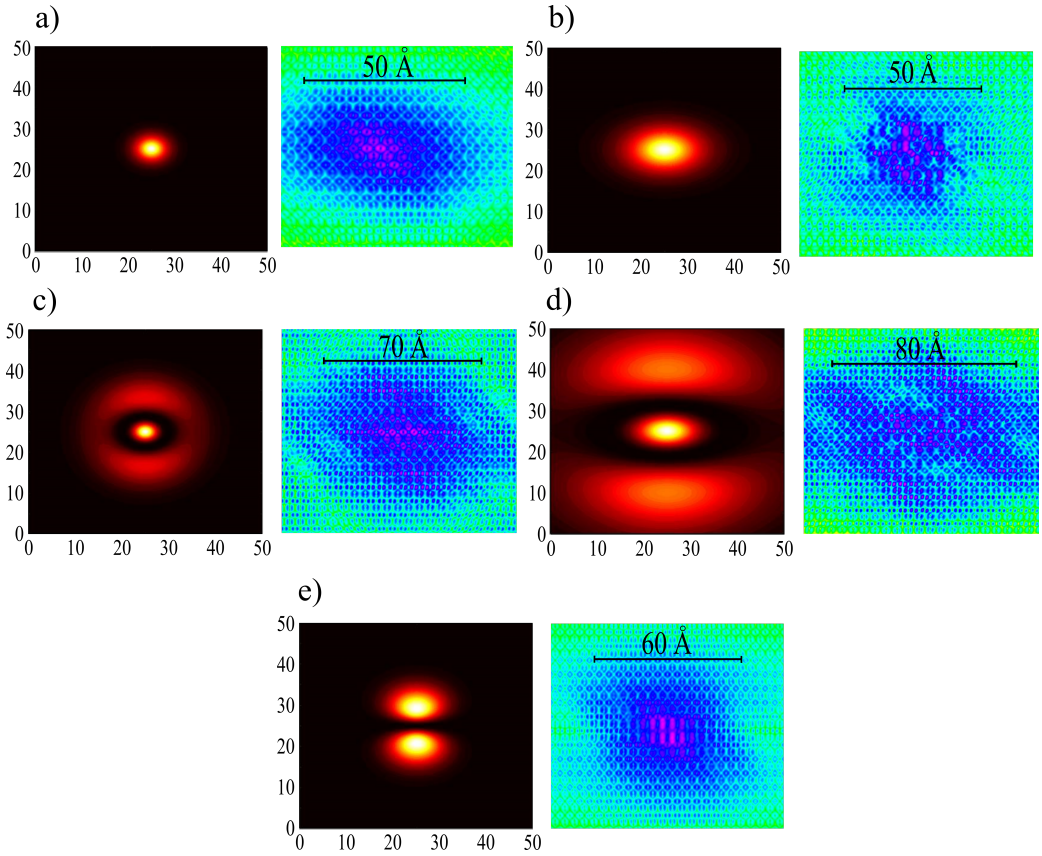

Figure 4.28: Excitonic wavefunctions comparison between hydrogen model(left side with red-hot colors) and BSE (left side with RGB colored) for β-Te. The bright excitons are: (a) correspond to $1s$, (b) is $1s^*$, (c) the $2s$ state and (d) $2s^*$; and dark exciton state printed in (e) for state $2p_y$.

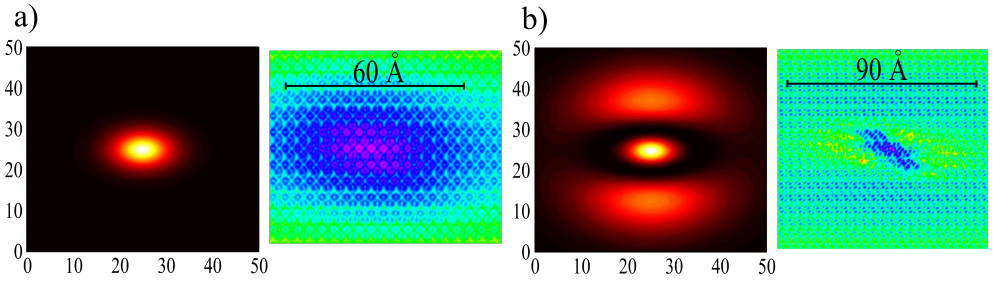

Figure 4.29: Excitonic wavefunctions comparison between hydrogen model(left side with red-hot colors) and BSE (left side with RGB colored) for β-Te with spin-orbit coupling. The bright excitons correspond to (a) $1s$ and (b) $2s$ states.

4.8 Discussion

In summary, the tellurene is a material which can be stabilized in the MoS_2-like (α-Te and γ-Te) and tetragonal (β-Te) structures. In which the formation of α-Te is novel in the history of 2D-materials (the thickness dependent phase transition). The band-structure of these systems show a metallic behavior for γ-Te, while the α-Te and β-Te are semiconductors. Our analysis for the optical properties of tellurene has been applied to the semiconductor phases with and without the inclusion of SOC (the case with SOC just correspond to the β-Te phase, because the α-Te non-SOC gap is actually small, and the inclusion of SOC will just decrease that value). So, the BSE optical spectra was constructed after the calculation of the QP corrections (GWA) for the two phases α-Te and β-Te, while for β-Te with SOC, the QP corrections where included via a rigid shift of the DFT bands. There we can see that the α-Te can not form stable excitons, while β-Te present three bright excitons happening at Γ. These transitions enroll the two first conduction bands due to the contact point formed at Γ. The binding energy of the excitons are 0.66 eV, 0.57 eV and 0.45 eV. The highest and lowest ones correspond to the brightest transition happening when light is polarized in x direction, while the one in the middle ,correspond to y-direction. However, since the excitons at x/y spectras are located at the same position, the x-directional overlaps the y for the diagonal light polarization spectra. In this way, the anisotropy of tellurene is not appreciated in the position of the peaks but in the intensity of them. Lastly, when SOC is turned on, the BSE spectra changes considerably from the non-SOC case, since the direct gap at Γ no longer present the contact point. The first three excitons correspond to states s-likes, where the intensity of the peaks becomes the source of anisotropy. Both results for β-Te, the most stable phase, argument that the tellurene is an excellent monolayer material for development of photovoltaic devices, due to the stable formation of excitons of binding energy of 0.66 eV. What is more, the anisotropy of the system could help in the development of electronic devices that include directional currents.

For the hydrogenic effective model, the effective masses (located at band-structure's places where the transitions happens) and 2D-polarization (calculation of the dielectric constant using phonon calculations) were computed. The model predicts that for α-Te, the excitons should be formed at Γ and T points with an average binding energy of 0.22 eV. For β-Te, the transitions were happening from the valence band, at Γ, to the point where two conduction bands meet. The excitons with highest binding energies correspond to s-like states when compared to hydrogenic wave-functions. Lastly, the SOC case of β-Te establish a binding energies of approximately 0.1 eV difference in compare to the non-SOC case, and ordered the character of principal excitons as s and d-likes states.

Lastly, when both results are compared. We see the first discrepancy for α-Te presence of excitons (in the hydrogen model). This can be explained due to the basis of the model (since it will always predict an energy if a gap is given). On the other hand, for β-Te, the

effective model predicts the three brightest excitons with excellent accuracy for the binding energies, transition places, and shape of the wavefunctions. Thus confirming the power of the hydrogen effective model, which has been previously applied to phosphorus and TMD's. However, when we have analyze the SOC results, we clearly see the limitations of a non-relativistic model. The no inclusion of an spin index nor the kinetic energy corrections in the effective model possibly make the difference in binding energies (even though the shape of wavefunctions matches the BSE results). So, for a fully understand of systems with spin-orbit coupling, a Dirac equation approach in two dimensions should be studied.

Conclusions

Through this thesis, we have talk firstly about the solar cell industry. In view that nowadays photovoltaic industry is currently searching techniques for develop low dimensional systems with better characteristics compared to present photovoltaic devices, the evolution of the solar cell market point towards thin film generation, and new types, such as excitonic solar cells. The mechanism behind the excitonic solar cell lead us to the well-known quasi-particle called as exciton, which, is composed by an electron-hole pair, similar to a hydrogenic atom. To study the properties of this excitons, it is necessary to decrease the dimensions of the system up to a few Angstroms (Å), and so fall in the world of nano-technology. Specifically, we focus on two-dimensional materials, the monolayers, which are one of the best systems to boost the exciton solar cell market due to the fact that they can harbor stable excitons (high binding energy excitons). Some representative examples in the literature are the TMD's, phosphorus, and, our subject of study, tellurene (monolayer of tellurium). In this sense, we start exploring the characteristics of Tellurium, and arrive to the quick conclusion that its production and cost are not the ideal ones for a market. However, tellurium can be overcome this, if new government politics are implemented, or by creating the necessity to acquire this new type of technology.

Since our main purpose is to understand the optical properties (excitonic formation) of tellurene. We firstly present the theoretical background for it in chapter 2. There, we start with the DFT theory, which has its bases on Hohenberg-Kohn theorems and a solution thanks to Kohn and Sham (KS). Where the KS solution help us to determine the energy levels and the wave-functions (band-structure). In addition, one could develop a time dependent DFT theory, which has its bases on Runge-Gross theorem, and predict the optical properties of the system, thanks to the calculation of the dielectric constant in the independent particle approximation (IPA) and random phase transition (RPA). However, despite the success of DFT, the DFT band-structure present errors due to the absence of quasi-particle (QP) interactions in the theory. This problem is solved thanks to Green functions, Hedin's equations and the GW approximation. Where the later uses the screened interaction in the plasmon-pole approximation, and the wave functions calculated from KS band-structure. In some cases the QP corrections just causes a rigid shift on the DFT band-structure (*e.g.* β-Te with and without SOC), and in others the changes are substantial (*e.g.* α-Te). The QP corrections make possible the calculation, by using TDDFT, of the GW-IPA and GW-RPA absorption spectras, and so, going closer to experimental results. However, there are some materials with large gaps, such as semiconductors or insulators, where it is necessary to include electron-hole (exciton) correlations through the Bethe-Salpeter equation (BSE). Finally, once BSE is solved, it gives us the correct absorption spectra, and also information of the binding

energies (when is compared to the band edge at the beginning of the GW-RPA) and wave-functions of the excitons.

As we have seen, the theory behind the BSE optical spectra deals with several previous calculations, which in combination with the several sums (for example the ones appearing in the screened interaction, the RPA or the GWA) make the computation too expensive. For this reason, we search an effective theory, in chapter 3, that give us partially the same information of the original system. The quantities of interest, in our case, are the ones related with excitons, such as binding energy and the wave function. So, the effective model should be based on excitons inside a two-dimensional material. This system can be approximated to a hydrogenic atom (exciton) moving in an effective potential (modeled as a sheet). The potential is constructed in terms of the Struve and Bessel functions, and is approximated to the Keldysh interaction. And, we also can have anisotropic solutions (with respect to the two-dimensional polarization α_{2D}) whose can be approximated as well to the Keldysh potential but with an average α_{2D} for x/y directions. What is more, since we are modeling a particle conformed by an electron and hole, the effective masses of them are mandatory. Those are extracted from the curvature of the valence and conduction band at points where the transition happen. Finally, The two-dimensional Schrodinger equation for the system can be isotropic or anisotropic depending on the directional effective masses. In both cases, they can be solved by the Numerov method, linear in the isotropic case and matrix for the anisotropic one. The results arising from this differential equation give us the energy levels and wave-functions of excitons.

The last chapter compare both excitonic results arising from the full BSE solution and the hydrogen like model. However, before we analyze the optical characteristics of tellurene, we focus on the structural and electronic properties in order to have a complete description of this monolayer. The tellurene, the two-dimensional material coming from the semiconductor tellurium (bulk-Te), present three phases: α-Te, β-Te y γ-Te. The α-Te introduces a new formation process known as thickness-dependent phase transition, while the natural most stable phase β-Te is obtained through exfoliation in the z^{th} direction. The band-structure show that both phases α-Te and β-Te are semiconductor, while the γ-Te behaves like a metal. In the same sense, the band-structure in the presence of SOC causes an splitting of contact points in the bands, a decrease in the size of the gap, and an inversion in the curvature of the valence band and conduction band for α-Te and β-Te respectively. On the other hand, the density of states, in any of the three phases, show a global contribution arising from p states. Our cases of study are reduced to the transitions in α-Te, which occur in the Γ and T points, in β-Te, which happen at Γ, and in β-Te + SOC, which occur at Γ as well. In what respect to the effective masses of valence and conduction bands, α-Te is isotropic, while the β-Te y β-Te + SOC show anisotropic behavior due to their rectangular IBZ. What is more, for the polarization constant, we found anisotropy for β-Te with or without SOC, and, a high value, almost the double from β-Te, for α-Te phase. When the QP corrections are performed, the

band-structures in the case of α-Te, make a change in the gap positions and causes several elevations throughout the trajectories of the DFT bands. On the other hand, for β-Te, we have a rigid shift. This fact encourage us to take the GW corrections to the β-Te + SOC as a rigid shift as well.

Lastly, for the optical properties, the BSE spectra results show that the α-Te does not present excitons, the BSE only makes a shift to the left in comparison to the GW-RPA; while on β-Te phase, we have an strong presence of excitonic peaks with optical gaps of 1.87 eV for the zz direction (x) and 1.96 eV for ac direction (y). The sum of this contributions in the diagonal direction show that the x direction is predominant in intensity (thus confirming, one more time, the anisotropic character of β-Te), thus, resulting in two excitons located at 1.87 eV and 2.08 eV with binding energies of 0.66 eV and 0.45 eV respectively. In what respect to the SOC case, it is notorious that in each level of theory (IPA, RPA and BSE), we observe the characteristic splitting due to the inclusion of the new degree of freedom, the spin. In this way, we have three prominent excitons before the band edge located at 1.45 eV, 1.70 eV y 1.88 eV with binding energies of 0.62 eV, 0.37 eV y 0.19 eV respectively. On the other hand, the hydrogen effective model applied to the α-Te phase predicts a binding energy of the order of 0.2 eV due to its great 2D-polarization constant. However, when is compared to the BSE spectra, we observe that no excitons exist in this phase. This discrepancy is due to the fact that the consideration of the gap is always present in the simple model, thus, a value will always be given to the binding energy. In the case of β-Te, the model works perfectly, it predicts the values of 0.63 eV y 0.45 eV for the first two excitonic peaks which corresponds to $1s$ and $1s^*$ states; what is more, it predicts the state $2s$ with an energy of 0.33 eV. Thus, confirming the power of the hydrogen effective model whose has previously been applied to TMD's and phosphorus. Lastly, the binding energies predictions in the case of β-Te with SOC does not match with the provided by BSE. This is due, perhaps, to the no inclusion of relativistic terms and spin-orbit coupling. However, it is left as a future research project to analyze the contributions and impact of this terms in the 2D hydrogenic model. In addition, the excitonic wave-functions formed in β-Te for our cases of interest $1s$, $1s^*$, $2s$ and $2s^*$ show a great similarity in shape to the ones obtained in the BSE calculation; however, there is a difference in scale for the cases with lowest binding energies $1s$ y $1s^*$.

Finally, the results show that one of our materials of study, the β-tellurene, is an excellent material to host stable excitons of the order of 0.65 eV similar to the ones found in TMD's and phosphorus. For this reason, we can firmly say that β-Te is a tentative candidate for photovoltaic technology. Even more, thanks to its anisotropic character, electronic devices operating with directional currents can be developed.

Bibliography

[1] Askari Mohammad Bagher, Mirzaei Mahmoud Abadi Vahid, and Mirhabibi Mohsen. Types of solar cells and application. *American Journal of Optics and Photonics*, 3(5):94–113, 08 2015.

[2] A. Jäger Waldau. Jrc science for policy report, pv status report 2017. *Publications Office of the European Union*, 03 2018. Available at "https://ec.europa.eu/jrc/en/publication/eur-scientific-and-technical-research-reports/pv-status-report-2017".

[3] Simon Philipps. Photovoltaics report. Technical report, Fraunhofer ISE and Werner Warmuth, PSE Conferences & Consulting GmbH, 03 2019. Available at "https://www.ise.fraunhofer.de/en/publications/studies/photovoltaics-report.html".

[4] B. Gregg. The photoconversion mechanism of excitonic solar cells. *MRS Bulletin*, 30(1):20–22, 01 2005.

[5] Jun Xiao, Mervin Zhao, Yuan Wang, and Xiang Zhang. Excitons in atomically thin 2d semiconductors and their applications. *Nanophotonics*, 6(6):1309–1328, 12 2016.

[6] Masayasu Ueta, Hiroshi Kanzaki, Koichi Kobayashi, Yutaka Toyozawa, and Eiichi Hanamura. *Excitonic Processes in Solids*, volume 60. Springer-Verlag Berlin Heidelberg, 1986. [Sections 1 and 6].

[7] J. Frenkel. On the transformation of light into heat in solids I. *Physical Review*, 37(1):17–44, 01 1931.

[8] Gregory H. Wannier. The structure of electronic excitation levels in insulating crystals. *Phys. Rev.*, 52(3):191–197, 08 1937.

[9] Peter Yu and Manuel Cardona. *Fundamentals of Semiconductors. Physics and Materials Properties*. Springer-Verlag Berlin Heidelberg, 4th edition, 04 2010. [Section 6.3].

[10] G. Dresselhaus. Effective mass approximation for excitons. *Journal of Physics and Chemistry of Solids*, 1(1):14–22, 05 1956.

[11] Donald I. Bleiwas. Byproduct mineral commodities used for the production of photovoltaic cells. Technical report, U.S. Geological Survey Circular 1365, 10p, 12 2010. Available at "https://pubs.usgs.gov/circ/1365/".

[12] Assoc. Prof. Muhammet S. Toprak. Introduction to nanotechnology, 2014. [Presentation].

[13] Syeda Amber Yousaf and Salamat Ali. Why nanoscience and nanotechnology? what is there for us? *Journal of Faculty of Engineering & Technnology*, pages 11–20, 04 2019.

[14] Scientific background on the nobel prize in physics 2010, graphene. "https://www.nobelprize.org/prizes/physics/2010/press-release/", 10 2010. [compiled by the Class for Physics of the Royal Swedish Academy of Sciences].

[15] Bo Peng, Hao Zhang, Hezhu Shao, Yuanfeng Xu, Rongjun Zhang, and Heyuan Zhu. Electronic, optical, and thermodynamic properties of borophene from first-principle calculations. *J. Mater. Chem. C*, 4(16):3592–3598, 01 2016.

[16] Emilio Scalise, Michel Houssa, Geoffrey Pourtois, B. van den Broek, Valery Afanas'ev, and André Stesmans. Vibrational properties of silicene and germanene. *Nano Research*, 6(1):19–28, 01 2013.

[17] Xiaodong Li, Jeffrey T. Mullen, Zhenghe Jin, Kostyantyn M. Borysenko, M. Buongiorno Nardelli, and Ki Wook Kim. Intrinsic electrical transport properties of monolayer silicene and MoS_2 from first principles. *Phys. Rev. B*, 87(11):115418, 03 2013.

[18] Liangzhi Kou, Changfeng Chen, and Sean C. Smith. Phosphorene: Fabrication, properties and applications. *The Journal of Physical Chemistry Letters*, 6(14):2794–2805, 06 2015.

[19] Feng-feng Zhu, Wei-jiong Chen, Yong Xu, Chun-lei Gao, Dan-dan Guan, Can-hua Liu, Dong Qian, Shou-Cheng Zhang, and Jin-feng Jia. Epitaxial growth of two-dimensional stanene. *Nature Materials*, 14:1020–1025, 08 2015.

[20] Martin Pumera and Zdenek Sofer. 2d monoelemental arsenene, antimonene, and bismuthene: Beyond black phosphorus. *Advanced Materials*, 29(21):1605299, 02 2017.

[21] R Mansfield and S A Salam. Electrical properties of molybdenite. *Proceedings of the Physical Society. Section B*, 66(5):377–385, 05 1953.

[22] Michael Ashton, Joshua Paul, Susan B. Sinnott, and Richard G. Hennig. Topology-scaling identification of layered solids and stable exfoliated 2d material. *Phys. Rev. Lett*, 118(10):106101, 03 2017.

[23] Judah Ginsberg. The discovery of fullerenes. Available at "www.acs.org/content/acs/en/education/whatischemistry/landmarks/fullerenes.html", 10 2010. [accessed 08,2018].

[24] Amila Samarabandu. The greatness of graphene. Available at "surrealsciencestuff.wordpress.com/2015/08/14/the-greatness-of-graphene/", 08 2015. [accessed 07,2018].

[25] J. J Güttinger, F. Molitor, C. Stampfer, S. Schnez, A. Jacobsen, S. Dröscher, T. Ihn, and K. Ensslin. Transport through graphene quantum dots. *Reports on Progress in Physics*, 75(12):126502+, 12 2012.

[26] Zuoli He and Wenxiu Que. Molybdenum disulfide nanomaterials: Structures, properties, synthesis and recent progress on hydrogen evolution reaction. *Applied Materials Today*, 3(2352-9407):23–56, 06 2016.

[27] Andrea Splendiani, Liang Sun, Yuanbo Zhang, Tianshu Li, Jonghwan Kim, Chi-Yung Chim, Giulia Galli, and Feng Wang. Emerging photoluminescence in monolayer MoS_2. *Nano Letters*, 10(4):1271–1275, 2010.

[28] B. RadiBrivio, J. savljevic, A. Radenovic, J. Brivio, V. Giacometti, and A. Kis. Single-layer MoS_2 transistors. *Nature Nanotechnology*, 6:147–150, 01 2011.

[29] Oriol Lopez-Sanchez, Dominik Lembke, Metin Kayci, Aleksandra Radenovic, and Andras Kis. Ultrasensitive photodetectors based on monolayer MoS_2. *Nature Nanotechnology*, 8:497–501, 06 2013.

[30] Ting Cao, Gang Wang, Wenpeng Han, Huiqi Ye, Chuanrui Zhu, Junren Shi, Qian Niu, Pingheng Tan, Enge Wang, Baoli Liu, and Ji Feng. Valley-selective circular dichroism of monolayer molybdenum disulphide. *Nature Communications*, 3(887), 06 2012.

[31] Kin Fai Mak, Keliang He, Jie Shan, and Tony F. Heinz. Control of valley polarization in monolayer MoS_2 by optical helicity. *Nature Nanotechnology*, 7:494–498, 06 2012.

[32] Hualing Zeng, Junfeng Dai, Wang Yao, Di Xiao, and Xiaodong Cui. Valley polarization in MoS_2 monolayers by optical pumping. *Nature Nanotechnology*, 7:490–493, 06 2012.

[33] J. A. Reyes-Retana and F. Cervantes-Sodi. Spin orbital effects in metal dichalcogenide semiconducting monolayers. *Scientific Reports*, 6(24093), 04 2016.

[34] H.J. Chen, J Huang, X.L. Lei, Musheng wu, G Liu, Chuying Ouyang, and bo xu. Adsorption and diffusion of lithium on MoS_2 monolayer: The role of strain and concentration. *International Journal of Electrochemical Science*, 8(2):2196–2203, 02 2013.

[35] Ashwin Ramasubramaniam. Large excitonic effects in monolayers of molybdenum and tugsten dichalcogenides. *Phys. Rev. B*, 86(11):115409, 09 2012.

[36] Mandana Safari, Zohreh Izadi, Jaafar Jalilian, Iftikhar Ahmad, and Saeid Jalali-Asadabadi. Metal mono-chalcogenides ZnX and CdX (X=S, Se and Te) monolayers: Chemical bond and optical interband transitions by first principles calculations. *Physics Letters A*, 381(0375-9601):663–670, 11 2017.

[37] Si Zhou, Cheng-Cheng Liu, Jijun Zhao, and Yugui Yao. Monolayer group-III monochalcogenides by oxigen functionalization: a promising class of two-dimensional topological insulators. *npj Quantum Materials*, 3(16), 03 2018.

[38] Ruixiang Fei, Wenbin Li, Ju Li, and Li Yang. Giant piezoelectricity of monolayer group IV monochalcogenides: Snse, gese and ges. *Applied Physics Letters*, 107(17):173104, 10 2015.

[39] Kai Cheng, Yu Guo, Nannan Han, Yan Su, Junfeng Zhang, and Jijun Zhao. Lateral heterostructures of monolayer group-IV monochalcogenides: band alignment and electronic properties. *J. Mater. Chem. C*, 5(15):3788–3795, 03 2017.

[40] Lidia C. Gomes, P. E. Trevisanutto, A. Carvalho, A. S. Rodin, and A. H. Castro Neto. Strongly bound Mott-Wannier excitons in GeS and GeSe monolayers. *Phys. Rev. B*, 94(15):155428, 10 2016.

[41] Hamad Rahman Jappor and Majeed Ali Habeeb. Optical properties of two-dimensional gas and gase monolayers. *Physica E: Low-dimensional Systems and Nanostructures*, 101(1386-9477):251–255, 07 2018.

[42] Houlong L. Zhuang and Richard G. Hennig. Single-layer group-III monochalcogenide photocatalysts for water splitting. *Chemistry of Materials*, 25(15):3232–3238, 07 2013.

[43] Cesar E. P. Villegas, A. S. Rodin, Alexandra Carvalho, and A. R. Rocha. Two-dimensional exciton properties in monolayer semiconducting phosphorus allotropes. *Phys. Chem. Chem. Phys.*, 18(40):27829–27836, 08 2016.

[44] S. Appalakondaiah, G. Vaitheeswaran, S. Lebégue, N. E. Christensen, and A. Svane. Effect of Van der Waals interactions on the structural and elastic properties of black phosphorus. *Phys. Rev B*, 86(3):035105, 07 2012.

[45] Likai Li, Yijun Yu, Guo Jun Ye, Qingqin Ge, Xuedong Ou, Hua Wu, Donglai Feng, Xian Hui Chen, and Yuanbo Zhang. Black phosphorus field-effect transistors. *Nature Nanotechnology*, 9:372–377, 03 2014.

[46] Han Liu, Adam T. Neal, Zhen Zhu, Zhe Luo, Xianfan Xu, David Tománek, and Peide D. Ye. Phosphorene: An unexplored 2d semiconductor with a high hole mobility. *ACS Nano*, 8(4):4033–4041, 2014.

[47] Yuehua Xu, Jun Dai, and Xiao Cheng Zeng. Electron-transport properties of few-layer black phosphorus. *The Journal of Physical Chemistry Letters*, 6(11):1996–2002, 2015.

[48] Guangzhao Qin, Qing-Bo Yan, Zhenzhen Qin, Sheng-Ying Yue, Hui-Juan Cui, Qing-Rong Zheng, and Gang Su. Hinge-like structure induced unusual properties of black

phosphorus and new strategies to improve the thermoelectric performance. *Scientific Reports*, 4(6946), 11 2014.

[49] Qun Wei and Xihong Peng. Superior mechanical flexibility of phosphorene and few-layer black phosphorus. *Applied Physics Letters*, 104(25):251915, 2014.

[50] Luqing Wang, Alex Kutana, Xiaolong Zou, and Boris I Yakobson. Electro-mechanical anisotropy of phosphorene. *Nanoscale*, 7(21):9746–9751, 2015.

[51] Jin-Wu Jiang and Harold S. Park. Negative poisson's ratio in single-layer black phosphorus. *Nature Communications*, 5(4727), 08 2014.

[52] Yuanchang Li and Xiaobin Chen. Dirac fermions in blue-phosphorus. *2D Materials*, 1(3):031002, 12 2014.

[53] Zhili Zhu, Xiaolin Cai, Seho Yi, Jinglei Chen, Yawei Dai, Chunyao Niu, Zhengxiao Guo, Maohai Xie, Feng Liu, Jun-Hyung Cho, Yu Jia, and Zhenyu Zhang. Multivalency-driven formation of te-based monolayer materials: A combined first-principles and experimental study. *Phys. Rev. Lett.*, 119(10):106101, 09 2017.

[54] Zhili Zhu. Supplemental online material for multivalency-driven ormationn of te-based monolayer materials: a combined first-principles and experimental study.

[55] Jingsi Qiao, Yuhao Pan, Feng Yang, Cong Wang, Yang Chai, and Wei Ji. Few-layer tellurium: one-dimensional-like layered elementary semiconductor with striking physical properties. *Science Bulletin*, 63(2095-9273):159–168, 2018.

[56] Sitansh Sharma, Nirpendra Singh, and Udo Schwingenschlögl. Two-dimensional tellurene as excellent thermoelectric material. *ACS Applied Energy Materials*, 1(5):1950–1954, 2018.

[57] Xiao Hua Wang, Da Wei Wang, Ai Jun Yang, Nikhil Koratkar, Ji Feng Chu, Pin Lei Lv, and Ming Zhe Rong. Effects on adatom and gas molecule adsorption on the physical properties of tellurene: a first principles investigation. *Phys. Chem. Chem. Phys*, 20(6):4058–4066, 2018.

[58] Yuanyuan Pan, Shiyuan Gao, Li Yang, and Jing Lu. Dependence of excited-state properties of tellurium on dimensionality: From bulk to two dimensions to one dimensions. *Phys. Rev. B*, 98(8):085135, 08 2018.

[59] Matin Amani, Chaoliang Tan, George Zhang, Chunsong Zhao, James Bullock, Xiaohui Song, Hyungjin Kim, Vivek Raj Shrestha, Yang Gao, Kenneth B. Crozier, Mary Scott, and Ali Javey. Solution-synthesized high-mobility tellurium nanoflakes for short-wave infrared photodetectors. *ACS Nano*, 12(7):7253–7263, 2018.

[60] Hugh O. H. "Churchill, Gregory J. Salamo, Shui-Qing Yu, Takayuki Hironaka, Xian Hu, Jeb Stacy, and Ishiang Shih. Toward single atom chains with exfoliated tellurium. *Nanoscale Research Letters*, 12(1):488, 2017.

[61] Xiaochun Huang, Jiaqi Guan, Zijian Lin, Bing Liu, Shuya Xing, Weihua Wang, and Jiandong Guo. Epitaxial growth and band structure of te film on graphene. *Nano Letters*, 17(8):4619–4623, 2017.

[62] B. Ydri. *Computational Physics: An Introduction to Monte Carlo Simulations of Matrix Field Theory*. 03 2016. [hep-lat/1506.02567].

[63] Klaus Capelle. A bird's-eye view of density-functional theory. *Brazilian Journal of Physics*, 36(0103-9733):1318–1343, 12 2006. DOI: 10.1590/S0103-97332006000700035.

[64] Judith Harl. *The linear response function in density functional theory: Optical spectra and improved description of the electron correlation*. PhD thesis, University of Vienna, faculty of physics, 10 2008. [Chapter 4].

[65] Stefan Kurth. Introduction to Green functions, the GW approximation, and the Bethe-Salpeter equation. [Presentation].

[66] Jose M Soler. The siesta method for ab initio order-n materials simulation. *Journal of Physics: Condensed Matter*, 14(11):2745–2779, 03 2002.

[67] Paolo Giannozzi, Stefano Baroni, Nicola Bonini, Matteo Calandra, Roberto Car, Carlo Cavazzoni, Davide Ceresoli, Guido L Chiarotti, Matteo Cococcioni, Ismaila Dabo, Andrea Dal Corso, Stefano de Gironcoli, Stefano Fabris, Guido Fratesi, Ralph Gebauer, Uwe Gerstmann, Christos Gougoussis, Anton Kokalj, Michele Lazzeri, Layla Martin-Samos, Nicola Marzari, Francesco Mauri, Riccardo Mazzarello, Stefano Paolini, Alfredo Pasquarello, Lorenzo Paulatto, Carlo Sbraccia, Sandro Scandolo, Gabriele Sclauzero, Ari P Seitsonen, Alexander Smogunov, Paolo Umari, and Renata M Wentzcovitch. Quantum espresso: a modular and open-source software project for quantum simulations of materials. *Journal of Physics: Condensed Matter*, 21(39):395502, 09 2009.

[68] Jack Deslippe, Georgy Samsonidze, David A. Strubbe, Manish Jain, Marvin L. Cohen, and Steven G. Louie. Berkeleygw: A massively parallel computer package for the calculation of the quasiparticle and optical properties of materials and nanostructures. *Computer Physics Communications*, 183(6):1269–1289, 06 2012.

[69] Andrea Marini, Conor Hogan, Myrta Gruening, and Daniele Varsano. yambo: An ab initio tool for excited state calculations. *Computer Physics Communications*, 180(8):1392–1403, 08 2009.

[70] P. Hohenberg and W. Kohn. Inhomogeneous electron gas. *Phys. Rev.*, 136(3B):B864–B871, 11 1964.

[71] W. Kohn and L. J. Sham. Self-consistent equations including exchange and correlation effects. *Phys. Rev.*, 140(4A):A1133–A1138, 11 1965.

[72] Erich Runge and E. K. U. Gross. Density-functional theory for time-dependent systems. *Phys. Rev. Lett.*, 52(12):997–1000, 03 1984.

[73] Lars Hedin. New method for calculating the one-particle Green's function with application to the electron-gas problem. *Phys. Rev.*, 139(3A):A796–A823, 08 1965.

[74] E. E. Salpeter and H. A. Bethe. A relativistic equation for bound-state problems. *Phys. Rev.*, 84(6):1232–1242, 12 1951.

[75] Judith Harl. *The linear response function in density functional theory: Optical spectra and improved description of the electron correlation.* PhD thesis, University of Vienna, faculty of physics, 10 2008. [Chapter 1].

[76] Juan Carlos Cuevas. Introduction to density functional theory. [Presentation at Institut fur Theoretische Festkorperphysik, Universitat Karlsruhe (Germany)].

[77] John P. Perdew, Kieron Burke, and Matthias Ernzerhof. Generalized gradient approximation made simple. *Phys. Rev. Lett.*, 77(18):3865–3868, 10 1996.

[78] Judith Harl. *The linear response function in density functional theory: Optical spectra and improved description of the electron correlation.* PhD thesis, University of Vienna, faculty of physics, 10 2008. [Chapter 2].

[79] Luca Guido Molinari. A derivation of hedin's equations. 11 2017. Available at "https://www.researchgate.net/publication/268369049_A_DERIVATION_OF_HEDIN'S_EQUATIONS".

[80] D. Pines and P. Nozieres. *The Theory of Quantum Liquids*, volume 1 of *Advanced Books Classics*. Addison-Wesley, California, 1st edition, 1990.

[81] "second quantization" (the occupation-number representation). Available at "http://physics.gu.se/~tfkhj/OsloSecondQuant.pdf", 02 2013.

[82] Gerald D. Mahan. *Many Particle Physics*. Physics of Solids and Liquids. Springer US, 2000.

[83] Cristiane Morais Smith. The single particle Green's function. [Chapter 4].

[84] Cristiane Morais Smith. Perturbation theory at zero temperature. [Chapter 5].

[85] F Aryasetiawan and O Gunnarsson. The GW method. *Reports on Progress in Physics*, 61(3):237–312, 03 1998.

[86] Cristiane Morais Smith. Self energy, Dyson's equation, quasiparticle energy and life time (electron systems). [Chapter 7].

[87] Sergey V. Faleev, Mark van Schilfgaarde, and Takao Kotani. All-electron self-consistent GW approximation: Application to Si, MnO, and NiO. *Phys. Rev. Lett.*, 93(12):126406, 09 2004.

[88] M. van Schilfgaarde, Takao Kotani, and S. Faleev. Quasiparticle self-consistent GW theory. *Physical Review Letters*, 96(22):226402, 06 2006.

[89] Robert van Leeuwen. Introduction to many body theory. [Presentation at Department of Physics, Nanoscience Center, University of Jyväskylä, Finland], 2014.

[90] Francesco Sottile. *Response functions of semiconductors and insulators : from the Bethe-Salpeter equation to time-dependent density functional theory*. PhD thesis, Ecole Polytechnique, 09 2003. Available at "https://www.researchgate.net/publication/45378372_Response_functions_of_semiconductors_and_insulators_from_the_Bethe-Salpeter_equation_to_time-dependent_density_functional_theory".

[91] F. Bechstedt, K. Tenelsen, B. Adolph, and R. Del Sole. Compensation of dynamical quasiparticle and vertex corrections in optical spectra. *Phys. Rev. Lett.*, 78(8):1528–1531, 02 1997.

[92] L. V. Keldysh. Coulomb interaction in thin semiconductor and semimetal films. *Journal of Experimental and Theoretical Physics Letters*, 29(11):658, 06 1979.

[93] Thomas Olsen, Simone Latini, Filip Rasmussen, and Kristian S. Thygesen. Simple screened hydrogen model of excitons in two-dimensional mtaerials. *Phy. Rev. Lett.*, 116(5):056401, 02 2016.

[94] Alexey Chernikov, Timothy C. Berkelbach, Heather M. Hill, Albert Rigosi, Yilei Li, Ozgur Burak Aslan, David R. Reichman, Mark S. Hybertsen, and Tony F. Heinz. Exciton binding energy and nonhydrogenic Rydberg series in monolayer WS_2. *Phys. Rev. Lett.*, 113(7):076802, 08 2014.

[95] O. Pulci, M. Marsili, V. Garbuio, P. Gori, I. Kupchak, and F. Bechstedt. Excitons in two dimensional sheets with honeycomb symmetry. *Physica Status Solidi (b)*, 252(1):72–77, 06 2015. DOI: 10.1002/pssb.201350404.

[96] A. S. Rodin, A. Carvalho, and A. H. Castro Neto. Excitons in anisotropic two-dimensional semiconducting crystals. *Phys. Rev. B*, 90(7):075429, 08 2014. DOI: 10.1103/PhysRevB.90.075429.

[97] Pierluigi Cudazzo, Ilya V. Tokatly, and Angel Rubio. Dielectric screening in two dimensional insulators: Implications for excitonic and impurity states in graphane. *Phys. Rev. B*, 84(8):085406, 08 2011.

[98] John Singleton. *Band Theory and Electronic Properties of Solids*. Oxford Master Series in Condensed Matter Physics. Oxford University Press, New York, 2001. [Chapter 5].

[99] Alexandre Reily Rocha. Hydrogen atom in two dimensions. [Class notes], 10 2016.

[100] P. J. Salzman. The Numerov algorithm. Department of Physics, University of California, 06 2001. Available at "http://www.physics.muni.cz/~jancely/NM/Procedury/ProcG95/NM/ODE/numerov/numerov.pdf".

[101] N. Bouad, L. Chapon, R.-M. Marin-Ayral, F. Bouree-Vigneron, and J.-C. Tedenac. Neutron powder diffraction study of strain and crystallite size in mechanically alloyed PbTe. *Journal of Solid State Chemistry*, 173(0022-4596):189–195, 2003.

[102] C. Adenis, V. Langer, and O. Lindqvist. Reinvestigation of the structure of tellurium. *Acta Crystallographica Section C*, 45(6):941–942, 06 1989.

[103] Lede Xian, Alejandro Perez Paz, Elisabeth Bianco, Pulickel M Ajayan, and Angel Rubio. Square selenene and tellurene: novel group VI elemental 2d materials with nontrivial topological properties. *2D Materials*, 4(4):041003, 08 2017.

Appendix

APPENDIX A

2D polarizability average

The electric potential (eq. (3.13)) can be generalized for the case when α_{2D} is a tensor. In this particular case α_{2D} has 4 components. Those are α^{x}_{2D}, α^{y}_{2D} and $\alpha^{xy}_{2D} = \alpha^{yx}_{2D}$, where the mixed components α^{xy}_{2D} contributions are zero. So, we have an equation,

$$\phi_{2D}(\mathbf{q}) = \frac{2\pi e}{q + 2\pi\alpha^{x}_{2D} q_x^2 + 2\pi\alpha^{y}_{2D} q_y^2}, \tag{A.1}$$

where q represents the modulus $|\mathbf{q}|$ and q_x, q_y its components. In real space the equation looks like

$$\phi_{2D}(\rho) = \frac{e}{2\pi}\int_0^{\infty}\int_0^{2\pi} \frac{1}{q + 2\pi\alpha^{x}_{2D} q^2\cos^2(\psi) + 2\pi\alpha^{y}_{2D} q^2\sin^2(\psi)} e^{q\rho\cos(\theta-\psi)} q\,dq\,d\psi, \tag{A.2}$$

and, by using the following identities:

$$F(q,\psi) = \sum_{infty}^{+\infty} F_n(q) e^{in\psi}, \tag{A.3}$$

$$F_n(q) = \frac{1}{2\pi}\int_0^{2\pi} F(q,\psi) e^{-in\psi} d\psi, \tag{A.4}$$

$$e^{iq\rho\cos(\theta-\psi)} = \sum_{-\infty}^{+\infty} i^n J_n(\rho q) e^{in\theta} e^{-in\psi}, \tag{A.5}$$

$$e^{-iq\rho\cos(\theta-\psi)} = \sum_{-\infty}^{+\infty} i^{-n} J_n(\rho q) e^{-in\theta} e^{in\psi}. \tag{A.6}$$

We obtain,

$$\phi_{2D}(\rho) = \frac{e}{2\pi}\sum_{-\infty}^{+\infty} i^n e^{in\theta}\int_0^{\infty}\int_0^{2\pi} F_n(q) J_n(q\rho) q\,dq\,d\psi, \tag{A.7}$$

and, integrating by ψ:

$$\phi_{2D}(\rho) = e\sum_{-\infty}^{+\infty} i^n e^{in\theta}\int_0^{\infty}\int_0^{2\pi} F_n(q) J_n(q\rho) q\,dq\,d\psi, \tag{A.8}$$

where the term $F_n(q)$,

$$F_n(q) = \frac{1}{2\pi}\int_0^{2\pi} F(q,\psi) e^{-in\psi} d\psi,$$

$$F_n(q) = \frac{1}{2\pi}\int_0^{2\pi} \frac{1}{q + 2\pi\alpha^{x}_{2D} q^2\cos^2(\psi) + 2\pi\alpha^{y}_{2D} q^2\sin^2(\psi)} (\cos(n\psi) - i\sin(n\psi)) d\psi, \tag{A.9}$$

$$\tag{A.10}$$

has the contributions only arising from even n coupled with $\cos(n\psi)$, and odd n with $\sin(n\psi)$. However, the contributions from integrals with $\sin(n\psi)$ are almost zero. So, $F_n(q)$ is

$$F_n(q) = \frac{1}{2\pi}\int_0^{2\pi} \frac{\cos(n\psi)}{q + \bar{m} q^2\cos^2(\psi) + \bar{n} q^2\sin^2(\psi)} d\psi. \tag{A.11}$$

By replacing it on ϕ_{2D}, we have

$$\begin{aligned}
\phi_{2D} =& \frac{e}{2\pi}\Bigg[\sum_{n=-2}^{-\infty} i^n e^{in\theta}\int_0^{+\infty}\int_0^{2\pi}\frac{\cos(n\psi)}{q+\bar{m}q^2\cos^2(\psi)+\bar{n}q^2\sin^2(\psi)}J_n(q\rho)qdq \\
&+\int_0^{+\infty}\int_0^{2\pi}\frac{\cos(n\psi)}{q+\bar{m}q^2\cos^2(\psi)+\bar{n}q^2\sin^2(\psi)}J_0(q\rho)qdq \\
&+\sum_{n=2}^{+\infty} i^n e^{in\theta}\int_0^{+\infty}\int_0^{2\pi}\frac{\cos(n\psi)d\psi}{q+\bar{m}q^2\cos^2(\psi)+\bar{n}q^2\sin^2(\psi)}J_n(q\rho)qdq\Bigg], \\
\phi_{2D} =& \frac{e}{2\pi}\Bigg[\sum_{n=-2}^{-\infty} i^n(\cos(n\theta)+i\sin(n\theta))T_n(\rho)+T_0(\rho) \\
&+\sum_{n=2}^{+\infty} i^n(\cos(n\theta)+i\sin(n\theta))T_n(\rho)\Bigg],
\end{aligned} \tag{A.12}$$

where

$$T_n(\rho)=\int_0^{+\infty}\int_0^{2\pi}\frac{\cos(n\psi)}{q+\bar{m}q^2\cos^2(\psi)+\bar{n}q^2\sin^2(\psi)}J_n(q\rho)qdq. \tag{A.13}$$

We can reduce eq. (A.12) by using the identity

$$J_n(q\rho)=(-1)^n J_n(q\rho), \tag{A.14}$$

which coupled with a negative even n gives

$$T_n(\rho)=T_{-n}(\rho). \tag{A.15}$$

Consequently, the 2D electric potential becomes

$$\phi_{2D}=\frac{e}{2\pi}\left[T_0(\rho)+2\sum_{n=2}^{+\infty} i^n cos(n\theta)T_n(\rho)\right], \tag{A.16}$$

for the anisotropic polarization case.

Firstly, We approximate the summation to just the two first terms (*i.e.* T_0 and T_2) due to the fact that the Bessel function contribution becomes small for large values of n. Secondly, we notice that equation (A.16) depends on the angle θ, which is a disadvantage when try to solve this analytically. However, this problem is overcome by approximating all solutions from every angle to the case where $\theta=0$. This is shown in picture A.1-b, where we appreciate that contributions on angles $\theta=\pi/4,\pi/2$ are almost identical to the case where $\theta=0$. Lastly, we compare the solutions of the full anisotropic case (eq. (A.16)) with Keldysh isotropic solution (eq. (3.24) with an average value for $\alpha_{2D}=(\alpha_{2D}^x+\alpha_{2D}^y)/2$) as we see from figure A.1-a. Since both plots are identical, we can use the Keldysh solution with an average α_{2D} for our anisotropic hydrogen effective model

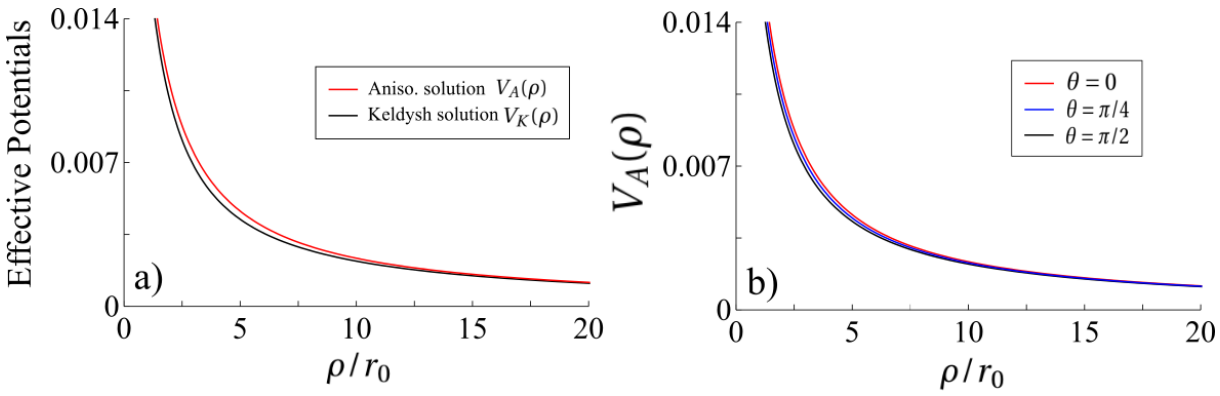

Figure A.1: a) Comparison between the anisotropic solution $V_A(\rho)$ (eq. (A.16)) and the Keldysh solution $V_K(\rho)$ with the average α_{2D} (eq. (3.24)). b) Anisotropic potential for different angles $\theta = 0$, $\theta = \pi/4$ and $\theta = \pi/2$

APPENDIX B

Thickness Dependent Structural Phase Transition

The formation of αTe is novel in the history of 2D materials. From what is known, 2D materials can be formed in two ways, those that can be mechanical exfoliated from their layered bulk such as graphene and MoS_2; and those, lacking a layered bulk counterpart, that have to be grown epitaxially on proper substrates such as silicene and statene [53]. However, tellurene can be formed from a new type of formation mechanism characterized by thickness-dependent structural phase transition. According to the results showed in [53], there are phase transitions when a few layer slab of Tellurium is relaxed, the α phase emerge after the relaxation of an slab with number of layers equals to $N = 3,6,9,12,15$ (they are the lowest energy points as is pictured in the figure B.1). Picture B.1 shows an example of this transition when $N = 8$ and $N = 9$[53]. After the formation of multilayered structures of α phase for the preferred thicknesses in a Te slab, the monolayers can be extracted by simple exfoliation.

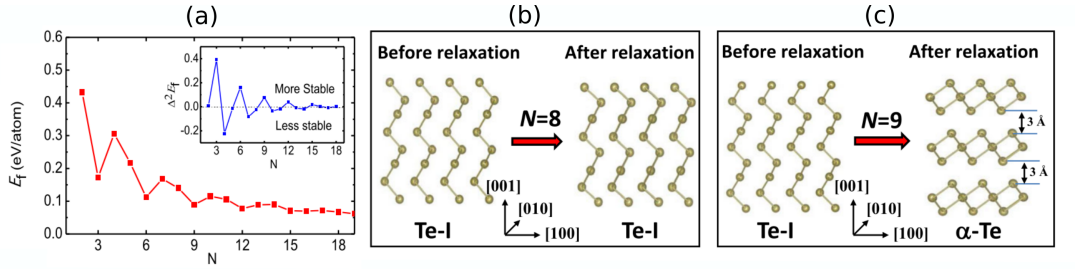

Figure B.1: (a) αTe formation energies E_f (minimal points) of the fully relaxed Te slabs as a function of the thickness. (b) and (c) The relaxation picture of the Te at N=8 and N=9, αTe emerges for N=9 extracted from [53].